Pulsed Laser Deposition and Characterization of Diamond-like Carbon and Graphitic Thin Films and Graphene

A Thesis submitted in partial fulfillment of the requirements for the award of the degree
of

DOCTOR OF PHILOSOPHY

by

INDRAJEET KUMAR

Department of Physics
Indian Institute of Technology Guwahati
Guwahati-781039, India
September, 2016

Dedicated to my Parents

Indrajeet Kumar
Registration No. 09612124
Department of Physics
Indian Institute of Technology Guwahati
Guwahati-781039, Assam, India

Statement

I hereby declare that the matter embodied in this thesis is the result of investigations carried out by me at the Department of Physics, Indian Institute of Technology Guwahati, Guwahati, India, under the supervision of ***Prof. Alika Khare***. This thesis has not been submitted to any university/institute or elsewhere for the award of any degree, diploma or associateship.

Date: Sept , 2016 **Indrajeet Kumar**

भारतीय प्रौद्योगिकी संस्थान गुवाहाटी
Indian Institute of Technology Guwahati
Department of Physics
Guwahati-781039, Assam State, INDIA
Phone: +91 361 2582705, 2582701, 2690321 to 328 (extn. 2705),
Fax: +91 361 2582749
Dr. Alika Khare
Professor
E-mail: alika@iitg.ernet.in, k_alika@yahoo.com

Date: Sept , 2016

Certificate

This is to certify that work contained in the thesis entitled '**Pulsed Laser Deposition and Characterization of Diamond-like Carbon and Graphitic Thin Films and Graphene**' by **Indrajeet Kumar** (Roll no: 09612124), a student of Department of Physics, Indian Institute of Technology Guwahati, for the award of degree of Doctor of Philosophy, has been carried out under my supervision and that the same has not been submitted elsewhere for any other degree.

(Alika Khare)

Acknowledgement

First and foremost I would like to express my sincere thanks towards my thesis supervisor, Prof. Alika Khare for her constant inspiration and precious advice throughout my research. Her fundamental scientific approach and forward thinking provided me a great base to conduct the research work. Without her guidance, intuition, patience and endless hours of discussion, this thesis would not exist. I consider it a great privilege that I had the opportunity to work as a student under her supervision. Apart from professional suggestions she gave me moral support and strengthened my skills in various ways.

I am also grateful to my doctoral committee members, Dr. Girish Sampath Setlur, Dr. Ashwini Kumar Sharma and Dr. G. Krishnamoorthy for their careful and well thought out critique of progress of my thesis and providing valuable suggestions which steered the thesis in right direction. I owe my thanks to present and former Head of Department of Physics, IIT Guwahati for providing me the necessary facilities to fulfil my PhD thesis objectives. Thanks to the entire faculty, staff and students who make this place a great environment to work in.

I am also thankful to Central Instruments Facility, IIT Guwahati for instrumentation facilities. In particular, I would like to extend my sincere thanks to Mr. Chandan Borgohain, Mr. Kula Kamal Senapati and Mr. Madhurjya Borah for their kind help with various instruments.

It has been pleasure to work with my research lab members Dr. Gaurav, Dr. Arpita, Dr. Archana, Dr. Abu, Dr. Satchi, Dr. Poulami, Partha, Gyan, Shantakumar, Rahul, Prahlad, Eshita, Gobinda and Sasmita. Thanks to them for assistance in experiments and providing enjoyable work environment in the lab and in particular I would like to thank Rahul for helping me to analyse the ellipsometric data.

I am deeply indebted to all my friends Dilip, Himanshu, Mukesh, Satendra, Onkar, Asha and Nisha at IIT Guwahati for making me feel like at home during all these years and successful completion of this thesis. I must acknowledge all my batchmates for their love, encouragement and support.

Last but not least, I would like to express my deepest appreciation to my family members for providing me support and encouragement throughout my academic studies even when distance kept us apart.

Abstract

The present work aims towards the fabrication and characterization of diamond-like carbon (DLC) and graphitic thin films and few-/multi-layer graphene via pulsed laser deposition (PLD) technique. DLC thin films deposited via PLD were found to be hydrogen-free and can be used for high temperature applications.

The structural characterization of all the films fabricated via PLD was performed by Raman spectrometer. The intensity of the excitation laser source while recording the Raman spectrum of DLC films plays a crucial role in the correct measurement of film quality. Thus, in order to assess the appropriate laser intensity, the Raman spectrum of a particular pulsed laser deposited DLC film was recorded as a function of excitation laser intensity in the range of 11-382 kW/cm^2. It was observed that upto the laser intensity of 114 kW/cm^2, there was not much significant changes in the Raman spectra while above this, the spectra was drastically modified indicating the effect of focal heating and these changes in the film are of permanent nature. Thus, the Raman spectra reported in the entire thesis were recorded at a laser intensity of 114 kW/cm^2.

The effect of deposition parameters; substrate temperature, laser fluence and the background helium gas pressure on the DLC film was undertaken in detail. It was observed that the low substrate temperature favoured the formation of carbon film dominated by sp^3 bonding while the film deposited at higher temperature, 700 °C and above, exhibited the graphitic nature. The variation in sp^3 fraction of the DLC thin film was more pronounced in case of helium pressure as compared to that of laser fluence. The sp^3 fraction of DLC thin films fabricated at RT was observed to be increasing with the increase in helium pressure from 0.05 mbar to 1 mbar. The higher pressure of helium gas was observed to favour the structural ordering of graphitic thin films deposited at 750 °C. Highly ordered graphitic thin film was observed at helium pressure of 10 mbar. The linear optical properties of DLC and graphitic thin films were studied by spectroscopic ellipsometer and results were found to be in agreement with that of Raman studies. Graphene layers were also fabricated in oxygen ambient of 0.1 mbar and at laser fluence of 5.0 J/cm^2. The line shape of 2D band of Raman spectra showed the signature

of multilayer graphene at RT and few-layer graphene at the substrate temperature of 700 °C. Thus, the desired quality of the carbon based thin films devoid of hydrogen can be easily fabricated simply by selecting the appropriate deposition parameters.

The π bonds associated to sp^2 bonding in DLC and graphitic thin films provide the nonlinear optical behaviour. To study the optical nonlinearity in DLC and graphitic thin films, conventional *Z*-scan setup was modified by replacing the photodiode detector with the charge-coupled device camera. The modified setup facilitates the advantage of obtaining the open aperture and closed aperture *Z*-scan data in a single scan. Another advantage of this setup is in optimization of the aperture size for closed aperture *Z*-scan measurement without repeating the experiment so as to obtain the nonlinear refractive index coefficient with minimal contribution of nonlinear absorption. DLC and graphitic thin films showed the positive nonlinearity. The NLR coefficient of carbon thin films was found to be increased with the sp^2 content.

Contents

Abstract *i*

List of Figures *vii*

List of Tables *xiii*

List of Abbreviations *xv*

List of Symbols *xvii*

1. Introduction **1**

1.1 Pulsed laser deposition technique 5

1.2 Characterization of carbon thin films 8

1.2.1 Raman spectroscopy 8

1.2.2 Ultraviolet-visible (UV-Vis) spectroscopy 12

1.2.3 Spectroscopic ellipsometry 12

1.2.4 Fourier transform infrared spectroscopy 15

1.2.5 X-ray diffraction 16

1.3 Optical nonlinearity in carbon based thin films 16

1.4 Organization of present thesis 18

Bibliography 21

2. Experimental details **37**

2.1 Pulsed laser deposition (PLD) setup 37

2.2 Characterization of PLD thin films 40

2.2.1 Atomic force microscopy (AFM) 40

2.2.2 Field emission scanning electron microscopy (FESEM) 40

2.2.3 Transmission electron microscopy (TEM) 40

2.2.4 Raman spectroscopy 41

2.2.5 Fourier transform infrared spectroscopy (FTIR) 41

2.2.6 Spectroscopic ellipsometry 41

2.2.7 Stylus profilometer 42

2.3 Modified *Z*-scan setup 42
Conclusion 44
Bibliography 45

3. Effect of cw laser irradiation on DLC films 47
3.1 Experimental details 48
3.2 Effect of laser intensity while recording the Raman spectra of PLD-DLC thin film 49
3.3 Effect of laser annealing on structural changes in PLD-DLC thin film 57
3.4 Effect of substrate on structural modification of DLC film at high laser intensity 60
Conclusion 62
Bibliography 63

4. Characterization of pulsed laser deposited DLC and graphitic thin films 65
4.1 Experimental details 66
4.2 Effect of deposition parameters on DLC thin films 67
4.2.1 Effect of substrate temperature on PLD-DLC thin films 69
4.2.1.1 Raman spectra of DLC thin films deposited at various substrate temperature 69
4.2.1.2 Spectroscopic ellipsometric study for linear optical properties of DLC thin films as a function of deposition temperature 74
4.2.2 Effect of laser fluence on PLD-DLC thin films 77
4.2.2.1 Raman spectra of DLC thin films as a function of laser fluence 77
4.2.2.2 FTIR spectra of DLC thin films as a function of laser fluence 79
4.2.2.3 Optical constants of DLC thin films as a function of laser fluence via spectroscopic ellipsometry 80
4.2.2.4 Optical band gap using UV-Visible-NIR transmission spectra 81
4.2.3 Effect of helium gas pressure on PLD-DLC thin films 84
4.2.3.1 Structural characterization using Raman spectroscopy of DLC thin films as a function of helium pressure 84

4.2.3.2 Linear optical parameters using spectroscopic ellipsometry for PLD-DLC thin films as a function of helium pressure 87
4.2.3.3 Transmission spectroscopy for optical band gap 91
4.2.3.4 Effect of laser fluence and helium pressure on the particle size distribution of PLD-DLC thin films 93
4.3 Fabrication of graphitic thin films 96
4.3.1 Raman spectra of graphitic thin films as a function of helium pressure 97
4.3.2 Measurement of linear optical constants of graphitic thin films using spectroscopic ellipsometer 101
4.3.3 UV-Visible-NIR transmission spectra of graphitic thin films 102
4.3.4 Surface morphology of graphitic thin films as a function of helium pressure 103
Conclusion 105
Bibliography 107

5. Fabrication and characterization of few- and multi-layer graphene via PLD technique 111
5.1 Experimental details 112
5.2 Raman spectra of few- and multi-layer graphene 112
5.3 Transmission electron microscope images of few- and multi-layer graphene 118
5.4 Field emission electron microscopy of few- and multi-layer graphene 120
Conclusion 120
Bibliography 121

6. Modified *Z*-scan setup using CCD camera 123
6.1 Experimental details 125
6.2 Analysis of CCD images for extracting NLA and NLR coefficients 126
6.2.1 Estimation of NLA coefficient 129
6.2.2 Optimization of aperture size for CA *Z*-scan 130
6.2.3 Estimation of NLR coefficient 131
Conclusion 133
Bibliography 135

7. Optical nonlinearity in pulsed laser deposited DLC and graphitic thin films **137**

7.1 Experimental details 139

7.2 NLR coefficient of DLC thin films deposited as a function of substrate temperature 139

7.3 NLR coefficient of DLC thin films deposited as a function of laser fluence 143

7.3.1 NLR coefficient of DLC thin films deposited in vacuum 143

7.3.2 NLR coefficient of DLC thin films deposited at helium pressure of 0.05 mbar 144

7.4 NLR coefficient of DLC thin films deposited as a function of helium pressure 146

7.5 NLR coefficient of graphitic thin films deposited as a function of helium pressure 147

Conclusion 149

Bibliography 151

8. Conclusion **153**

List of Publications **159**

List of Figures

1.1	Ternary diagram for amorphous carbon-hydrogen alloys	2
1.2	Schematic of pulsed laser ablation chamber	6
1.3	Illustration of vibration mode of **(a)** G band and **(b)** D band	8
1.4	Raman spectrum of graphite	9
1.5	Raman spectrum of few-layer graphene	10
1.6	Raman spectrum of natural diamond	10
1.7	Raman spectrum of DLC thin film	11
1.8	Raman spectrum of glassy carbon thin film	11
1.9	Reflection of polarized light on film-substrate surface and geometrical interpretation of ellipsometer parameters (ψ, Δ)	13
1.10	Geometrical interpretation of parameters r_p and r_s	14
1.11	FTIR spectrum of hydrogen-free DLC thin film	15
2.1	Schematic of PLD setup	38
2.2	Photograph of **(a)** PLD setup and **(b)** target-substrate configuration	39
2.3	Schematic of structure adopted for dispersion model	42
2.4	Schematic of modified *Z*-scan setup	43
2.4	Photograph of modified *Z*-scan setup	43
3.1	Raman spectra of DLC thin film as a function of laser intensity	49
3.2	Deconvoluted Raman spectra of DLC thin film as a function of laser intensity **(a)** 11 kW/cm^2, **(b)** 114 kW/cm^2, **(c)** 254 kW/cm^2 and **(d)** 382 kW/cm^2	50
3.3	**(a)** Dispersion of G band and **(b)** Dispersion rate of G band	52

3.4	**(a)** G band, **(b)** D band and **(c)** Band-3 (~1200 cm^{-1}) as a function of laser intensity	53
3.5	Integrated intensity of Raman bands as a function of laser intensity	53
3.6	Raman spectra of DLC thin film recorded at 114 kW/cm^2 after laser annealing for 5 min in the intensity range 127-382 kW/cm^2	57
3.7	**(a)** Comparison of Raman spectra of as-deposited thin film and that of after laser annealing at intensity of 382 kW/cm^2 and **(b)** corresponding deconvoluted Raman spectrum of laser annealed DLC thin film	58
3.8	Comparison of band parameters of G and D bands at high laser intensity and after laser annealing	59
3.9	Integrated intensity ratio, I_D/I_G, of as-deposited film and after laser annealing	60
3.10	Raman spectra of DLC thin film on silicon substrate at various laser intensities	61
4.1	Raman spectra of DLC thin films deposited on fused silica substrate as a function of substrate temperature	69
4.2	Deconvoluted Raman spectra of carbon thin films deposited at **(a)** RT, **(b)** 300 °C, **(c)** 500 °C and **(d)** 750 °C	70
4.3	**(a)** Peak position of G band and I_D/I_G ratio as a function of substrate temperature and **(b)** Variation of FWHM of G band with substrate temperature	71
4.4	**(a)** I_D/I_G ratio as a function of FWHM of G band and **(b)** sp^2 cluster size as a function of substrate temperature	72
4.5	**(a)** Dispersion of G band for film deposited at RT and **(b)** Dispersion rate of G band for films deposited at RT, 300 °C, 500 °C and 750 °C	73
4.6	mFB fit for **(a)** pseudo refractive index and **(b)** pseudo extinction coefficient for films deposited at RT, 300 °C, 500 °C and 750 °C	75
4.7	Raman spectra of DLC thin films deposited at RT as a function of laser fluence	77
4.8	Deconvoluted Raman spectra of DLC thin film deposited at a laser fluence of 5.0 J/cm^2	78
4.9	Dispersion rate of G band for DLC thin films deposited at RT and laser fluence of 5.0 J/cm^2, 6.7 J/cm^2, 8.3 J/cm^2, 10.0 J/cm^2 and 11.7 J/cm^2	79

4.10 FTIR transmission spectra for DLC thin films deposited at RT and laser fluence of 5.0 J/cm^2, 6.7 J/cm^2, 8.3 J/cm^2, 10.0 J/cm^2 and 11.7 J/cm^2 80

4.11 mFB fit for **(a)** pseudo refractive index and **(b)** pseudo extinction coefficient for DLC thin films deposited at RT as a function of laser fluence 80

4.12 Transmission spectra of DLC thin films deposited at RT as a function of laser fluence of 5.0 J/cm^2, 6.7 J/cm^2, 8.3 J/cm^2, 10.0 J/cm^2 and 11.7 J/cm^2 82

4.13 Tauc plot for DLC thin films deposited at RT and laser fluence of 5.0 J/cm^2, 6.7 J/cm^2, 8.3 J/cm^2, 10.0 J/cm^2 and 11.7 J/cm^2 83

4.14 Comparison of Tauc energy gap and mFB energy gap for DLC thin films as a function of laser fluence 83

4.15 Raman spectra of DLC thin films deposited at laser fluence of 10.0 J/cm^2, 11.7 J/cm^2, 13.3 J/cm^2 and 15.0 J/cm^2 and helium pressure of **(a)** 0.05 mbar, **(b)** 0.1 mbar, **(c)** 0.5 mbar and **(d)** 1 mbar 85

4.16 Deconvoluted Raman spectra of DLC thin films deposited at laser fluence of 15.0 J/cm^2 as a function of helium pressure **(a)** 0.05 mbar, **(b)** 0.1 mbar and **(c)** 0.5 mbar 86

4.17 Dispersion rate of G band for DLC thin films deposited at a laser fluence of 15.0 J/cm^2 and helium pressure of 0.05mbar, 0.1 mbar and 0.5 mbar 86

4.18 mFB fit for **(a)** pseudo refractive index and **(b)** pseudo extinction coefficient for DLC thin films deposited at a laser fluence of 15.0 J/cm^2 and helium pressure of 0.05 mbar, 0.1 mbar, 0.5 mbar and 1 mbar 87

4.19 Transmission spectra of DLC thin films deposited at a laser fluence of 15.0 J/cm^2 and helium pressure of 0.05 mbar, 0.1 mbar, 0.5 mbar and 1 mbar 91

4.20 Tauc plot for DLC thin films deposited at a laser fluence of 15.0 J/cm^2 and helium pressure of 0.05 mbar, 0.1 mbar, 0.5 mbar and 1 mbar 92

4.21 Comparison of Tauc energy gap and mFB energy gap for DLC thin films deposited in helium ambient 93

4.22 Surface morphology of DLC thin films deposited at helium pressure of 1 mbar and laser fluence of **(a)** 10.0 J/cm^2, **(b)** 11.7 J/cm^2, **(c)** 13.3 J/cm^2 and **(d)** 15.0 J/cm^2 94

4.23 Particle size distribution of DLC thin films deposited at helium pressure of 1 mbar and laser fluence of **(a)** 10.0 J/cm^2, **(b)** 11.7 J/cm^2, **(c)** 13.3 J/cm^{2}and **(d)** 15.0 J/cm^2 94

4.24	Surface morphology of DLC thin films deposited at a laser fluence of 15.0 J/cm^2 and helium pressure of **(a)** 0.05 mbar, **(b)** 0.1 mbar, **(c)** 0.5 mbar and **(d)** 1 mbar	95
4.25	Particle size distribution of DLC thin films deposited at a laser fluence of 15.0 J/cm^2 and helium pressure of **(a)** 0.1 mbar, **(b)** 0.5 mbar and **(c)** 1 mbar	96
4.26	Raman spectra of graphitic thin films as a function of helium pressure	98
4.27	Deconvoluted Raman spectra of graphitic thin films deposited at **(a)** 10^{-5} mbar and **(b)** helium pressure of 10 mbar	98
4.28	mFB fit for **(a)** pseudo refractive index and **(b)** pseudo extinction coefficient for graphitic thin films deposited at background pressure of ~10^{-5} mbar and helium pressure of 0.1 mbar, 1 mbar, 5 mbar and 10 mbar	101
4.29	Transmission spectra of graphitic thin films as a function of deposition pressure	102
4.30	Surface morphology of graphitic thin films as a function of deposition pressure **(a)** 10^{-5} mbar, **(b)** 0.1 mbar helium, **(c)** 1 mbar helium, **(d)** 5 mbar helium and **(e)** 10 mbar helium	103
4.31	Particle size distribution for the graphitic thin films deposited at helium pressure of **(a)** 0.1 mbar, **(b)** 1 mbar and **(b)** 5 mbar	104
5.1	Raman spectra of graphene layers deposited at **(a)** RT, **(b)** 300 °C, **(c)** 500 °C and **(d)** 700 °C	113
5.2	2D band splitting of graphene layers deposited at **(a)** RT, **(b)** 300 °C, **(c)** 500 °C and **(d)** 700 °C	115
5.3	Variation in Raman spectrum of graphene sample prepared at 700 °C with excitation laser wavelength	117
5.4	Dispersion of D and 2D peak position of few-layer graphene	118
5.5	**(a)**, **(b)** TEM images and **(c)** SAED pattern of graphene sample prepared at RT	119
5.6	**(a)** TEM images, **(b)** HRTEM and **(c)** SAED pattern of graphene sample prepared at 700 °C	119
5.7	FESEM images of graphene layers deposited at **(a)** RT and **(b)** 700 °C	120
6.1	Schematic of **(a)** conventional *Z*-scan setup in open aperture configuration **(b)** conventional Z-scan setup in closed aperture configuration and **(c)** modified Z-scan setup	123

6.2	CCD image of transmitted beam through film positioned at 20 mm from focal point: **(a)** open aperture and **(b)** closed aperture *Z*-scan for S~0.40	126
6.3	Flow chart for obtaining OA and CA *Z*-scan transmission curve	127
6.4	Flow chart for function: Circular aperture (R)	128
6.5	Normalized transmittance curve for carbon thin film for open aperture *Z*-scan	129
6.6	**(a)** Marking of apertures on CCD image for various values of '*S*' and **(b)** CA *Z*-scan curve for various aperture sizes; S~0.20, 0.25, 0.30, 0.35, 0.40, 0.45, 0.50, 0.55 and 0.60	130
6.7	ΔI_{pv} for CA transmission curve as a function of aperture size '*S*'	131
6.8	Normalized transmittance curve for carbon film for closed aperture *Z*-scan, *S*~0.40	132
7.1	Linear absorption coefficient of DLC thin films at 632.8 nm as a function of substrate temperature	140
7.2	Normalized open aperture and closed aperture *Z*-scan transmittance curve for fused silica substrate	140
7.3	Normalized closed aperture *Z*-scan transmittance curve for DLC thin films deposited at **(a)** RT, **(b)** 300 °C, **(c)** 500 °C and **(d)** 750 °C	141
7.4	NLR coefficient of DLC thin films as a function of substrate temperature	142
7.5	Normalized closed aperture *Z*-scan transmittance curve for DLC thin films deposited at a base pressure of ~10^{-5} mbar and laser fluence of **(a)** 5.0 J/cm^2, **(b)** 6.7 J/cm^2, **(c)** 8.3 J/cm^2, **(d)** 10.0 J/cm^2 and **(e)** 11.7 J/cm^2	143
7.6	NLR coefficient of DLC thin films as a function of laser fluence	144
7.7	Normalized closed aperture *Z*-scan transmittance curve for DLC thin films deposited at 0.05 mbar of helium pressure and laser fluence of **(a)** 10.0 J/cm^2, **(b)** 11.7 J/cm^2, **(c)** 13.3 J/cm^2 and **(d)** 15.0 J/cm^2	145
7.8	Normalized closed aperture *Z*-scan transmittance curve for DLC thin films deposited at a laser fluence of 15.0 J/cm^2 and helium pressure of **(a)** 0.05 mbar, **(b)** 0.1 mbar, **(c)** 0.5 mbar and **(d)** 1 mbar	146
7.9	Normalized closed aperture *Z*-scan transmittance curve for graphitic thin films deposited at a laser fluence of 5.0 J/cm^2 and pressure of **(a)** 10^{-5} mbar, **(b)** 0.1 mbar helium, **(c)** 1 mbar helium, **(d)** 5 mbar helium and **(e)** 10 mbar helium	148

भारतीय प्रौद्योगिकी संस्थान गुवाहाटी
Indian Institute of Technology Guwahati

List of Tables

1.1	Properties of various form of carbon	2
3.1	Raman band position, FWHM of G and D bands and I_D/I_G ratio of DLC film as a function of laser intensity	51
3.2	Percentage Change in integrated intensity of Raman spectra of PLD-DLC film and their deconvoluted bands as a function of laser intensity w.r.t. laser intensity of 11 kW/cm^2.	54
3.3	Raman band position, FWHM of G and D band and I_D/I_G ratio of laser annealed DLC film	58
4.1	Deposition parameters for the fabrication of DLC thin films	68
4.2	Refractive index, extinction coefficient and optical band gap of carbon thin films as a function of substrate temperature	75
4.3	Raman band parameters of DLC thin films as a function of laser fluence	78
4.4	Thickness, band gap, refractive index and extinction coefficient of DLC thin films as a function of laser fluence	81
4.5	Tauc gap of DLC thin films as a function of laser fluence	83
4.6	Thickness of DLC thin films as a function of deposition condition	88
4.7	Band gap of DLC thin films as a function of deposition condition	89
4.8	Refractive index of DLC thin films at λ=633 nm as a function deposition condition	90
4.9	Extinction coefficient of DLC thin films at λ=633 nm as a function of deposition condition	91
4.10	Tauc band gap of DLC thin films as a function of laser fluence and helium gas pressure	92
4.11	Deposition parameters for graphitic thin film fabrication	97
4.12	Nature of deconvoluted Raman bands of graphitic thin films	99

4.13	Deconvoluted Raman band parameters of graphitic thin films as a function of ambient pressure	100
4.14	Band gap, refractive index and extinction coefficient of graphitic thin films as function of deposition pressure	102
5.1	Raman intensity ratio, I_D/I_G and I_{2D}/I_G of graphene layers as a function of substrate temperature	114
5.2	Dispersion of D and 2D band with the excitation laser wavelength in Raman spectra of FLG	117
7.1	NLR coefficient of DLC thin films deposited at 0.05 mbar of helium pressure as a function of laser fluence	145
7.2	NLR coefficient of DLC thin films deposited at laser fluence of 15.0 J/cm^2 as a function of helium pressure	147
7.3	NLR coefficient of graphitic thin films as a function of deposition pressure	148

List of Abbreviations

a-C	Amorphous carbon
AFM	Atomic force microscope
ATCC	Automated target carrousel controller
CA	Closed aperture
CCD	Charge-coupled device
CVD	Chemical vapor deposition
DC	Direct current
DLC	Diamond-like carbon
e.g.	for example
FESEM	Field emission scanning electron microscope
FLG	Few-layer graphene
FTIR	Fourier transform infrared
FWHM	Full width at half maxima
HC	Hydrocarbon
He:Ne	Helium Neon
HRTEM	High resolution transmission electron microscope
iLA	in-plane longitudinal acoustic
iTO	in-plane transverse optical
IR	Infrared
LIP	Laser induced plasma
LO	Longitudinal optical
LPP	Laser produced plasma
mFB	modified Forouhi-Bloomer
MLG	Multilayer graphene
NIR	Near infrared
ND	Neutral density
Nd:YAG	Neodymium-doped Yttrium Aluminium Garnet
NLA	Nonlinear absorption
NLO	Nonlinear optics
NLR	Nonlinear refractive index
OA	Open aperture

PLD	Pulsed laser deposition
PECVD	Plasma enhanced chemical vapor deposition
RF	Radio frequency
RMS	Root mean square
RT	Room temperature
SAED	Selected area diffraction pattern
sccm	standard cubic centimetres per minute
ta-C	Tetrahedral amorphous carbon
ta-C:H	Hydrogenated tetrahedral amorphous carbon
TS	Translation stage
UV	Ultra-violet
w.r.t.	with respect to
XRD	X-ray diffraction
TO	Transverse optical

List of Symbols

~	approximately
α	linear absorption coefficient
β	nonlinear absorption coefficient
ε_1	real part of dielectric constant
ε_2	imaginary part of dielectric constant
λ	wavelength of light
ν	frequency of light
ρ	Fresnel reflection coefficient
ϕ	incident angle of plane polarized light
Δ	phase difference between *p*- and *s*- polarization
$\Delta\phi_o$	phase distortion
Δm	plasma flux supersaturation
ΔI_{pv}	difference between height of peak and depth of valley
$\Delta T_{p\text{-}v}$	difference in the normalized transmission of peak and valley
$\Delta z_{p\text{-}v}$	separation between peak and valley position
°C	degree Celsius
μm	micrometre
cm	centimetre
eV	electron volt
E_i	incident electric field
E_{ip}	incident electric field for *p*-polarization
E_{is}	incident electric field for *s*-polarization
E_g	optical band gap
E_p	energy corresponding to plasma frequency
E_r	reflected electric field
E_{rp}	reflected electric field for *p*-polarization
E_{rs}	reflected electric field for *s*-polarization
f	focal length
h	Plank's constant
He	helium

Hz	hertz
I_o	peak intensity at focus
J	joule
k	extinction coefficient
k_B	Boltzmann constant
K	Kelvin
keV	kilo electron volt
L_{eff}	effective length
mbar	millibar
min	minutes
n	refractive index
n_2	nonlinear refractive index coefficient
nm	nanometre
ns	nanosecond
Ni	nickel
O_2	oxygen
S	aperture size
Si	silicon
T_{cl}	closed aperture transmittance
T_{op}	open aperture transmittance
W	watt
z	sample position w.r.t. focus
z_o	Rayleigh length

Chapter 1

Introduction

Diamond-like carbon (DLC) thin films have great importance in the field of research and industry due to the relatively low cost of production and properties similar to that of diamond. It exhibits a unique combination of properties; extremely high hardness, low friction coefficient, high wear-resistance, excellent chemical and electrochemical stability, good thermal conductivity, high transmission in the infra-red region, etc. [**1-6**]. As a protective coating, DLC films are applied on cutting tools, magnetic storage disks, biomedical coating, optical windows, moving components of a machine, etc. [**7-10**]. DLC films are also appearing as a promising candidate for anti-reflection coating on solar cells [**11**]. The high thermal conductivity makes it a suitable coating material as a heat sink for semiconductor devices [**12**]. DLC film is a mixed structure of sp^3, sp^2 and *sp* bonding of carbon atoms [**2**]. The sp^3 bonding confers the properties of diamond whereas sp^2 fraction extends the graphite-like properties. The content of *sp* hybridized carbon bonds is very low and has hardly any effect on the properties of DLC films. Due to the mixed structure, it is amorphous in nature. The various structures of amorphous carbon can be visualized through a ternary phase diagram of carbon as a function of sp^2, sp^3 and hydrogen contents, shown in *Figure 1.1*, proposed by Jacob and Moller in 1993 [**2, 13**]. In this diagram, sp^3, sp^2 and H content are represented by the top, left and right vertices of the triangle, respectively. Amorphous carbon with disordered graphitic materials; rich in sp^2 bonds such as carbon soot, chars,

glassy carbon and evaporated amorphous carbon (*a-C)* lie towards lower left corner. The lower right corner of the ternary diagram represents the hydrogen abundant region. Hydrocarbon polymers are located next to the hydrogen abundant region. The locations of other amorphous carbon are also shown in ternary diagram, *Figure 1.1*.

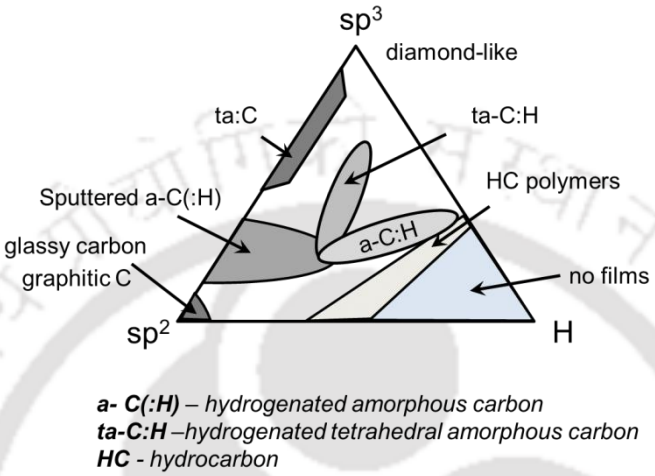

Figure 1.1: *Ternary diagram for amorphous carbon-hydrogen alloy.*

The properties of various forms of carbon are listed in *Table 1.1* [**2, 14-23**].

Table 1.1: *Properties of various form of carbon*

Materials		**sp^3 (%)**	**sp^2 (%)**	**H%**	**Density (g/cm^3)**	**Band gap (eV)**	**Hardness (GPa)**
diamond		100	0	0	3.515	5.5	100
graphite		0	100	0	2.267	0	
C_{60}		0	100	0		1.6	
graphene		0	100	0	1.8	0	
Graphite-like	glassy carbon	0	90-100	0	1.3-1.55	0.01	3
	evaporated carbon	0	90-100	0	1.9	0.4-0.7	3
	sputtered carbon	5	90-100	0	2.2	0.5	
Diamond-like	ta-C	80-88	10-20	0	3.1	2.5	80
	hard a-C:H	40		30-40	1.6-2.2	1.1-1.7	10-20
	soft a-C:H	60		40-50	1.2-1.6	1.7-4	<10
	ta-C:H	70		30	2.4	2.0-2.5	50

The properties of film containing high sp^3/sp^2 ratio resemble more of diamond and thus the film is referred as 'DLC' thin film. In 1970, Aisenberg and Chabot reported

the fabrication of DLC film using Ion Beam Deposition technique, possessing properties similar to that of diamond having refractive index greater than 2.0 [**24**]. Later in 1973, the same group demonstrated the industrial applications of DLC coating on stainless steel and plastic eyeglass lens [**25**]. The DLC coated steel blades for paper slitting operation were found to be 100 times longer than that of uncoated one [**25**]. The plastic eyeglass lens coated with DLC films was observed to be 3-6 times more scratch resistant than that of the uncoated one [**25**]. In 1976, Whitmell and Williamson reported hard insulating films of DLC having Vickers hardness of more than 2000 and thickness of the order of μm on variety of metallic substrates using direct current (DC) based glow discharge [**26**]. Holland and Ojha prepared hard insulating carbon films on dielectric substrates using radio frequency (RF) glow discharge method [**27, 28**]. Enke et al. reported the fabrication of DLC films having low friction coefficients ranging from 0.01 to 0.19 using RF plasma deposition method [**29, 30**]. In 1980s, Bubenzer et al. demonstrated the application of a-C:H films as an anti-reflection coating on IR optical components at a wavelength of 10.6 μm [**31, 32**]. The deposition of smooth, hard and dense carbon films having thickness around 200 nm have been reported using laser-arc technique [**33, 34**]. The refractive index of these films was ranging from 2.05 to 2.50 [**34**]. The fabrication of carbon films rich in sp^3 content have also been reported via mass selected ion beam, sputtering, cathodic arc, pulsed laser deposition (PLD), chemical vapor deposition (CVD) and plasma enhanced chemical vapour deposition (PECVD) techniques [**2, 35-46**]. The optical band gap of DLC films prepared by cathodic arc technique is reported in the range of 2.1 to 2.4 eV and corresponding variation in refractive index from 2.67 to 2.46 [**40**]. DLC films obtained by PLD technique have shown optical band gap between 1.5 and 1.9 eV and an index of refraction of 2.5 [**41**]. The optical band gap of DLC films fabricated by PECVD technique is reported in the

range of 1.10 to 2.48 eV [**46**].

The carbon film consisting of dominating sp^2 bonded carbon atoms is termed as graphitic thin films. Graphitic thin films attracted attention in the field of research because of its good thermal and electrical conductivity, high transparency, biocompatibility, etc. [**47-53**]. The high thermal conductivity leads to its usage as a coating for thermal management application [**54**]. The high electrical conductivity makes it a promising candidate for transparent electrodes [**55, 56**]. These films have been also investigated as a coating for heart valves and other forms of prosthesis [**52, 57**]. Fabrication of graphite thin film, having thickness from nm to μm, on Ni substrate using CVD method was reported by Yudasaka et al. in 1994 [**58**]. The well-ordered graphitic films grown by CVD technique was also reported by Obraztsov et al., in 2007 [**59**]. Recently, pulsed laser deposition and magnetic sputtering techniques have also been used to fabricate the graphitic thin films [**60-62**].

Graphene, an another allotrope of carbon, is a material of great interest in the field of research and industry due to some of its unique properties. It is optical transparent and possesses high electron mobility, high young's modulus, thermal conductivity, etc. [**55, 63-66**]. All these properties lead to its potential applications as transparent electrodes, field emission display, biosensors, energy storage, touch screen, photovoltaic devices, photo detectors, etc. [**67-73**]. Graphene is a thermodynamically stable single atomic plane of sp^2 bonded carbon atoms (σ bonds) and considered as the building block for carbon allotropes of all other dimensionalities; graphite (3D), carbon nanotubes (2D) and fullerenes (0D). A stack of graphene layers, bonded by Vander Waal forces (π bonds), forms graphite. The in-plane and inter-plane bond length of graphite is 0.142 nm and 0.341 nm, respectively. Graphene sheets rolled up into cylindrical surface with diameter of the order of a nanometer are called carbon nanotube [**74**]. Another

nanostructure of sp^2 network is its spherical lattice, known as fullerene [**74**]. The first experimentally produced graphene was reported by Novoselov et al. in 2004 by mechanical exfoliation of highly oriented pyrolytic graphite [**75**]. Graphene was also obtained by sublimating Si from silicon carbide at high temperatures (>1100 °C) [**76**]. Further, Graphene has been prepared by several other techniques viz.; CVD, PLD, chemical synthesis, etc. [**67, 77-86**]. In 2009, Reina et al. demonstrated the growth of single- to few-layer graphene over a large area on Ni surfaces via CVD technique and transferred the films onto arbitrary substrates [**87**]. The high quality transparent few-layer graphene (FLG) onto Ni substrate at the substrate temperature in the range of 1100-1300 °C using PLD technique was reported by Zhang et al. in 2010 [**88**].

1.1 Pulsed laser deposition technique

Pulsed laser deposition is a simple and versatile technique for the growth of wide variety of thin films of metals, semiconductors, ceramic, composite etc. [**89-96**]. Some of the advantages offered by PLD technique over other deposition techniques are listed below:

(a) Stoichiometric growth of thin films [**97-100**].

(b) Control over the physical and chemical properties of thin film by proper choice of deposition parameters; laser wavelength, pulse duration, laser fluence, deposition temperature, background gas pressure, target to substrate distance, etc. [**43, 101-107**].

(c) Fabrication of hydrogen-free DLC films [**43, 108**].

(d) Growth of multicomponent and multilayer thin films [**109-111**].

The PLD films deposited using shorter laser wavelength possess low surface roughness [**94, 102**]. The laser fluence affects the lattice constant and defect structure of

the grown films [**97, 99**]. The elevated substrate temperatures favours the transformation of target stoichiometry onto the film as well as it enhances the uniformity over deposited area [**90**]. The presence of background gas encourages the formation of nanoparticles and epitaxial growth [**91, 92**]. The size of particulates on the film surface also can be controlled by the target to substrate distance [**94, 95**]. The PLD films sometime could be rough due to the deposition of large sized particulates or the liquid droplets particularly in case of pure metallic films. This can be avoided by suitably adjusting the deposition parameters [**89**]. Another limitation of PLD technique is non-uniform deposition over large area which can be overcome by rastering of substrate or scanning the laser beam over the target or both [**109, 112**].

PLD technique was first proposed by Smith and Turner in 1965 [**113**]. Later, since 1980 this technique had emerged as a powerful deposition tool for the fabrication of various materials, multilayer, nanostructures.

The schematic diagram of PLD system is shown in *Figure 1.2*. It consists of a multiport vacuum chamber having a programmable target holder, substrate holder and viewport for focusing the laser beam onto the target. The PLD chamber is initially evacuated to a base pressure of ~ 10^{-6} mbar and if required, it can be pressurised with the desired background gas. In PLD technique, a high power pulsed laser is focused onto a

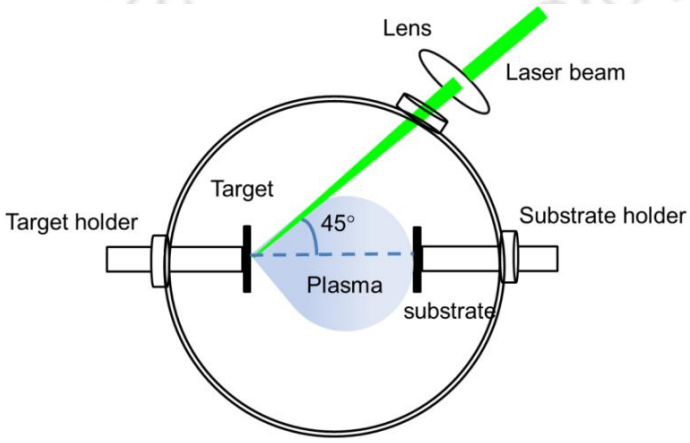

Figure 1.2: *Schematic of pulsed laser ablation chamber.*

target through a view port, as shown in *Figure 1.2*. Normally, nano-second pulsed lasers; Nd:YAG or excimer lasers, are used for thin film fabrication which provides the irradiance of $>10^8$ W/cm^2 [**89, 95, 97-99, 104, 114**]. In this regime, the laser energy induces multi-photon ionization of the target material [**115**]. This results in the formation of laser induced plasma (LIP) of the target material consisting of ions, electrons and neutrals. At the early stage of the laser pulse, the plasma plume expansion depends on the ambient gas pressure, laser fluence, laser focal spot on the target, etc. [**91, 94, 95, 116-118**]. The expanding plasma adjacent to the target surface interacts with the later part of laser pulse and absorbs the laser energy via inverse bremsstrahlung process leading to further ionization of the plasma species as well as increases its temperature [**91, 115**]. At such high temperature, the plume pressure increases to more than 5-10 bars. The pressure gradient between the plasma plume near the target surface and the chamber ambient drives the plasma species away from the target with the expansion velocity of the order of 10^3-10^5 m/s [**117, 119-122**]. After termination of the laser pulse, the thermal energy is converted into kinetic energy and the plasma cools down rapidly. In case of gaseous ambient, the gas molecules may undergo ionization through collision of highly energetic plasma species. If the laser intensity is sufficiently high then there is also a direct ionization of ambient gas atoms/molecules. During the expansion, the target plasma undergoes dynamical and chemical changes due to the interaction with the plasma of ambient gas and/or gas molecules which is followed by the formation of molecular species [**118, 123, 124**]. These molecular species condenses and nucleates onto substrate (placed at a few centimetres away from the target in the direction of plasma expansion) which favours the film growth. The growth of the thin film depends on the LIP dynamics, substrate surface energy as well as the lattice orientation of the substrate. The growth mechanism of thin film in PLD can be understood by the

thermodynamic parameters; substrate temperature (T) and plasma flux supersaturation (Δm). These two parameters are related by $\Delta m = k_B T \ln(R/R_e)$, where k_B is Boltzmann constant, R is actual deposition rate and R_e is equilibrium deposition rate [**125**]. In PLD process, the plasma flux supersaturation is of the order of 10^5 J/mol. Such high degree of supersaturation leads to two dimensional nucleation with monoatomic height which favours the layer by layer growth of the film. The high kinetic energy of plasma species provides the formation of good quality thin films even at room temperature (RT) compared to that of other techniques. In addition, the film properties are governed by various deposition parameters; laser wavelength, irradiance of the laser onto the target surface, target to substrate distance, nature of ambient, ambient gas pressure, substrate temperature and quality of the target [**94, 95, 102, 105-107**].

1.2 Characterization of carbon thin films

1.2.1 Raman spectroscopy

Raman spectroscopy is a powerful and non-destructive tool for the characterization of crystalline, nanocrystalline and amorphous carbon [**126-128**]. The single crystal graphite exhibits Raman peak at ~1575 cm^{-1}, which is attributed to the Raman active E_{2g} mode of graphite [**129**]. This E_{2g} mode of graphite is commonly referred to as the G band, which appears in all sp^2 hybridized carbon materials including

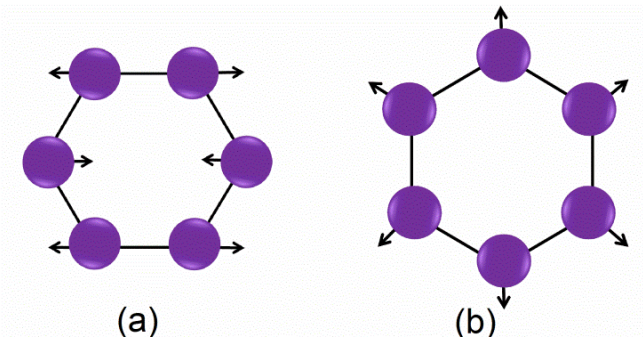

***Figure 1.3**: Illustration of Vibration mode of **(a)** G band and **(b)** D band.*

amorphous carbon, graphene, carbon nanotube etc. The vibration mode of G band involves in-plane bond-stretching motion of pairs of sp^2 carbon atoms as shown in *Figure 1.3 (a)* [**126**]. The Raman spectrum of diamond has a Raman shift of ~1332 cm^{-1} corresponding to T_{2g} zone centre mode [**130**]. Amorphous carbon containing microcrystalline graphite shows Raman shift at ~1355 cm^{-1} other than the G band. This Raman mode of amorphous carbon corresponds to A_{1g} symmetry and is assigned as the D band, activated from the structural disorder due to the finite crystallite size [**126, 131**]. The D band involves in-plane breathing mode in carbon rings as shown in *Figure 1.3 (b)* [**126**]. The visible Raman spectra of nanocrystalline and amorphous carbon are dominated by G and D bands of sp^2 sites. This is due to the larger cross section of π states of sp^2 sites [**132, 133**]. In amorphous carbon, the Raman shift of G band always lies in the range of 1500-1630 cm^{-1}. The peak position, line width and the intensity of G and D bands depend on the ratio of sp^3 and sp^2 bonded carbon atoms.

Raman spectra of graphite, few-layer graphene, natural diamond, DLC film and glassy carbon are shown in *Figure 1.4-1.8,* respectively.

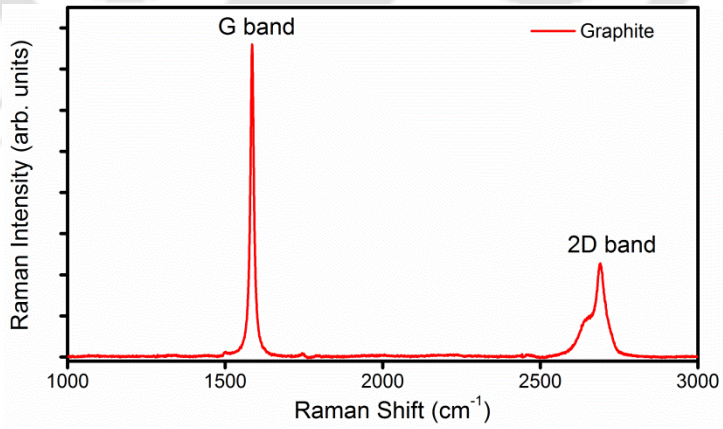

Figure 1.4*: Raman spectrum of graphite.*

The Raman spectrum of *Figure 1.4* shows the G band at ~1580 cm^{-1} and 2D band at ~ 2730 cm^{-1} as first- and second-order Raman features, respectively, of graphite [**134**]. The absence of D band at ~1350 cm^{-1} reflects that the graphite is defect-free.

Figure 1.5 shows the Raman spectrum of FLG fabricated by PLD technique [**135**]. The spectrum consists of D, G and 2D bands at 1355 cm^{-1}, 1584 cm^{-1} and 2730 cm^{-1}, respectively. As 2D band originates from the in-plane breathing mode of carbon rings like D band but involves two phonons in the process and hence the Raman shift for 2D band is twice that of the D band. The symmetry of 2D band around the peak, *Figure 1.5*, compared to that of graphite (*Figure 1.4*) is a signature of FLG. In addition to these bands, the Raman spectrum of FLG has a weak (less intensity) band at ~ 2450 cm^{-1} termed as G* band which is due to the two phonon process [**136**].

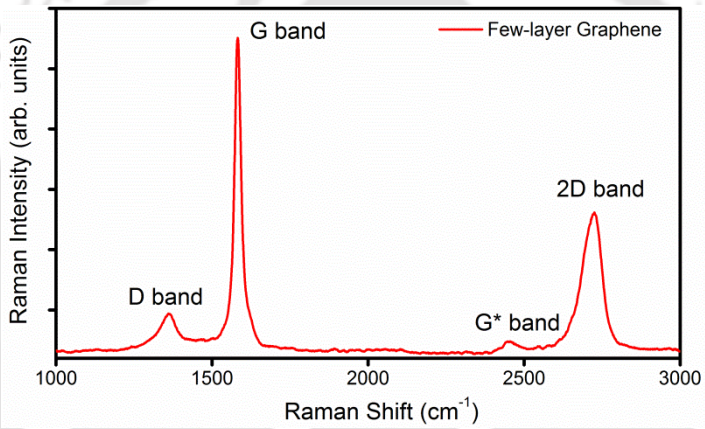

Figure 1.5: *Raman spectrum of few-layer graphene.*

The Raman spectrum of natural diamond is shown in *Figure 1.6* which has a prominent peak at ~1333 cm^{-1} (FWHM: ~ 3 cm^{-1}) corresponds to the triply degenerate zone centre optical phonon in T_{2g} symmetry [**130**].

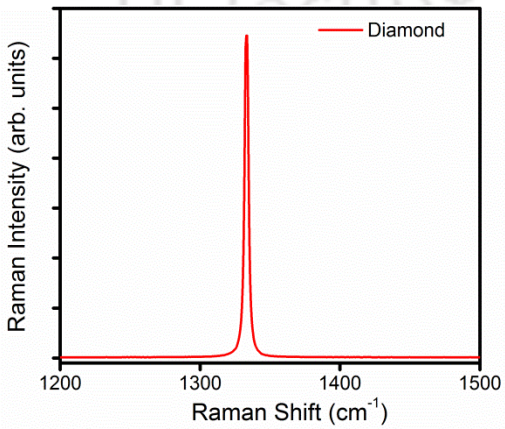

Figure 1.6: *Raman spectrum of natural diamond.*

In case of DLC, Raman spectrum shows a broad band centred at ~1550 cm^{-1} with an asymmetric tail extending towards lower wavenumber, *Figure 1.7* [**137, 138**]. The downward shift of the Raman peak of G band w.r.t. the graphite, 1575 cm^{-1}, is due to the decrease in average C-C bond angle and is proportional to the percentage of sp^3 bonded carbon atoms [**139**]. The peak position of G band shifts towards higher wavenumber with the decrease in excitation laser wavelength for disordered carbon [**137**]. The estimation of sp^3/sp^2 ratio of carbon bonding in DLC films can be made by using *Equation (1.1)* [**140**].

$$sp^3 \ content = -0.07 + 2.50 \times Dispersion(G)[cm^{-1} / nm] \pm 0.06 \qquad (1.1)$$

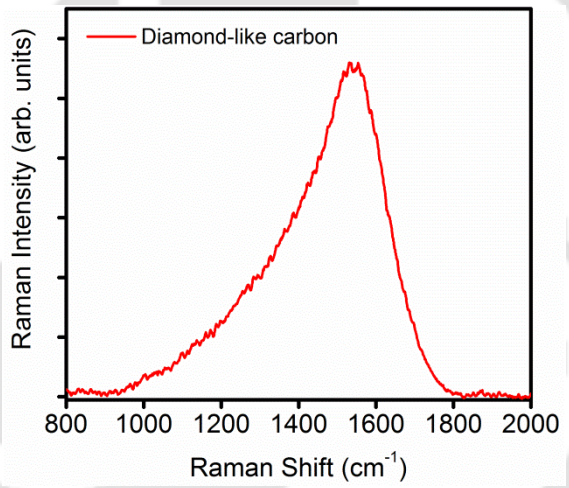

***Figure 1.7**: Raman spectrum of DLC thin film.*

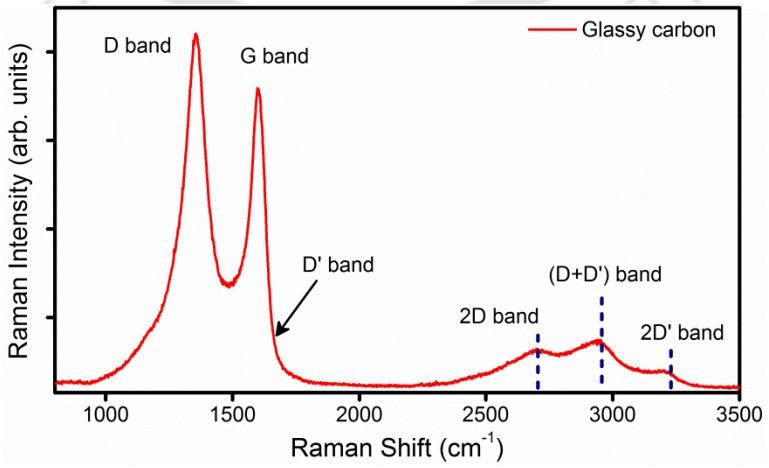

***Figure 1.8**: Raman spectrum of glassy carbon thin film.*

Glassy carbon is a graphitized material with high defects. It is characterized by the distinct D and G Raman bands which are broader than that of graphite. Due to defects in glassy carbon and its highly graphitic nature, its Raman spectrum, *Figure 1.8*, exhibits several other bands; D', (D+D') and 2D'. The D' band is one phonon process and appears at ~1620 cm^{-1} which can be distinguished from G band after deconvolution [**141**]. 2D' band (~3206 cm^{-1}) is overtone of D' band and is due to the two phonon process whereas (D+D') band (~2940 cm^{-1}) is a combination of D and D' bands [**141**].

1.2.2 Ultraviolet-visible (UV-Vis) spectroscopy

UV-Vis spectroscopy refers to transmission/absorption/reflectance spectroscopy in the ultraviolet-visible spectral region and is used to determine the absorption coefficient and band gap of a thin film. The UV-Visible spectrum of the films having thickness greater than 100 nm shows the interference fringes which is used to determine the film thickness and refractive index using Swanepoel envelope method [**142**]. Thin film of highly reflecting surface and thickness less than 100 nm show transmission spectrum which are normally free from any signature of interference fringes and hence absorption coefficient obtained from the transmission or the absorption spectrum possess large errors and the film thickness can't be measured. For such samples, spectroscopic ellipsometer is used for the determination of absorption coefficient and other optical constants with precision.

1.2.3 Spectroscopic ellipsometry

Spectroscopic ellipsometer (SE) is a powerful tool to determine the absorption coefficient, film thickness, optical band gap energy and refractive index of the reflecting films [**143, 144**]. It is even applicable to the thin films of very small thickness (< 100 nm) where Swanepoel envelope approximation can't be applied due to non-appearance of

the interference fringes or poor fringe visibility of UV-Visible transmission spectrum. In this technique, the change in polarization state of the reflected light with respect to the

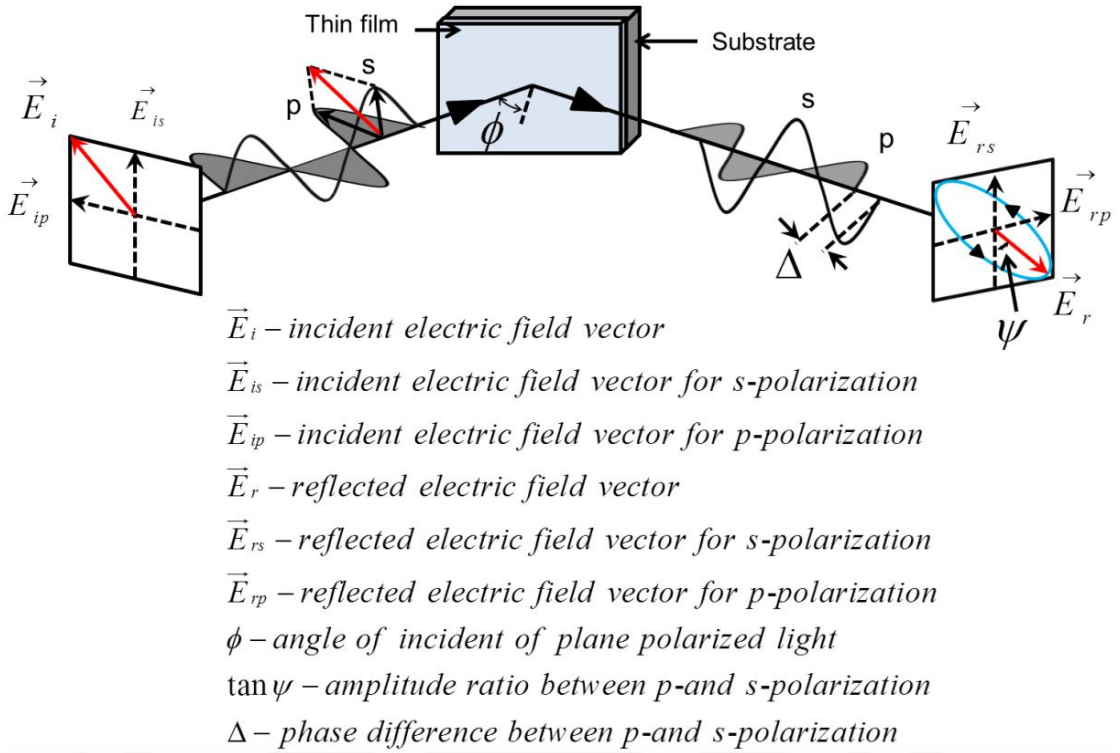

Figure 1.9: *Reflection of polarized light on film-substrate surface and geometrical interpretation of ellipsometer parameters (ψ, Δ).*

incident light is measured as a function of frequency (or wavelength). *Figure 1.9* shows the schematic of working principle of an ellipsometer. The parameters 'ψ' is defined in *Figure 1.10* and is given as $\tan\psi = |r_p|/|r_s|$, where $|r_p| = \left|\vec{E}_{rp}\right| \Big/ \left|\vec{E}_{ip}\right|$ and $|r_s| = \left|\vec{E}_{rs}\right| \Big/ \left|\vec{E}_{is}\right|$ are the amplitude of reflection coefficient for *p*- and *s*- polarizations, respectively. For linearly polarized incident light oriented at 45°, $\left|\vec{E}_{ip}\right| = \left|\vec{E}_{is}\right|$ and therefore, $\tan\psi = |r_p|/|r_s| = \left|\vec{E}_{rp}\right| \Big/ \left|\vec{E}_{rs}\right|$. The *p*- and *s*- polarized light waves are the parallel and perpendicular components of the electric field vector of the light wave with respect to the plane of incidence. The another parameter 'Δ' determines the phase difference between

reflected *p*- and *s*- polarized light waves, $\Delta = \delta_p - \delta_s$ where δ_p and δ_s are the phase of reflected *p*- and *s*- polarized light waves, respectively.

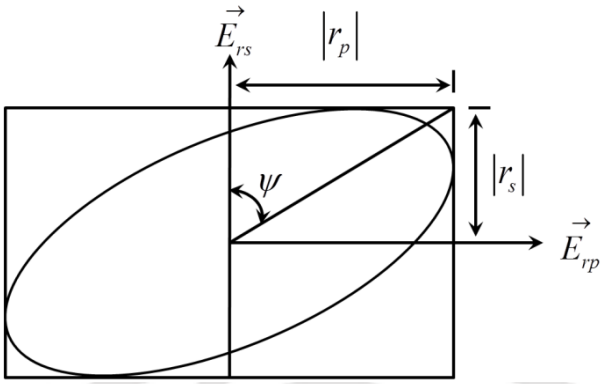

Figure 1.10: *Geometrical interpretation of parameter r_p and r_s*

The ellipsometer parameters 'ψ' and 'Δ' are related to each other by *Equation (1.2*) which is known as ellipsometer equation [**145**].

$$\rho = \frac{r_p}{r_s} = \tan\psi \exp(i\Delta) \tag{1.2}$$

where, ρ is Fresnel reflection coefficient. From the *Equation (1.2)*, the pseudo dielectric function is obtained using *Equation (1.3)* [**145**].

$$\varepsilon(\omega) = \sin^2\phi\left[1 + \tan^2\phi\left(\frac{1-\rho}{1+\rho}\right)^2\right] \tag{1.3}$$

where, ϕ is the angle of incidence of the plane polarized light with respect to the sample surface as depicted in *Figure (1.9)*. From *Equation (1.3)*, real and imaginary part of the dielectric constant can be defined as $\varepsilon(\omega) = \varepsilon_1(\omega) + i\varepsilon_2(\omega)$ .The pseudo dielectric function contains the substrate features along with that of thin film which can be separated out by using appropriate dispersion model. For amorphous carbon film, various dispersion models have been used including Tauc Lorentz, Forouhi Bloomer (FB) model and modified FB model (mFB) [**146-148**]. The refractive index '*n*', extinction coefficient '*k*' and absorption coefficient 'α' can be obtained from complex dielectric function ε_1

and ε_2 using *Equations (1.4)-(1.6)*, respectively [**145**]:

$$n = \left\{ \frac{1}{2} \left[\varepsilon_1 + \left(\varepsilon_1^2 + \varepsilon_2^2 \right)^{1/2} \right] \right\}^{1/2} \tag{1.4}$$

$$k = \left\{ \frac{1}{2} \left[-\varepsilon_1 + \left(\varepsilon_1^2 + \varepsilon_2^2 \right)^{1/2} \right] \right\}^{1/2} \tag{1.5}$$

$$\alpha = \frac{4\pi k}{\lambda} \tag{1.6}$$

The mFB model includes all the possible band transitions of amorphous structure and hence adopted to fit the SE data of DLC films in the present thesis [**149**].

1.2.4 Fourier transform infrared spectroscopy

Fourier Transform Infrared (FTIR) spectroscopy is a technique for investigating the bonding structure based on the absorption of infrared photons by the molecule. In the amorphous carbon, an absorption band appears in the range of 900-1800 cm^{-1} which is due to the delocalized π-electrons associated with sp^2 bonded carbon atoms [**150-153**]. The absorption band in the range of 2800-3300 cm^{-1} is a signature of the presence of hydrogen [**154**]. The vibration modes of C-H bond for sp^3 and sp^2 configurations lie in the range of 2850-2955 cm^{-1} and 2975-3085 cm^{-1}, respectively [**2, 154**]. The *sp* bonded

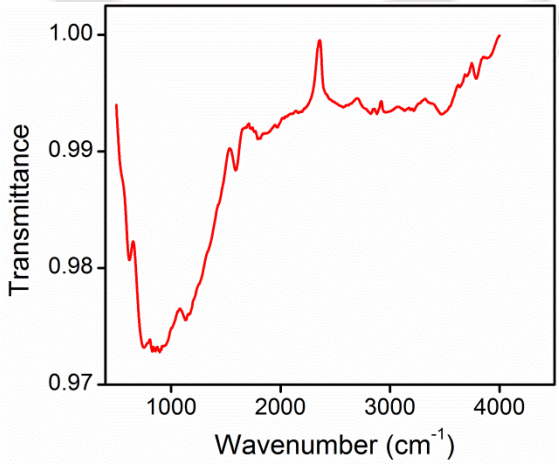

Figure 1.11: *FTIR spectrum of hydrogen-free DLC thin film.*

C-H vibration mode has a center at 3300 cm^{-1} **[2]**. The IR spectrum of hydrogen-free amorphous carbon is shown in *Figure 1.11* where there is hardly any appearance of the band in the range of 2800-3300 cm^{-1}.

1.2.5 X-ray diffraction

X-ray diffraction (XRD) is a non-destructive technique for characterizing the crystalline material and investigating atomic arrangement, crystallite size and type of crystallinity. As DLC is amorphous in nature, the XRD spectra of the film deposited on glass substrate shows a broad peak lying in the range of 2θ ~10°-30° which is originating from the substrate [**155**]. However, the XRD spectra of DLC films having diamond crystallites exhibit diffraction peaks at ~43.20°, ~74.06°, ~89.90° and ~95.57° whereas the graphitic crystallites shows the diffraction peaks at ~26.30° and ~50.36° [**156, 157**].

1.3 Optical nonlinearity in carbon based thin films

Nonlinear optical properties of materials are of great importance in various optical devices [**158-161**]. Carbon nanostructures; carbon nanotubes, graphene, graphene oxide, carbon black, onion-like carbon, fullerenes, diamond, etc. exhibit nonlinear optical (NLO) properties [**158, 162-170**]. The single wall carbon nanotubes showed the reverse saturation absorption behaviour at the laser wavelength of 532 nm and exhibits negative value of nonlinear refractive index coefficient, n_2 [**162**]. Multiwall carbon nanotubes in ethylene glycol (0.4 mg/ml) exhibit reverse saturation effect and positive value of n_2 under picosecond laser (532 nm) illumination [**163**]. Few-layer graphene fabricated by CVD exhibits saturation behaviour under the irradiance of picosecond laser at a wavelength of 1550 nm [**164**]. Diamond exhibits positive nonlinear refractive index coefficient (n_2) at a laser wavelength of 1064 nm and 532 nm whereas in case of laser wavelength of 355 nm and 266 nm it shows negative n_2 [**168**]. The reverse saturation

absorption is reported in linear carbon chains at a wavelength of 532 nm from nanosecond laser [**169**]. The NLO behaviour of carbon materials enable them to act as an optical limiter [**158, 159**]. The optical limiting in carbon black suspension, onion-like carbon, fullerenes and diamond nanoparticles have been reported in the literature [**158, 166, 167**]. The optical limiting action is the result of a number of mechanisms which includes nonlinear absorption, nonlinear scattering and nonlinear refraction [**158, 171, 172**]. One of the most important applications of optical limiting property is to protect the optical elements, human eyes and optical sensors from intense laser beam [**173-175**]. Another application of NLO behaviour of graphene and carbon nanotube is in mode locking of a laser [**160, 176-178**].

A variety of techniques have been developed to measure the nonlinear optical properties of materials. These techniques include nonlinear interferometry, degenerate four-wave mixing, ellipse rotation, *Z*-scan technique and beam distortion measurements [**161, 179-182**]. The first three techniques are sensitive but require relatively complex experimental setup whereas the beam distortion measurement is relatively less sensitive and need detailed wave propagation analysis. *Z*-scan technique involves comparatively simple experimental setup. The *Z*-scan technique, proposed by Sheik-Bahae et al. in 1989, is a single beam scan method and based on the spatial beam distortion during beam propagation through the nonlinear medium [**181**]. In this technique, the sample is translated longitudinally along the optic axis of a focused Gaussian laser beam. The translation of the sample leads to the change of irradiance at the sample, resulting in changes in the intensity dependent optical properties. The intensity transmitted through the sample is recorded as a function of sample location 'z' with respect to the focal plane. The plot of transmitted intensity as a function of 'z' gives the information about the order of the nonlinearity as well as its sign and magnitude. The technique includes open

aperture (OA) and closed aperture (CA) Z-scan measurements which determine nonlinear absorption (NLA) coefficient and nonlinear refractive index (NLR) coefficient, respectively. The experimental setup is explained in *Chapter 2, Section 2.2*. In the present thesis, the conventional *Z*-scan setup was modified so as to obtain the OA and CA data from the single scan. The details are presented in *Chapter 6*.

1.4 Organization of present thesis

DLC thin films and graphene have numerous applications. To preserve the quality of DLC coating at high temperature, it should be hydrogen-free and therefore the present thesis aims towards the fabrication of hydrogen-free DLC films having higher fraction of sp^3 bonded carbon atoms via PLD technique. Different forms of DLC films are distinguished by Raman spectroscopy. To extract the information for the carbon bonding ratio and its configuration, the Raman spectrum should have high signal to noise ratio which can be achieved by using the high laser intensity in Raman system. But excessive laser intensity may cause the local heating in the focal region and the film may undergo thermally induced structural modification and therefore the information extracted from the Raman spectrum will be deviated compared to that of the as-deposited film. Therefore, the present thesis also includes the effect of laser intensity on the Raman spectrum and hence structural changes in DLC film.

Graphene, another important allotrope of carbon, fabricated by most of techniques involves the catalytic metal and then transferring it on the desired substrate which induces defects. It is very important to reduce the defects in graphene for practical applications. Hence, in the present thesis, single step fabrication of few-/multi-layer graphene on glass substrate via PLD is demonstrated. The work is extended to the study of NLO behaviour of DLC and graphitic thin films. To study the NLO behaviour of the

PLD film, the conventional *Z*-scan setup was modified by replacing the photodiode detector with CCD camera and the hard aperture by the synthetic aperture using a matlab program.

The present thesis is organized into following eight chapters:

Chapter 1, the first chapter "*Introduction*", contains the overview of the literature survey on DLC films and graphene, basic of PLD technique, various characterization tools and the nonlinear optical properties of carbon materials.

Chapter 2, "*Experimental details*", describes the PLD setup used for fabrication of DLC and graphitic thin films and few-/multi-layer graphene. It also briefly demonstrates the modified *Z*-scan setup to measure the NLA and NLR coefficients of carbon films. The basic information of various commercial instruments used for the characterization of PLD films is also included in this chapter.

Chapter 3, "*Effect of cw laser irradiation on DLC films*", presents the effect of laser intensity during recording of Raman spectra and degree of graphitization of DLC film with laser irradiation to assess the optimum laser intensity to be used without any significant structural modification of DLC film due to heating effect of the laser.

Chapter 4, "*Characterization of pulsed laser deposited DLC and graphitic thin films*", includes the effect of substrate temperature, background helium pressure and laser fluence on sp^3 content of DLC films as well as their linear optical properties.

Chapter 5, "*Fabrication and characterization of few- and multi-layer graphene via PLD technique*", documents the deposition parameters and characterizations of few- and multi-layer graphene.

Chapter 6, "*Modified Z-scan setup using CCD camera*", demonstrates CCD as a detector for recording the open as well as closed aperture *Z*-scan in a single scan to measure NLA and NLR coefficients.

Chapter 7, "*Optical nonlinearity in pulsed laser deposited DLC and graphitic thin films*", includes the measurement of NLA and NLR coefficients of DLC and graphitic thin films by modified *Z*-scan setup.

Chapter 8, the last chapter "*Conclusion*" summarizes the salient features of the present research work. It also discusses the possibilities of future exploration of the present research work.

Bibliography

[**1**] S.R.P. Silva (ed.), "Properties of Amorphous Carbon ", *INSPEC ,The Institution of Electrical Engineers*, London ,United Kingdom, 2003.

[**2**] J. Robertson, "Diamond-like amorphous carbon", *Materials Science and Engineering R*, **37** (2002) 129-281.

[**3**] S. Xu, D. Flynn, B.K. Tay, S. Prawer, K.W. Nugent, S.R.P. Silva, Y. Lifshitz, W.I. Milne, "Mechanical properties and Raman spectra of tetrahedral amorphous carbon films with high sp^3 fraction deposited using a filtered cathodic arc", *Philosophical Magazine B*, **76** (1997) 351-361.

[**4**] M. Jarratt, J. Stallard, N.M. Renevier, D.G. Teer, "An improved diamond-like carbon coating with exceptional wear properties", *Diamond and Related Materials*, **12** (2003) 1003-1007.

[**5**] M. Shamsa, W.L. Liu, A.A. Balandin, C. Casiraghi, W.I. Milne, A.C. Ferrari, "Thermal conductivity of diamond-like carbon films", *Applied Physics Letters*, **89** (2006) 161921.

[**6**] P. Patsalas, "Optical properties of amorphous carbons and their applications and perspectives in photonics", *Thin Solid Films*, **519** (2011) 3990-3996.

[**7**] K. Kanda, S. Takehana, S. Yoshida, R. Watanabe, S. Takano, H. Ando, F. Shimakura, "Application of diamond-coated cutting tools", *Surface and Coatings Technology*, **73** (1995) 115-120.

[**8**] A.C. Ferrari, "Diamond-like carbon for magnetic storage disks", *Surface and Coatings Technology*, **180–181** (2004) 190-206.

[**9**] C.A. Love, R.B. Cook, T.J. Harvey, P.A. Dearnley, R.J.K. Wood, "Diamond like carbon coatings for potential application in biological implants—a review", *Tribology International*, **63** (2013) 141-150.

[**10**] A.H. Lettington, "Applications of diamond-like carbon thin films", *Carbon*, **36** (1998) 555-560.

[**11**] W.S. Choi, K. Kim, J. Yi, B. Hong, "Diamond-like carbon protective anti-reflection coating for Si solar cell", *Materials Letters*, **62** (2008) 577-580.

[**12**] W.I. Milne, "Electronic devices from diamond-like carbon", *Semiconductor Science and Technology*, **18** (2003) S81-S85.

[**13**] W. Jacob, W. Möller, "On the structure of thin hydrocarbon films", *Applied Physics Letters*, **63** (1993) 1771-1773.

[**14**] J.E. Field, "Properties of Diamond", *Academic Press*, London, 1993.

[**15**] B.T. Kelly, "Physics of Graphite", *Applied Science Publishers*, London, 1981.

[**16**] M.S. Dresselhaus, G. Dresselhaus, P.C. Eklund, "Science of Fullerenes and Carbon Nanotubes", *Academic Press*, London, 1996.

[**17**] J. Robertson, "Amorphous carbon", *Advances in Physics*, **35** (1986) 317-374.

[**18**] G.M. Pharr, D.L. Callahan, S.D. McAdams, T.Y. Tsui, S. Anders, A. Anders, J.W. Ager, I.G. Brown, C.S. Bhatia, S.R.P. Silva, J. Robertson, "Hardness, elastic modulus, and structure of very hard carbon films produced by cathodic-arc deposition with substrate pulse biasing", *Applied Physics Letters*, **68** (1996) 779-781.

[**19**] D.R. McKenzie, "Tetrahedral bonding in amorphous carbon", *Reports on Progress in Physics*, **59** (1996) 1611.

[**20**] P.J. Fallon, V.S. Veerasamy, C.A. Davis, J. Robertson, G.A.J. Amaratunga, W.I. Milne, J. Koskinen, "Properties of filtered-ion-beam-deposited diamondlike carbon as a function of ion energy", *Physical Review B*, **48** (1993) 4777-4782.

[**21**] P. Koidl, C. Wild, B. Dischler, J. Wagner, M. Ramsteiner, "Plasma deposition, properties and structure of amorphous hydrogenated carbon films", *Materials Science Forum*, **52-53** (1991) 41-70.

[**22**] M. Weiler, S. Sattel, K. Jung, H. Ehrhardt, V.S. Veerasamy, J. Robertson, "Highly tetrahedral, diamond-like amorphous hydrogenated carbon prepared from a plasma beam source", *Applied Physics Letters*, **64** (1994) 2797-2799.

[**23**] http://www.appliednanotech.net/tech/graphene_films.php

[**24**] S. Aisenberg, R. Chabot, "Ion-Beam deposition of thin films of diamondlike carbon", *Journal of Applied Physics*, **42** (1971) 2953-2958.

[**25**] S. Aisenberg, R.W. Chabot, "Physics of ion plating and ion beam deposition", *Journal of Vacuum Science & Technology*, **10** (1973) 104-107.

[**26**] D.S. Whitmell, R. Williamson, "The deposition of hard surface layers by hydrocarbon cracking in a glow discharge", *Thin Solid Films*, **35** (1976) 255-261.

[**27**] L. Holland, "Some characteristics and uses of low-pressure plasmas in materials science", *Journal of Vacuum Science & Technology*, **14** (1977) 5-15.

[**28**] L. Holland, S.M. Ojha, "Deposition of hard and insulating carbonaceous films on an r.f. target in a butane plasma", *Thin Solid Films*, **38** (1976) L17-L19.

[**29**] K. Enke, H. Dimigen, H. Hübsch, "Frictional properties of diamondlike carbon layers", *Applied Physics Letters*, **36** (1980) 291-292.

[**30**] K. Enke, "Some new results on the fabrication of and the mechanical, electrical and optical properties of i-carbon layers", *Thin Solid Films*, **80** (1981) 227-234.

[**31**] A. Bubenzer, B. Dischler, G. Brandt, P. Koidl, "rf-plasma deposited amorphous hydrogenated hard carbon thin films: Preparation, properties, and applications", *Journal of Applied Physics*, **54** (1983) 4590-4595.

[**32**] A. Bubenzer, B. Dischler, A. Nyaiesh, "Optical properties of hydrogenated hard carbon thin films", *Thin Solid Films*, **91** (1982) 81-87.

[**33**] W. Pompe, H.J. Scheibe, P. Siemroth, R. Wilberg, D. Schulze, B. Bücken, "Film deposition by laser-arcs", *Thin Solid Films*, **208** (1992) 11-14.

[**34**] H.J. Scheibe, P. Siemroth, "Film deposition by laser-induced vacuum arc evaporation", *IEEE Transactions on Plasma Science*, **18** (1990) 917-922.

[**35**] Y. Lifshitz, "Diamond-like carbon — present status", *Diamond and Related Materials*, **8** (1999) 1659-1676.

[**36**] H. Hofsäss, H. Binder, T. Klumpp, E. Recknagel, "Doping and growth of diamond-like carbon films by ion beam deposition", *Diamond and Related Materials*, **3** (1993) 137-142.

[**37**] F. Jansen, M. Machonkin, S. Kaplan, S. Hark, "The effects of hydrogenation on the properties of ion beam sputter deposited amorphous carbon", *Journal of Vacuum Science & Technology A*, **3** (1985) 605-609.

[**38**] S. Logothetidis, "Hydrogen-free amorphous carbon films approaching diamond prepared by magnetron sputtering", *Applied Physics Letters*, **69** (1996) 158-160.

[**39**] M.C. Polo, J.L. Andújar, A. Hart, J. Robertson, W.I. Milne, "Preparation of tetrahedral amorphous carbon films by filtered cathodic vacuum arc deposition", *Diamond and Related Materials*, **9** (2000) 663-667.

[**40**] R. Lossy, D.L. Pappas, R.A. Roy, J.P. Doyle, J.J. Cuomo, J. Bruley, "Properties of amorphous diamond films prepared by a filtered cathodic arc", *Journal of Applied Physics*, **77** (1995) 4750-4756.

[**41**] D.L. Pappas, K.L. Saenger, J. Bruley, W. Krakow, J.J. Cuomo, T. Gu, R.W. Collins, "Pulsed laser deposition of diamond-like carbon films", *Journal of Applied Physics*, **71** (1992) 5675-5684.

[**42**] M. Tabbal, P. Mérel, M. Chaker, M.A. El Khakani, E.G. Herbert, B.N. Lucas, M.E. O'Hern, "Synthesis of diamond-like-carbon coatings by pulsed laser deposition: optimization of process parameters", *Surface and Coatings Technology*, **116–119** (1999) 452-455.

[**43**] Y. Miyajima, S.J. Henley, G. Adamopoulos, V. Stolojan, E. Garcia-Caurel, B. Drévillon, J.M. Shannon, S.R.P. Silva, "Pulsed laser deposited tetrahedral amorphous carbon with high sp^3 fractions and low optical bandgaps", *Journal of Applied Physics*, **105** (2009) 073521.

[**44**] S. Iijima, Y. Aikawa, K. Baba, "Early formation of chemical vapor deposition diamond films", *Applied Physics Letters*, **57** (1990) 2646-2648.

[**45**] N.M.S. Marins, R.P. Mota, R.Y. Honda, P.A.P. Nascente, M.E. Kayama, K.G. Kostov, M.A. Algatti, N.C. Cruz, E.C. Rangel, "Properties of hydrogenated amorphous carbon films deposited by PECVD and modified by SF_6 plasma", *Surface and Coatings Technology*, **206** (2011) 640-645.

[**46**] M.L. Theye, V. Paret, A. Sadki, "Relations between the deposition conditions, the microstructure and the defects in PECVD hydrogenated amorphous carbon films; influence on the electronic density of states", *Diamond and Related Materials*, **10** (2001) 182-190.

[**47**] Q. Zheng, P.V. Braun, D.G. Cahill, "Thermal conductivity of graphite thin films grown by low temperature chemical vapor deposition on Ni (111)", *Advanced Materials Interfaces*, **3** (2016) 1600234.

[**48**] X. Tian, M.E. Itkis, E.B. Bekyarova, R.C. Haddon, "Anisotropic thermal and electrical properties of thin thermal interface layers of graphite nanoplatelet-based composites", *Scientific Reports*, **3** (2013) 1710.

[**49**] S. Yamanaka, T. Nishino, T. Fujimoto, Y. Kuga, "Production of thin graphite sheets for a high electrical conductivity film by the mechanical delamination of ternary graphite intercalation compounds", *Carbon*, **50** (2012) 5027-5033.

[**50**] A.P. Graham, G. Schindler, G.S. Duesberg, T. Lutz, W. Weber, "An investigation of the electrical properties of pyrolytic carbon in reduced dimensions: Vias and wires", *Journal of Applied Physics*, **107** (2010) 114316.

[**51**] G.I. Dovbeshko, V.R. Romanyuk, D.V. Pidgirnyi, V.V. Cherepanov, E.O. Andreev, V.M. Levin, P.P. Kuzhir, T. Kaplas, Y.P. Svirko, "Optical properties of pyrolytic carbon films versus graphite and graphene", *Nanoscale Research Letters*, **10** (2015) 234.

[**52**] V. PesÁkovÁ, Z. Kle´zl, K. Bali´k, M. Adam, "Biomechanical and biological properties of the implant material carbon-carbon composite covered with pyrolytic carbon", *Journal of Materials Science: Materials in Medicine*, **11** (2000) 793-798.

[**53**] T. Kaplas, P. Kuzhir, "Ultra-thin graphitic film: synthesis and physical properties", *Nanoscale Research Letters*, **11** (2016) 54.

[**54**] C.-Y. Wen, G.-W. Huang, "Application of a thermally conductive pyrolytic graphite sheet to thermal management of a PEM fuel cell", *Journal of Power Sources*, **178** (2008) 132-140.

[**55**] W. Cai, Y. Zhu, X. Li, R.D. Piner, R.S. Ruoff, "Large area few-layer graphene/graphite films as transparent thin conducting electrodes", *Applied Physics Letters*, **95** (2009) 123115.

[**56**] A. Mukhopadhyay, A. Tokranov, K. Sena, X. Xiao, B.W. Sheldon, "Thin film graphite electrodes with low stress generation during Li-intercalation", *Carbon*, **49** (2011) 2742-2749.

[**57**] H. Brückmann, K.J. Hüttinger, "Carbon, a promising material in endoprosthetics. Part 1: the carbon materials and their mechanical properties", *Biomaterials*, **1** (1980) 67-72.

[**58**] M. Yudasaka, R. Kikuchi, T. Matsui, H. Kamo, Y. Ohki, S. Yoshimura, E. Ota, "Graphite thin film formation by chemical vapor deposition", *Applied Physics Letters*, **64** (1994) 842-844.

[**59**] A.N. Obraztsov, E.A. Obraztsova, A.V. Tyurnina, A.A. Zolotukhin, "Chemical vapor deposition of thin graphite films of nanometer thickness", *Carbon*, **45** (2007) 2017-2021.

[**60**] K.T. Chaudhary, R. Qindeel, Saktioto, M.S. Hussain, J. Ali, P.P. Yupapin, "Graphite thin film deposition using laser induced plasma", *Procedia Engineering*, **8** (2011) 423-427.

[**61**] J.H. Kwak, S.S. Lee, H.J. Lee, G. Anoop, H.J. Lee, W.S. Kim, S.-W. Ryu, H.S. Kim, J.Y. Jo, "Direct growth of nano-crystalline graphite films using pulsed laser deposition with in-situ monitoring based on reflection high-energy electron diffraction technique", *Applied Physics Letters*, **108** (2016) 123107.

[**62**] D.L.C.e. Silva, L.R.P. Kassab, J.R. Martinelli, A.D.d. Santos, S.J.L. Ribeiro, M.V.d. Santos, "Characterization of thin carbon films produced by the magnetron sputtering technique", *Materials Research*, **19** (2016) 669-672.

[**63**] K.I. Bolotin, K.J. Sikes, Z. Jiang, M. Klima, G. Fudenberg, J. Hone, P. Kim, H.L. Stormer, "Ultrahigh electron mobility in suspended graphene", *Solid State Communications*, **146** (2008) 351-355.

[**64**] C. Lee, X. Wei, J.W. Kysar, J. Hone, "Measurement of the elastic properties and intrinsic strength of monolayer graphene", *Science*, **321** (2008) 385-388.

[**65**] A.A. Balandin, S. Ghosh, W. Bao, I. Calizo, D. Teweldebrhan, F. Miao, C.N. Lau, "Superior thermal conductivity of single-layer graphene", *Nano Letters*, **8** (2008) 902-907.

[**66**] R. Prasher, "Graphene spreads the heat", *Science*, **328** (2010) 185-186.

[**67**] K.S. Kim, Y. Zhao, H. Jang, S.Y. Lee, J.M. Kim, K.S. Kim, J.-H. Ahn, P. Kim, J.-Y. Choi, B.H. Hong, "Large-scale pattern growth of graphene films for stretchable transparent electrodes", *Nature*, **457** (2009) 706-710.

[**68**] M.-S. Lee, K. Lee, S.-Y. Kim, H. Lee, J. Park, K.-H. Choi, H.-K. Kim, D.-G. Kim, D.-Y. Lee, S. Nam, J.-U. Park, "High-performance, transparent, and stretchable electrodes using graphene–metal nanowire hybrid structures", *Nano Letters*, **13** (2013) 2814-2821.

[**69**] Y.D. Kim, M.-H. Bae, J.-T. Seo, Y.S. Kim, H. Kim, J.H. Lee, J.R. Ahn, S.W. Lee, S.-H. Chun, Y.D. Park, "Focused-laser-enabled p–n junctions in graphene field-effect transistors", *ACS Nano*, **7** (2013) 5850-5857.

[**70**] S. Kumar, G.S. Duesberg, R. Pratap, S. Raghavan, "Graphene field emission devices", *Applied Physics Letters*, **105** (2014) 103107.

[**71**] T. Kuila, S. Bose, P. Khanra, A.K. Mishra, N.H. Kim, J.H. Lee, "Recent advances in graphene-based biosensors", *Biosensors and Bioelectronics*, **26** (2011) 4637-4648.

[**72**] E. Yoo, J. Kim, E. Hosono, H.-s. Zhou, T. Kudo, I. Honma, "Large reversible Li storage of graphene nanosheet families for use in rechargeable lithium ion batteries", *Nano Letters*, **8** (2008) 2277-2282.

[**73**] F. Bonaccorso, Z. Sun, T. Hasan, A.C. Ferrari, "Graphene photonics and optoelectronics", *Nature Photonics*, **4** (2010) 611-622.

[**74**] A.K. Geim, K.S. Novoselov, "The rise of graphene", *Nature Materials*, **6** (2007) 183-191.

[**75**] K.S. Novoselov, A.K. Geim, S.V. Morozov, D. Jiang, Y. Zhang, S.V. Dubonos, I.V. Grigorieva, A.A. Firsov, "Electric field effect in atomically thin carbon films", *Science*, **306** (2004) 666-669.

[**76**] J. Hass, R. Feng, T. Li, X. Li, Z. Zong, W.A. de Heer, P.N. First, E.H. Conrad, C.A. Jeffrey, C. Berger, "Highly ordered graphene for two dimensional electronics", *Applied Physics Letters*, **89** (2006) 143106.

[**77**] L.G.D. Arco, Y. Zhang, A. Kumar, C. Zhou, "Synthesis, transfer, and devices of single- and few-layer graphene by chemical vapor deposition", *IEEE Transactions on Nanotechnology*, **8** (2009) 135-138.

[**78**] K. Wang, G. Tai, K.H. Wong, S.P. Lau, W. Guo, "Ni induced few-layer graphene growth at low temperature by pulsed laser deposition", *AIP Advances*, **1** (2011) 022141.

[**79**] M. Qian, Y.S. Zhou, Y. Gao, J.B. Park, T. Feng, S.M. Huang, Z. Sun, L. Jiang, Y.F. Lu, "Formation of graphene sheets through laser exfoliation of highly ordered pyrolytic graphite", *Applied Physics Letters*, **98** (2011) 173108.

[**80**] A.T.T. Koh, Y.M. Foong, D.H.C. Chua, "Cooling rate and energy dependence of pulsed laser fabricated graphene on nickel at reduced temperature", *Applied Physics Letters*, **97** (2010) 114102.

[**81**] S. Stankovich, D.A. Dikin, R.D. Piner, K.A. Kohlhaas, A. Kleinhammes, Y. Jia, Y. Wu, S.T. Nguyen, R.S. Ruoff, "Synthesis of graphene-based nanosheets via chemical reduction of exfoliated graphite oxide", *Carbon*, **45** (2007) 1558-1565.

[**82**] T.N. Lambert, C.C. Luhrs, C.A. Chavez, S. Wakeland, M.T. Brumbach, T.M. Alam, "Graphite oxide as a precursor for the synthesis of disordered graphenes using the aerosol-through-plasma method", *Carbon*, **48** (2010) 4081-4089.

[**83**] O. Akhavan, "The effect of heat treatment on formation of graphene thin films from graphene oxide nanosheets", *Carbon*, **48** (2010) 509-519.

[**84**] W. Chen, L. Yan, P.R. Bangal, "Preparation of graphene by the rapid and mild thermal reduction of graphene oxide induced by microwaves", *Carbon*, **48** (2010) 1146-1152.

[**85**] E. Tatarova, J. Henriques, C.C. Luhrs, A. Dias, J. Phillips, M.V. Abrashev, C.M. Ferreira, "Microwave plasma based single step method for free standing graphene synthesis at atmospheric conditions", *Applied Physics Letters*, **103** (2013) 134101.

[**86**] B. Shen, J. Ding, X. Yan, W. Feng, J. Li, Q. Xue, "Influence of different buffer gases on synthesis of few-layered graphene by arc discharge method", *Applied Surface Science*, **258** (2012) 4523-4531.

[**87**] A. Reina, X. Jia, J. Ho, D. Nezich, H. Son, V. Bulovic, M.S. Dresselhaus, J. Kong, "Large area, few-layer graphene films on arbitrary substrates by chemical vapor deposition", *Nano Letters*, **9** (2009) 30-35.

[**88**] H. Zhang, P.X. Feng, "Fabrication and characterization of few-layer graphene", *Carbon*, **48** (2010) 359-364.

[**89**] A.T.T. Mostako, C.V.S. Rao, A. Khare, "Mirrorlike pulsed laser deposited tungsten thin film", *Review of Scientific Instruments*, **82** (2011) 013101.

[**90**] R.D. Vispute, S. Choopun, R. Enck, A. Patel, V. Talyansky, R.P. Sharma, T. Venkatesan, W.L. Sarney, L. Salamancariba, S.N. Andronescu, A.A. Iliadis, K.A. Jones, "Pulsed laser deposition and processing of wide band gap semiconductors and related materials", *Journal of Electronic Materials*, **28** (1999) 275-286.

[**91**] P.R. Willmott, J.R. Huber, "Pulsed laser vaporization and deposition", *Reviews of Modern Physics*, **72** (2000) 315-328.

[**92**] M.N.R. Ashfold, F. Claeyssens, G.M. Fuge, S.J. Henley, "Pulsed laser ablation and deposition of thin films", *Chemical Society Reviews*, **33** (2004) 23-31.

[**93**] H.M. Christen, G. Eres, "Recent advances in pulsed-laser deposition of complex oxides", *Journal of Physics: Condensed Matter*, **20** (2008) 264005.

[**94**] D.B. Chrisey, G.K. Hubler, "Pulsed Laser Deposition of Thin Films", *Wiley-Interscience*, New York, 1994.

[**95**] R.W. Eason, "Pulsed Laser Deposition of Thin Films Applications", *John Wiley & Sons*, New York, 2007.

[**96**] D.H. Lowndes, D.B. Geohegan, A.A. Puretzky, D.P. Norton, C.M. Rouleau, "Synthesis of novel thin-film materials by pulsed laser deposition", *Science*, **273** (1996) 898-903.

[**97**] J. Schou, "Physical aspects of the pulsed laser deposition technique: The stoichiometric transfer of material from target to film", *Applied Surface Science*, **255** (2009) 5191-5198.

[**98**] G.Z. Liu, Q.Y. Lei, X.X. Xi, "Stoichiometry of $SrTiO_3$ films grown by pulsed laser deposition", *Applied Physics Letters*, **100** (2012) 202902.

[**99**] T. Ohnishi, M. Lippmaa, T. Yamamoto, S. Meguro, H. Koinuma, "Improved stoichiometry and misfit control in perovskite thin film formation at a critical fluence by pulsed laser deposition", *Applied Physics Letters*, **87** (2005) 241919.

[**100**] R. Groenen, J. Smit, K. Orsel, A. Vailionis, B. Bastiaens, M. Huijben, K. Boller, G. Rijnders, G. Koster, "Research Update: Stoichiometry controlled oxide thin film growth by pulsed laser deposition", *APL Materials*, **3** (2015) 070701.

[**101**] R.K. Singh, J. Narayan, "Pulsed-laser evaporation technique for deposition of thin films: Physics and theoretical model", *Physical Review B*, **41** (1990) 8843-8859.

[**102**] T. Yoshitake, T. Nishiyama, H. Aoki, K. Suizu, K. Takahashi, K. Nagayama, "The effects of substrate temperature and laser wavelength on the formation of carbon thin films by pulsed laser deposition", *Diamond and Related Materials*, **8** (1999) 463-467.

[**103**] T.V. Kononenko, V.V. Kononenko, S.M. Pimenov, E.V. Zavedeev, V.I. Konov, V. Romano, G. Dumitru, "Effects of pulse duration in laser processing of diamond-like carbon films", *Diamond and Related Materials*, **14** (2005) 1368-1376.

[**104**] A. Sikora, F. Garrelie, C. Donnet, A.S. Loir, J. Fontaine, J.C. Sanchez-Lopez, T.C. Rojas, "Structure of diamondlike carbon films deposited by femtosecond and nanosecond pulsed laser ablation", *Journal of Applied Physics*, **108** (2010) 113516.

[**105**] K.J. Koivusaari, J. Levoska, S. Leppävuori, "Pulsed-laser deposition of diamond-like carbon: Relations between laser fluence, velocity of carbon ions, and bonding in the films", *Journal of Applied Physics*, **85** (1999) 2915-2920.

[**106**] H.C. Ong, R.P.H. Chang, "Effect of laser intensity on the properties of carbon plasmas and deposited films", *Physical Review B*, **55** (1997) 13213-13220.

[**107**] T. Yoshitake, T. Nishiyama, K. Nagayama, "The role of hydrogen and oxygen gas in the growth of carbon thin films by pulsed laser deposition", *Diamond and Related Materials*, **9** (2000) 689-692.

[**108**] Y. Lifshitz, "Hydrogen-free amorphous carbon films: correlation between growth conditions and properties", *Diamond and Related Materials*, **5** (1996) 388-400.

[**109**] A.T.T. Mostako, A. Khare, "Large area deposition of Rh single and Rh/W/Cu multilayer thin films on stainless steel substrate by pulsed laser deposition technique", *Review of Scientific Instruments*, **85** (2014) 046101.

[**110**] G. Shukla, A. Khare, "Effect of substrate annealing on the quality of pulsed laser deposited $Zn_{1-x}Mg_xO$ thin films", *Applied Surface Science*, **255** (2009) 7017-7020.

[**111**] S. Kumari, A. Khare, "Optical and structural characterization of pulsed laser deposited ruby thin films for temperature sensing application", *Applied Surface Science*, **265** (2013) 180-186.

[**112**] J.A. Greer, M.D. Tabat, "Large-area pulsed laser deposition: Techniques and applications", *Journal of Vacuum Science & Technology A*, **13** (1995) 1175-1181.

[**113**] H.M. Smith, A.F. Turner, "Vacuum deposited thin films using a ruby laser", *Applied Optics*, **4** (1965) 147-148.

[**114**] F. Xiong, Y.Y. Wang, V. Leppert, R.P.H. Chang, "Pulsed laser deposition of amorphous diamond-like carbon films with ArF (193 nm) excimer laser", *Journal of Materials Research*, **8** (1993) 2265-2272.

[**115**] J.P. Singh, S.N. Thakur, "Laser-Induced Breakdown Spectroscopy", *Elsevier, UK*, 2007.

[**116**] S.J. Henley, J.D. Carey, S.R.P. Silva, G.M. Fuge, M.N.R. Ashfold, D. Anglos, "Dynamics of confined plumes during short and ultrashort pulsed laser ablation of graphite", *Physical Review B*, **72** (2005) 205413.

[**117**] Z. Chen, D. Bleiner, A. Bogaerts, "Effect of ambient pressure on laser ablation and plume expansion dynamics: A numerical simulation", *Journal of Applied Physics*, **99** (2006) 063304.

[**118**] S.S. Harilal, "Expansion dynamics of laser ablated carbon plasma plume in helium ambient", *Applied Surface Science*, **172** (2001) 103-109.

[**119**] J. Haverkamp, R.M. Mayo, M.A. Bourham, J. Narayan, C. Jin, G. Duscher, "Plasma plume characteristics and properties of pulsed laser deposited diamond-like carbon films", *Journal of Applied Physics*, **93** (2003) 3627-3634.

[**120**] Y. Tasaka, H. Kuroda, M. Tanaka, S. Usami, "Velocity analysis of ablated particles in pulsed laser deposition of NiO film", *Thin Solid Films*, **281-282** (1996) 441-444.

[**121**] N. Smijesh, K.H. Rao, R. Philip, "Influence of pulse width on the laser ablation of zinc in nitrogen ambient", *Applied Physics A*, **122** (2016) 460.

[**122**] S. Kumari, A. Kushwaha, A. Khare, "Spatial distribution of electron temperature and ion density in laser induced ruby (Al_2O_3:Cr^{3+}) plasma using Langmuir probe", *Journal of Instrumentation*, **7** (2012) C05017.

[**123**] K. Ebihara, T. Nakamiya, T. Ohshima, T. Ikegami, S.-i. Aoqui, "Influence of ambient gas on diamond-like carbon films prepared by KrF pulsed laser deposition", *Diamond and Related Materials*, **10** (2001) 900-904.

[**124**] T. Kerdja, S. Abdelli, D. Ghobrini, S. Malek, "Dynamics of laser-produced carbon plasma in an inert atmosphere", *Journal of Applied Physics*, **80** (1996) 5365-5371.

[**125**] S. Metev, K. Meteva, "Nucleation and growth of laser-plasma deposited thin films", *Applied Surface Science*, **43** (1989) 402-408.

[**126**] A.C. Ferrari, J. Robertson, "Interpretation of Raman spectra of disordered and amorphous carbon", *Physical Review B*, **61** (2000) 14095-14107.

[**127**] P.K. Chu, L. Li, "Characterization of amorphous and nanocrystalline carbon films", *Materials Chemistry and Physics*, **96** (2006) 253-277.

[**128**] A.C. Ferrari, "Determination of bonding in diamond-like carbon by Raman spectroscopy", *Diamond and Related Materials*, **11** (2002) 1053-1061.

[**129**] F. Tuinstra, J.L. Koenig, "Raman spectrum of graphite", *The Journal of Chemical Physics*, **53** (1970) 1126-1130.

[**130**] D.S. Knight, W.B. White, "Characterization of diamond films by Raman spectroscopy", *Journal of Materials Research*, **4** (1989) 385-393.

[**131**] S. Neuville, "Quantum electronic mechanisms of atomic rearrangements during growth of hard carbon films", *Surface and Coatings Technology*, **206** (2011) 703-726.

[**132**] S.R. Sails, D.J. Gardiner, M. Bowden, J. Savage, D. Rodway, "Monitoring the quality of diamond films using Raman spectra excited at 514.5 nm and 633 nm", *Diamond and Related Materials*, **5** (1996) 589-591.

[**133**] R.E. Shroder, R.J. Nemanich, J.T. Glass, "Analysis of the composite structures in diamond thin films by Raman spectroscopy", *Physical Review B*, **41** (1990) 3738-3745.

[**134**] R.J. Nemanich, S.A. Solin, "First- and second-order Raman scattering from finite-size crystals of graphite", *Physical Review B*, **20** (1979) 392-401.

[**135**] I. Kumar, A. Khare, "Multi- and few-layer graphene on insulating substrate via pulsed laser deposition technique", *Applied Surface Science*, **317** (2014) 1004-1009.

[**136**] T. Shimada, T. Sugai, C. Fantini, M. Souza, L.G. Cançado, A. Jorio, M.A. Pimenta, R. Saito, A. Grüneis, G. Dresselhaus, M.S. Dresselhaus, Y. Ohno, T. Mizutani, H. Shinohara, "Origin of the 2450 cm^{-1} Raman bands in HOPG, single-wall and double-wall carbon nanotubes", *Carbon*, **43** (2005) 1049-1054.

[**137**] A.C. Ferrari, J. Robertson, "Raman spectroscopy of amorphous, nanostructured, diamond–like carbon, and nanodiamond", *Philosophical Transactions of the Royal Society of London A*, **362** (2004) 2477-2512.

[**138**] I. Kumar, A. Khare, "Optical nonlinearity in nanostructured carbon thin films fabricated by pulsed laser deposition technique", *Thin Solid Films*, **611** (2016) 56-61.

[**139**] D. Beeman, J. Silverman, R. Lynds, M.R. Anderson, "Modeling studies of amorphous carbon", *Physical Review B*, **30** (1984) 870-875.

[**140**] W.G. Cui, Q.B. Lai, L. Zhang, F.M. Wang, "Quantitative measurements of sp^3 content in DLC films with Raman spectroscopy", *Surface and Coatings Technology*, **205** (2010) 1995-1999.

[**141**] B. Ryan, C. Luiz Gustavo, N. Lukas, "Raman characterization of defects and dopants in graphene", *Journal of Physics: Condensed Matter*, **27** (2015) 083002.

[**142**] R. Swanepoel, "Determination of the thickness and optical constants of amorphous silicon", *Journal of Physics E: Scientific Instruments*, **16** (1983) 1214-1222.

[**143**] J. Zhu, J. Han, X. Han, S. Meng, A. Liu, X. He, "Optical properties of amorphous diamond films evaluated by non-destructive spectroscopic ellipsometry", *Optical Materials*, **28** (2006) 473-479.

[**144**] A.A. Khan, D. Mathine, J.A. Woollam, Y. Chung, "Optical properties of "diamondlike" carbon films: An ellipsometric study", *Physical Review B*, **28** (1983) 7229-7235.

[**145**] H. Fujiwara, "Spectroscopic ellipsometry: Principles and Applications", *John Wiley and Sons Ltd, England*, 2007.

[**146**] A. Canillas, M.C. Polo, J.L. Andújar, J. Sancho, S. Bosch, J. Robertson, W.I. Milne, "Spectroscopic ellipsometric study of tetrahedral amorphous carbon films: optical properties and modelling", *Diamond and Related Materials*, **10** (2001) 1132-1136.

[**147**] N. Laidani, R. Bartali, G. Gottardi, M. Anderle, P. Cheyssac, "Optical absorption parameters of amorphous carbon films from Forouhi–Bloomer and Tauc–Lorentz models: a comparative study", *Journal of Physics: Condensed Matter*, **20** (2008) 015216.

[**148**] W.A. McGahan, T. Makovicka, J. Hale, J.A. Woollam, "Modified Forouhi and Bloomer dispersion model for the optical constants of amorphous hydrogenated carbon thin films", *Thin Solid Films*, **253** (1994) 57-61.

[**149**] Y. Liu, G. Xu, C. Song, W. Weng, P. Du, G. Han, "Modification on Forouhi and Bloomer model for the optical properties of amorphous silicon thin films", *Thin Solid Films*, **515** (2007) 3910-3913.

[**150**] A.C. Ferrari, S.E. Rodil, J. Robertson, "Interpretation of infrared and Raman spectra of amorphous carbon nitrides", *Physical Review B*, **67** (2003) 155306.

[**151**] M. Bonelli, A.C. Ferrari, A. Fioravanti, A. Li Bassi, A. Miotello, P.M. Ossi, "Structure and mechanical properties of low stress tetrahedral amorphous carbon films prepared by pulsed laser deposition", *The European Physical Journal B - Condensed Matter and Complex Systems*, **25** (2002) 269-280.

[**152**] S.E. Rodil, "Infrared spectra of amorphous carbon based materials", *Diamond and Related Materials*, **14** (2005) 1262-1269.

[**153**] S.E. Rodil, A.C. Ferrari, J. Robertson, W.I. Milne, "Raman and infrared modes of hydrogenated amorphous carbon nitride", *Journal of Applied Physics*, **89** (2001) 5425-5430.

[**154**] A. Grill, V. Patel, "Characterization of diamondlike carbon by infrared spectroscopy?", *Applied Physics Letters*, **60** (1992) 2089-2091.

[**155**] Ö.D. Coşkun, T. Zerrin, "Optical, structural and bonding properties of diamond-like amorphous carbon films deposited by DC magnetron sputtering", *Diamond and Related Materials*, **56** (2015) 29-35.

[**156**] H. Pang, X. Wang, G. Zhang, H. Chen, G. Lv, S. Yang, "Characterization of diamond-like carbon films by SEM, XRD and Raman spectroscopy", *Applied Surface Science*, **256** (2010) 6403-6407.

[**157**] R.K. Roy, B. Deb, B. Bhattacharjee, A.K. Pal, "Synthesis of diamond-like carbon film by novel electrodeposition route", *Thin Solid Films*, **422** (2002) 92-97.

[**158**] L.W. Tutt, T.F. Boggess, "A review of optical limiting mechanisms and devices using organics, fullerenes, semiconductors and other materials", *Progress in Quantum Electronics*, **17** (1993) 299-338.

[**159**] J. Wang, Y. Chen, W.J. Blau, "Carbon nanotubes and nanotube composites for nonlinear optical devices", *Journal of Materials Chemistry*, **19** (2009) 7425-7443.

[**160**] Z. Wang, S.-E. Zhu, Y. Chen, M. Wu, C. Zhao, H. Zhang, G.C.A.M. Janssen, S. Wen, "Multilayer graphene for Q-switched mode-locking operation in an erbium-doped fiber laser", *Optics Communications*, **300** (2013) 17-21.

[**161**] S.R. Friberg, P.W. Smith, "Nonlinear optical glasses for ultrafast optical switches", *IEEE Journal of Quantum Electronics*, **23** (1987) 2089-2094.

[**162**] J. Seo, S. Ma, Q. Yang, L. Creekmore, R. Battle, M. Tabibi, H. Brown, A. Jackson, T. Skyles, B. Tabibi, S. Jung, M. Namkung, "Third-order optical nonlinearities of singlewall carbon nanotubes for nonlinear transmission limiting application", *Journal of Physics: Conference Series*, **38** (2006) 37-40.

[**163**] K.C. Jena, P.B. Bisht, M.M. Shaijumon, S. Ramaprabhu, "Study of optical nonlinearity of functionalized multi-wall carbon nanotubes by using degenerate four wave mixing and *Z*-scan techniques", *Optics Communications*, **273** (2007) 153-158.

[**164**] H. Zhang, S. Virally, Q. Bao, L. Kian Ping, S. Massar, N. Godbout, P. Kockaert, "*Z*-scan measurement of the nonlinear refractive index of graphene", *Optics Letters*, **37** (2012) 1856-1858.

[**165**] X. Zhao, Z.-B. Liu, W.-B. Yan, Y. Wu, X.-L. Zhang, Y. Chen, J.-G. Tian, "Ultrafast carrier dynamics and saturable absorption of solution-processable few-layered graphene oxide", *Applied Physics Letters*, **98** (2011) 121905.

[**166**] D. Vincent, S. Petit, S.L. Chin, "Optical limiting studies in a carbon-black suspension for subnanosecond and subpicosecond laser pulses", *Applied Optics*, **41** (2002) 2944-2946.

[**167**] E. Koudoumas, O. Kokkinaki, M. Konstantaki, S. Couris, S. Korovin, P. Detkov, V. Kuznetsov, S. Pimenov, V. Pustovoi, "Onion-like carbon and diamond nanoparticles for optical limiting", *Chemical Physics Letters*, **357** (2002) 336-340.

[**168**] M. Sheik-Bahae, R.J. DeSalvo, A.A. Said, D.J. Hagan, M.J. Soileau, E.W. Van Stryland, "Optical nonlinearities in diamond", *SPIE*, **2428** (1995) 605-609.

[**169**] E. Fazio, F. Neri, S. Patanè, L. D'Urso, G. Compagnini, "Optical limiting effects in linear carbon chains", *Carbon*, **49** (2011) 306-310.

[**170**] T. Kaplas, L. Karvonen, J. Rönn, M.R. Saleem, S. Kujala, S. Honkanen, Y. Svirko, "Nonlinear refraction in semitransparent pyrolytic carbon films", *Optical Materials Express*, **2** (2012) 1822-1827.

[**171**] T. He, W. Wei, L. Ma, R. Chen, S. Wu, H. Zhang, Y. Yang, J. Ma, L. Huang, G.G. Gurzadyan, H. Sun, "Mechanism studies on the superior optical limiting observed in graphene oxide covalently functionalized with upconversion $NaYF_4:Yb^{3+}/Er^{3+}$ nanoparticles", *Small*, **8** (2012) 2163-2168.

[**172**] R.W. Boyd, "Nonlinear Optics", *Academic press, London*, 2008.

[**173**] L. Vivien, P. Lançon, D. Riehl, F. Hache, E. Anglaret, "Carbon nanotubes for optical limiting", *Carbon*, **40** (2002) 1789-1797.

[**174**] L. Vivien, E. Anglaret, D. Riehl, F. Bacou, C. Journet, C. Goze, M. Andrieux, M. Brunet, F. Lafonta, P. Bernier, F. Hache, "Single-wall carbon nanotubes for optical limiting", *Chemical Physics Letters*, **307** (1999) 317-319.

[**175**] R. Signorini, M. Meneghetti, R. Bozio, M. Maggini, G. Scorrano, M. Prato, G. Brusatin, P. Innocenzi, M. Guglielmi, "Optical limiting and non linear optical properties of fullerene derivatives embedded in hybrid sol–gel glasses", *Carbon*, **38** (2000) 1653-1662.

[**176**] Z. Sun, T. Hasan, F. Torrisi, D. Popa, G. Privitera, F. Wang, F. Bonaccorso, D.M. Basko, A.C. Ferrari, "Graphene mode-locked ultrafast laser", *ACS Nano*, **4** (2010) 803-810.

[**177**] X. Liu, D. Han, Z. Sun, C. Zeng, H. Lu, D. Mao, Y. Cui, F. Wang, "Versatile multi-wavelength ultrafast fiber laser mode-locked by carbon nanotubes", *Scientific Reports*, **3** (2013) 2718.

[**178**] G. Della Valle, R. Osellame, G. Galzerano, N. Chiodo, G. Cerullo, P. Laporta, O. Svelto, U. Morgner, A.G. Rozhin, V. Scardaci, A.C. Ferrari, "Passive mode locking by carbon nanotubes in a femtosecond laser written waveguide laser", *Applied Physics Letters*, **89** (2006) 231115.

[**179**] M.J. Moran, S. Chiao-Yao, R.L. Carman, "Interferometric measurements of the nonlinear refractive-index coefficient relative to CS_2 in laser-system-related materials", *IEEE Journal of Quantum Electronics*, **11** (1975) 259-263.

[**180**] A. Owyoung, "Ellipse rotation studies in laser host materials", *IEEE Journal of Quantum Electronics*, **9** (1973) 1064-1069.

[**181**] M. Sheik-Bahae, A.A. Said, T.H. Wei, D.J. Hagan, E.W. Van Stryland, "Sensitive measurement of optical nonlinearities using a single beam", *IEEE Journal of Quantum Electronics*, **26** (1990) 760-769.

[**182**] W.E. Williams, M.J. Soileau, E.W. Van Stryland, "Optical switching and n_2 measurements in CS_2", *Optics Communications*, **50** (1984) 256-260.

भारतीय प्रौद्योगिकी संस्थान गुवाहाटी
Indian Institute of Technology Guwahati

Chapter 2

Experimental details

Pulsed laser deposition (PLD) technique is widely used for the growth of large variety of thin films [**1-11**]. The properties of PLD thin films are strongly influenced by the kinetics of the laser produced plasma species which in turn can be controlled by a number of deposition parameters [**12-18**]. In the present thesis, PLD technique was used to deposit the DLC and graphitic thin films over a large range of deposition parameters; substrate temperature, laser fluence and helium gas pressure, to identify the optimum condition for sp^3 and sp^2 dominated films. The effect of substrate temperature on the deposition of graphene layers in presence of oxygen gas as the background is also studied. PLD films were characterized by Raman spectrometer, Spectroscopic ellipsometer, Fourier transform infrared spectrophotometer, Atomic force microscope and Stylus profilometer. Graphene layers were also subjected to Transmission electron microscope and Field emission scanning electron microscope. The nonlinear absorption (NLA) and nonlinear refractive index (NLR) coefficients were measured by in-house developed modified *Z*-scan setup.

In this chapter, the experimental details of PLD setup, modified *Z*-scan setup and all the other characterization tools employed for PLD films are presented.

2.1 Pulsed laser deposition (PLD) setup

The schematic of PLD setup and its photograph used for deposition of DLC films, few- and multi-layer graphene and graphitic thin films is shown in *Figure 2.1 and*

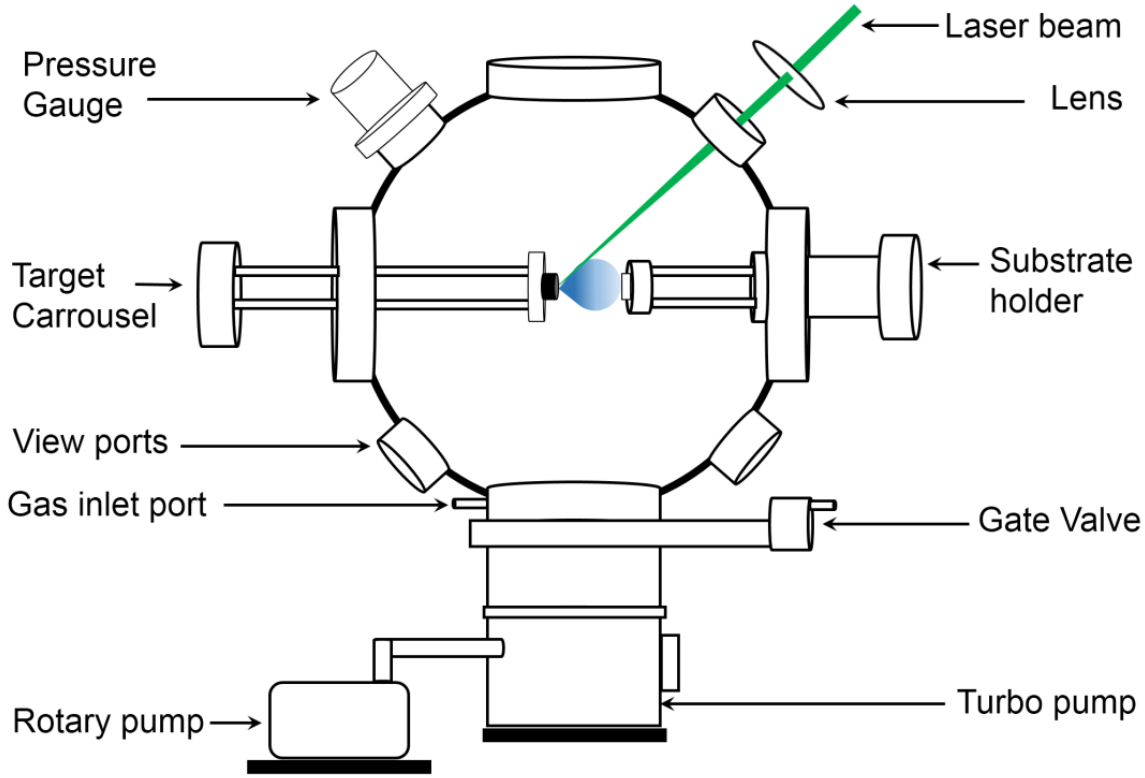

***Figure 2.1**: Schematic of PLD setup.*

2.2, respectively. It consists of a 12" diameter ultra-high vacuum compatible multiport stainless steel chamber. The graphite target was mounted on a motorized target carrousel and was inserted inside through one of the 150 CF port of the vacuum chamber. The substrate (glass and silicon) was mounted on a substrate holder assembly having provision of resistive heater to control the substrate temperature in a programmable manner. The substrate holder assembly was mounted on another 150 CF port of the ablation chamber opposite to the target carrousel. The target to substrate separation was maintained around ~3 cm. The PLD films of carbon were deposited on glass and silicon substrates. Prior to deposition, the vacuum chamber was evacuated to a base pressure ~10^{-6} mbar using turbo molecular pump (*Pfeiffer, Hi Pace 300 C*) connected to the bottom 100 CF port of the vacuum chamber, as shown in *Figure 2.1*. The turbo molecular pump was backed by a rotary pump (*Pfeiffer, DUO 10 MC*). The pressure inside the ablation chamber was monitored using a compact cold cathode gauge (*Pfeiffer,*

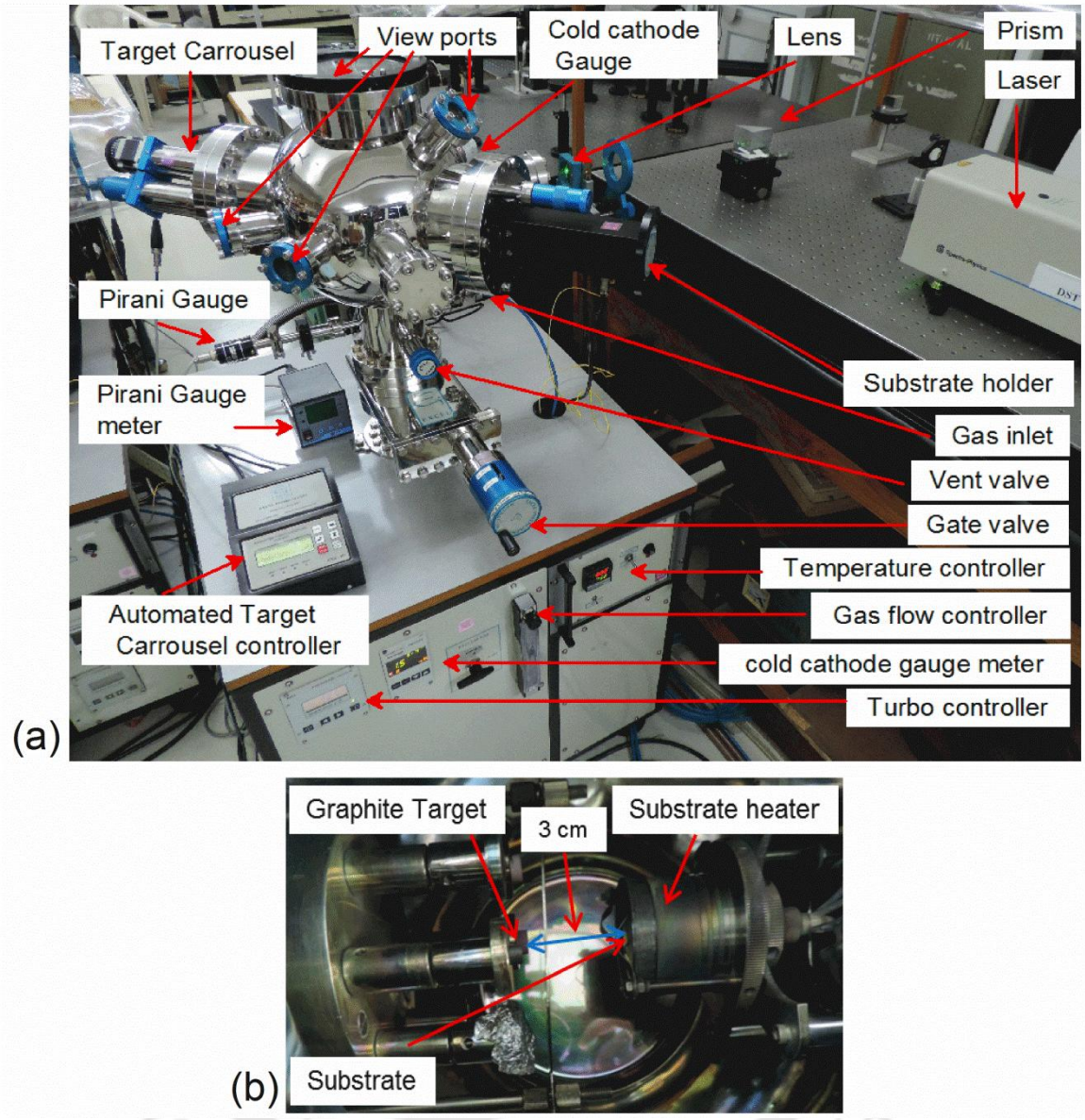

Figure 2.2: *Photograph of* ***(a)*** *PLD setup and* ***(b)*** *target-substrate configuration.*

IKR 251) for low pressure regime (10^{-2} mbar – 10^{-7} mbar) and pirani gauge (*Pfeiffer, PCR 280* and *Hind HiVac, HPS-2*) for high pressure regime (10^{3} mbar - 10^{-3} mbar). The second harmonic of a Q-switched Nd:YAG laser (*Quanta-System, HYL-101*; 532 nm, 8 ns, 10 Hz) was used to fabricate the DLC thin films and graphene layers whereas the third harmonic of a Q-switched Nd:YAG laser (*Quanta-Ray, INDI-HG;* 355 nm, 8 ns, 10Hz) was used for the deposition of graphitic thin films. The laser beam was focused onto the graphite target by a convex lens of focal length of 35 cm. The focusing of the laser beam furnishes the laser induced plasma of carbon from graphite target which

expands in the presence of background gas and finally deposited onto the substrate placed parallel to the target. The DLC and graphitic thin films were deposited in vacuum as well as in the presence of helium gas. Few- and multi-layer graphene were deposited in the oxygen gas ambient at a pressure of 0.1 mbar. The ambient gases were purged into the deposition chamber through a 16 CF port via gas flow controller, shown in *Figure 2.2.* The flow rate was maintained in the range of 20-30 standard cubic centimetres per minute (sccm).

2.2 Characterization of PLD thin films

All the samples fabricated via PLD in the present work were subjected to various characterizations as briefed below:

2.2.1 Atomic force microscopy (AFM)

The atomic force microscope (*Aligent, 5500 series*) was used in non-contact mode using silicon cantilever to image the surface morphology of PLD films. The Root mean square (RMS) Surface roughness and average grain sizes of PLD films were estimated using software "*WSxM 5.0 Develop 7.0*" [**19**].

2.2.2 Field emission scanning electron microscopy (FESEM)

The surface morphology of the graphene samples were also captured by FESEM (*ZEISS sigma*) which was operated at an accelerating voltage of 3 to 5 keV. The films were coated with very thin gold layer in a separate vacuum chamber prior to loading them inside the vacuum column of FESEM to avoid the charging effect during measurement.

2.2.3 Transmission electron microscopy (TEM)

To capture the TEM images of graphene, it was deposited onto the uncoated Cu mesh grid. The measurements were performed with TEM (*Jeol, JEM 2100*) using electron source at accelerating voltage of 200 keV. The TEM images and SAED pattern were analysed for inter-spacing distance using software "*Gatan digital micrograph*" of TEM instrument.

2.2.4 Raman spectroscopy

To unveil the proportion of sp^3 and sp^2 bonding and to assess the disorder, Raman spectra of PLD films were recorded by the micro-Laser Raman spectrometer (*Horiba Jobin Yvon, LabRam HR800*) using a holographic grating of 1800 groves/mm. He-Ne laser (633 nm) and Ar-ion laser (488 nm and 514 nm) were used as an excitation source. The laser beam was focused on the sample using an objective lens, 100X, to a spot size of ~1 μm diameter on the film surface.

2.2.5 Fourier transform infrared spectroscopy (FTIR)

In the present thesis, a single beam FTIR spectrometer (*Perkin Elmer BX*) was used to record the IR transmission spectra of DLC films to assess the hydrogen content in it. For FTIR measurement, DLC films were deposited onto undoped silicon (100) wafer. The spectrometer was operated with a resolution of 4 cm^{-1} and the spectra were averaged over twenty scans for each sample.

2.2.6 Spectroscopic ellipsometry

A rotatory polarizer ellipsometer (*Semilab GES5-E*) was used to measure the linear refractive index, absorption coefficient, thickness and optical band gap of the PLD films. As the DLC films are amorphous in nature, the spectra were fitted to modified

Fourohi-Bloomer (mFB) model. To fit the spectra, the structure of the sample was modelled to three interfaces: (1) air/film, (2) film/substrate and (3) substrate/air, as shown in *Figure 2.3*. Transmission spectra were also recorded using ellipsometer to estimate the optical band gap of DLC films.

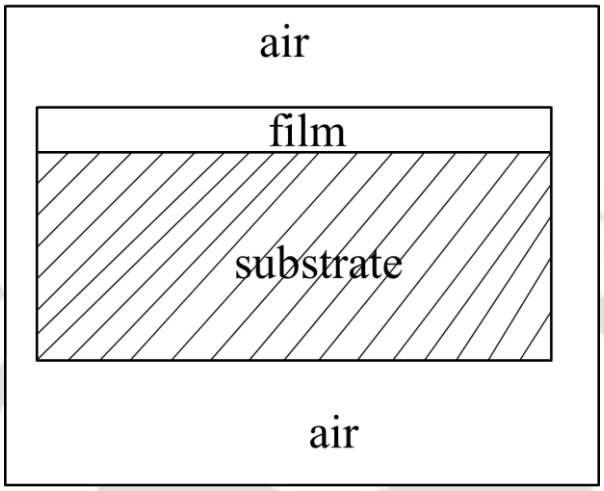

***Figure 2.3**: Schematic of structure adopted for dispersion model.*

2.2.7 Stylus profilometer

Thickness of PLD films was also measured directly using profilometer (*Veeco DekTak 150*). In this instrument, the stylus tip, made up of silicon carbide, is pulled in contact mode along the masked-unmasked interface of the film surface at constant velocity. At the interface, the displacement of tip experiences a step which is the measure of the film thickness. The vertical resolution of the profilometer is in Å and that of the lateral resolution is 1 μm. To prevent destruction of the film surface, the load on the sample was kept 3 mN. The thickness of all samples presented in thesis was the average value of the measurement over the five different locations.

2.3 Modified *Z*-scan setup

To study the nonlinear optical (NLO) properties of pulsed laser deposited films, *Z*-scan technique was employed by modifying the conventional setup [**20**]. *Figure 2.4*

and 2.5 show the schematic of in-house assembled modified *Z*-scan setup and its photograph, respectively.

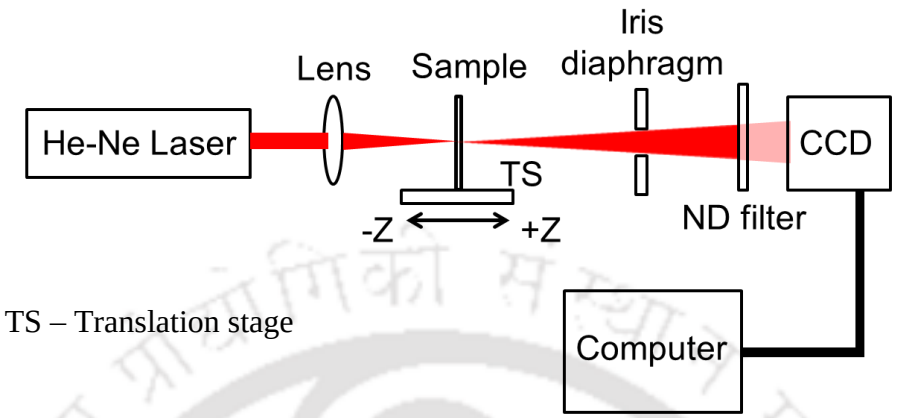

Figure 2.4: *Schematic of modified Z-scan setup.*

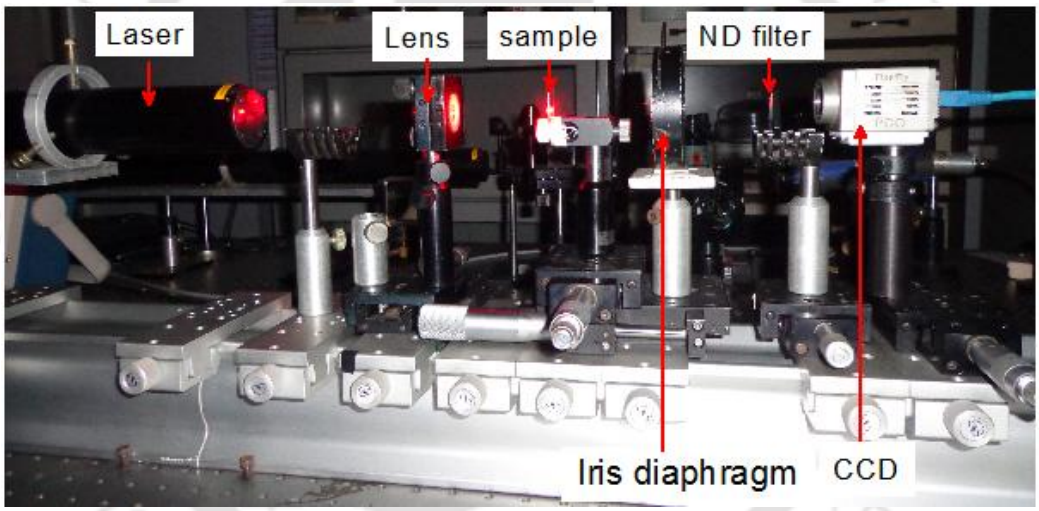

Figure 2.5: *Photograph of modified Z-scan setup.*

A He-Ne laser (*Melles Griot, 05-LHP-927*, 632.8 nm) was focused by a convex lens of the focal length of 5 cm on the sample. The transmitted beam from the sample was imaged on a CCD detector (*PCO, PixelFly*), kept at a distance of ~25 cm from the focusing lens. A neutral density (ND) filter was placed in front of CCD to avoid its saturation. An iris diaphragm of aperture size ~6 mm was placed before the ND filter to suppress the scattered light entering into the CCD. The images of the transmitted beam were recorded by scanning the sample 20 mm on either side of the focal position of the lens. For recording the open aperture *Z*-scan curve, the transmitted intensity through the

thin film was obtained by integrating the gray values of the recorded images. The same images were used to obtain the data for CA *Z*-scan by applying a suitable synthetic aperture onto the image using the Matlab program. The measurement details on NLA and NLR coefficients using this modified *Z*-scan setup is detailed in *Chapter 6*.

Conclusion

In this chapter, the pulsed laser deposition setup to fabricate DLC and graphitic thin films as well as graphene layers and the modified *Z*-scan setup developed, to study the NLO properties of PLD films are discussed. The various characterization instruments employed to study the structural and optical properties of PLD films are also presented briefly.

Bibliography

[**1**] D.L. Pappas, K.L. Saenger, J. Bruley, W. Krakow, J.J. Cuomo, T. Gu, R.W. Collins, "Pulsed laser deposition of diamond-like carbon films", *Journal of Applied Physics*, **71** (1992) 5675-5684.

[**2**] R.W. Eason, "Pulsed Laser Deposition of Thin Films Applications", *John Wiley & Sons*, New York, 2007.

[**3**] P.M. Ossi, C.E. Bottani, A. Miotello, "Pulsed laser deposition of nano-glassy carbon films", *Applied Surface Science*, **248** (2005) 334-339.

[**4**] K. Wang, G. Tai, K.H. Wong, S.P. Lau, W. Guo, "Ni induced few-layer graphene growth at low temperature by pulsed laser deposition", *AIP Advances*, **1** (2011) 022141.

[**5**] I. Kumar, A. Khare, "Multi- and few-layer graphene on insulating substrate via pulsed laser deposition technique", *Applied Surface Science*, **317** (2014) 1004-1009.

[**6**] S. Kumari, A. Khare, "Langmuir probe studies of laser ablated ruby plasma and correlation with pulsed laser deposited ruby thin film properties", *Laser and Particle Beams*, **32** (2014) 359-367.

[**7**] G. Shukla, A. Khare, "Spectroscopic studies of laser ablated ZnO plasma and correlation with pulsed laser deposited ZnO thin film properties", *Laser and Particle Beams*, **28** (2010) 149-155.

[**8**] S. Kumari, A. Khare, "Pulsed laser deposited barium titanate thin film for tunable optical delay application", *Applied Surface Science*, **347** (2015) 619-623.

[**9**] A.T.T. Mostako, C.V.S. Rao, A. Khare, "Mirrorlike pulsed laser deposited tungsten thin film", *Review of Scientific Instruments*, **82** (2011) 013101.

[**10**] A.T.T. Mostako, A. Khare, "Molybdenum thin films via pulsed laser deposition technique for first mirror application", *Laser and Particle Beams*, **30** (2012) 559-567.

[**11**] A.T.T. Mostako, A. Khare, "Large area deposition of Rh single and Rh/W/Cu multilayer thin films on stainless steel substrate by pulsed laser deposition technique", *Review of Scientific Instruments*, **85** (2014) 046101.

[**12**] R.K. Singh, J. Narayan, "Pulsed-laser evaporation technique for deposition of thin films: Physics and theoretical model", *Physical Review B*, **41** (1990) 8843-8859.

[**13**] T. Yoshitake, T. Nishiyama, H. Aoki, K. Suizu, K. Takahashi, K. Nagayama, "The effects of substrate temperature and laser wavelength on the formation of carbon thin films by pulsed laser deposition", *Diamond and Related Materials*, **8** (1999) 463-467.

[**14**] K.J. Koivusaari, J. Levoska, S. Leppävuori, "Pulsed-laser deposition of diamond-like carbon: Relations between laser fluence, velocity of carbon ions, and bonding in the films", *Journal of Applied Physics*, **85** (1999) 2915-2920.

[**15**] T. Yoshitake, T. Nishiyama, K. Nagayama, "The role of hydrogen and oxygen gas in the growth of carbon thin films by pulsed laser deposition", *Diamond and Related Materials*, **9** (2000) 689-692.

[**16**] H.C. Ong, R.P.H. Chang, "Effect of laser intensity on the properties of carbon plasmas and deposited films", *Physical Review B*, **55** (1997) 13213-13220.

[**17**] T.V. Kononenko, V.V. Kononenko, S.M. Pimenov, E.V. Zavedeev, V.I. Konov, V. Romano, G. Dumitru, "Effects of pulse duration in laser processing of diamond-like carbon films", *Diamond and Related Materials*, **14** (2005) 1368-1376.

[**18**] A. Sikora, F. Garrelie, C. Donnet, A.S. Loir, J. Fontaine, J.C. Sanchez-Lopez, T.C. Rojas, "Structure of diamondlike carbon films deposited by femtosecond and nanosecond pulsed laser ablation", *Journal of Applied Physics*, **108** (2010) 113516.

[**19**] I. Horcas, R. Fernández, J.M. Gómez-Rodríguez, J. Colchero, J. Gómez-Herrero, A.M. Baro, "WSXM: A software for scanning probe microscopy and a tool for nanotechnology", *Review of Scientific Instruments*, **78** (2007) 013705.

[**20**] M. Sheik-bahae, A.A. Said, E.W. Van Stryland, "High-sensitivity, single-beam n_2 measurements", *Optics Letters*, **14** (1989) 955-957.

Chapter 3

Effect of cw laser irradiation on DLC films

One of the most powerful technique to characterise the carbon films is Raman spectroscopy [**1**]. It is a nondestructive technique and very sensitive towards the bonding of carbon atoms [**2-4**]. The single crystal graphite exhibits Raman shift at ~1575 cm^{-1}, which is attributed to the Raman active E_{2g} mode of graphite [**5**]. This E_{2g} mode of graphite is commonly referred to as the G band, which appears in all sp^2 hybridized carbon materials. Amorphous carbon containing disordered graphite has G band, positioned in the range 1580-1600 cm^{-1} along with another band at ~1355 cm^{-1}, which is assigned as the D band. The D band is activated from the structural disorder due to the finite crystal size [**6**]. The D band along with the integrated intensity ratio of D band to G band, I_D/I_G, gives the information of disorder in the DLC film. The dispersion of G band can be used for quantitative estimation of sp^3 contents [**7**].

The Raman spectrum is recorded by normally focusing a cw laser beam onto the sample under consideration. The substantially large laser intensity on the DLC film causes local heating in the focal region. This may result in stress and structural relaxation in the film [**8-10**]. These structural relaxations in the film create defects and the corresponding Raman spectrum shows signatures of higher disorder compared to that of actually present in as-deposited DLC film [**11**]. Whereas at low irradiance, the effect may be less pronounced and the disorder induced, if any, may be reversible but at high intensities the focal region of the film may undergo the permanent changes. Therefore, the laser intensity becomes a crucial parameter in recording the Raman spectrum of DLC

film as low intensity results in poor signal to noise ratio whereas higher intensity changes the film properties. The longer exposure of high laser intensity anneals the film sufficiently which causes transformation of sp^3 bonded carbon atoms into sp^2 phase permanently [**12, 13**].

In this chapter, the effect of laser intensity on the Raman spectrum of pulsed laser deposited DLC (PLD-DLC) film is documented to emphasize the importance of optimum laser intensity for Raman measurement without effecting the bonding structures of the film. The structural changes in the DLC film while recording the Raman spectra as a function of excitation laser intensity are assesed from features of G and D bands; peak position, FWHM and I_D/I_G ratio. For this, Raman spectra were deconvoluted by multiple peak fitting using Gaussian Function. Further, the study has been extented to validate the permanent nature of structural changes by laser annealing of DLC film at higher intensity in the range of 127-382 kW/cm^2 for 5 min and recording the Raman specta at lower laser intensity of 114 kW/cm^2. Following this analysis, the Raman spectra of DLC film on Si substrate is also presented to confirm that the accumulated heat is the main cause for the structural changes in DLC film during Raman measurement.

3.1 Experimental details

The DLC films used to study the effect of excitation laser intensity while recording the Raman spectrum were deposited on corning glass and silicon (undoped) substrate at room temperature (RT) via pulsed laser deposition (PLD) technique. For this, a second harmonic of a Q-switched Nd:YAG laser was focused onto the graphite target inside the PLD chamber, evacuated to a base pressure of ~ 10^{-6} mbar. The details of the PLD setup for thin film deposition is described in *Chapter 2, Section 2.1*. The film was deposited for 30 min at a laser fluence of ~11.7 J/cm^2. The thickness of the deposited

film was measured using Stylus profilometer as well as via ellipsometric measurement (*Table 4.4, chapter 4*) and was found to be in the range of 110-120 nm. The Raman spectra as a function of excitation laser intensity were recorded using an Argon ion laser at a wavelength of 488 nm. The spectra were recorded in the range of 800-2000 cm^{-1}. To study the effect of laser annealing on the structural changes in PLD-DLC film, the spectra were recorded at a laser intensity of 114 kW/cm^2 after laser annealing the film for 5 min each in the intensity range of 127-382 kW/cm^2.

3.2 Effect of laser intensity while recording the Raman spectra of PLD-DLC thin film

Figure 3.1 shows the normalized Raman spectra of DLC thin film recorded as a function of laser intensity in the range of 11-382 kW/cm^2. The Raman spectra in the intensity range of 11-114 kW/cm^2, *Figure 3.1 (a)*, are almost similar and exhibit a broad G band centered at ~1550 cm^{-1} with an asymmetric tail extending towards lower wavenumber. The downward shift of the Raman peak for G band w.r.t. that of graphite, 1575 cm^{-1}, is due to the decrease in average C-C bond angle and is proportional to the percentage of sp^3 bonded carbon atoms [**14**]. The variation in deconvoluted spectra with the increase in laser intensity upto 114 kW/cm^2, *Figure 3.2 (a) and (b)*, is small but it is

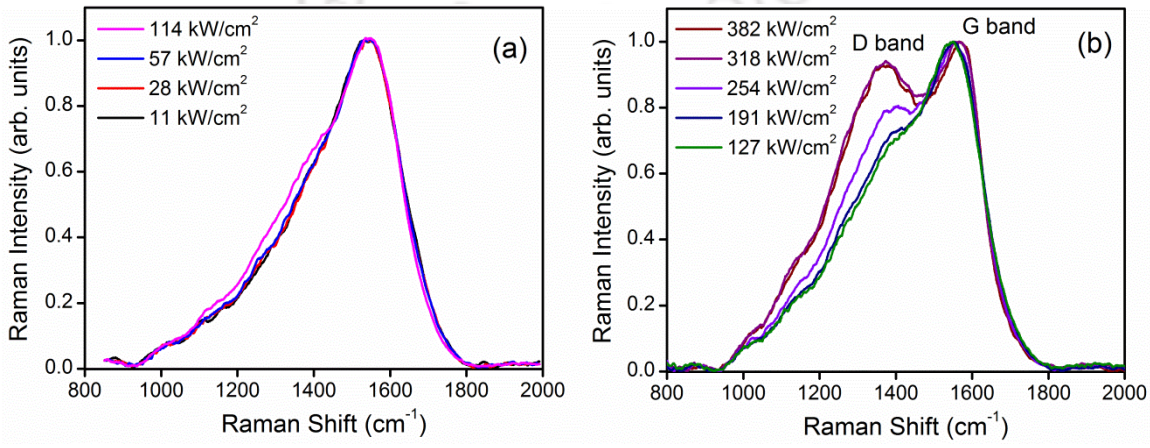

***Figure 3.1**: Raman spectra of DLC film as a function of laser intensity.*

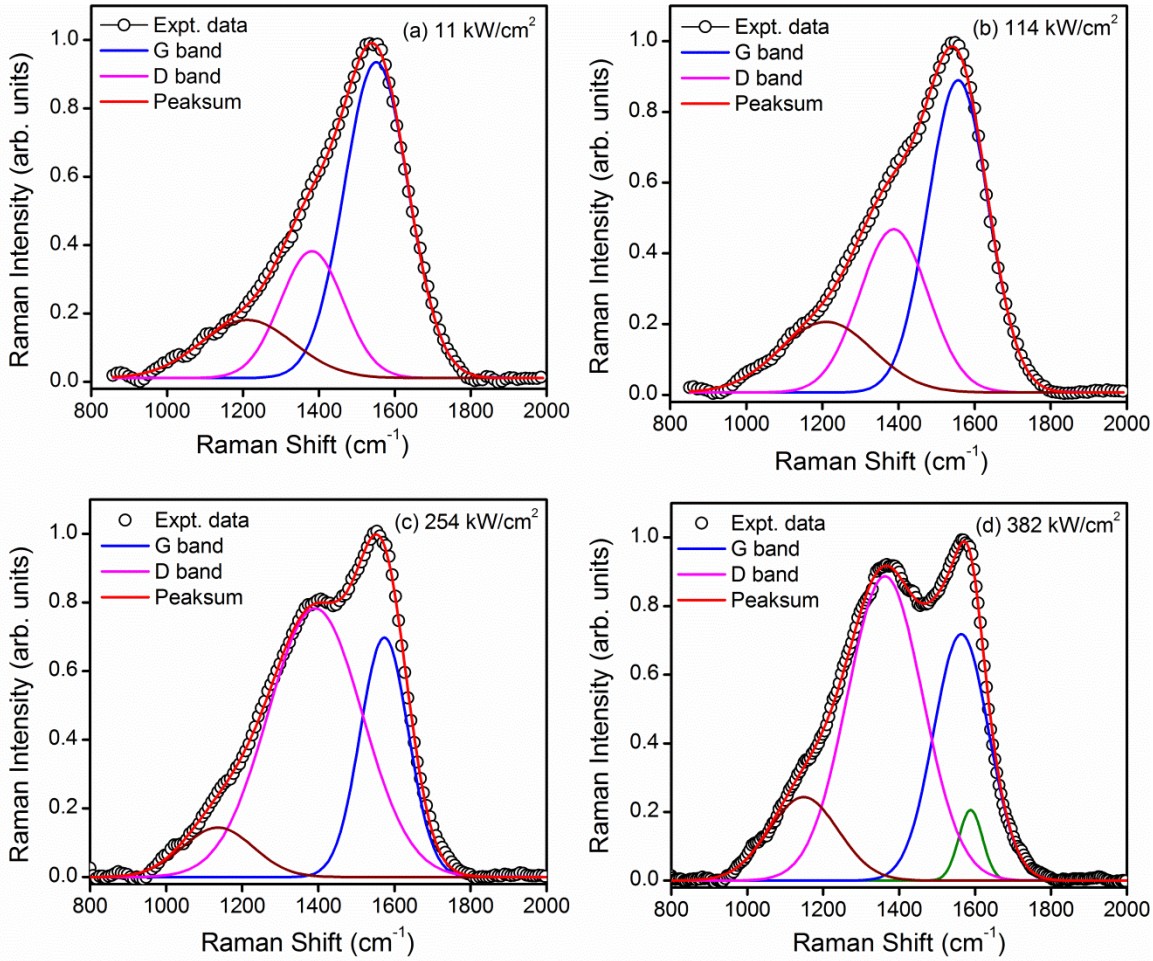

Figure 3.2: *Deconvoluted Raman spectra of DLC thin film as a function of laser intensity;* ***(a)*** *11 kW/cm^2,* ***(b)*** *114 kW/cm^2,* ***(c)*** *254 kW/cm^2 and* ***(d)*** *382 kW/cm^2.*

not of permanent nature and could be retrieved by lowering the laser intensity. The spectra recorded at higher laser intensities; 127 kW/cm^2 and above, *Figure 3.1 (b)*, exhibit the pronounced changes in the film. The major distinction in this range of intensities as compared to that of lower intensity range (11-114 kW/cm^2) is the emergence of D and G bands distinctly, as shown in *Figure 3.1 (b)*. The emergence of D band is the characteristic of the increase in formation of aromatic rings in sp^2 clusters while the emergence of G band reflects the reorganization of the carbon atoms towards graphitic configuration. Hence, the Raman spectra recorded at higher laser intensities reflect the structural changes of DLC film towards sp^2 rich carbon film.

The visible Raman spectroscopy is more sensitive to sp^2 sites of carbon atoms compared to that of sp^3 sites as visible photons preferentially excite π-sites [**15, 16**]. Therefore, the deconvoluted Raman spectra depict the dominating G and D bands corresponding to the sp^2 sites of carbon atoms. The G band corresponds to the zone center phonons of E_{2g} symmetry whereas the D band is induced by structural disorder and attributed to the breathing mode of A_{1g} symmetry due to the phonons near the K zone boundary [**17, 18**]. The origin of third band in the range of 1100-1210 cm^{-1}, *Figure 3.2 (a-d)* could be due to the presence of interfacing amorphous carbon matrix of olefin sp^3 sites to diamond-like structures [**17**]. An additional Raman band (D' band) at ~1600 cm^{-1} is observed at laser intensity of 318 and 382 kW/cm^2, *Figure 3.2(d),* which is attributed to microcrystalline graphite [**19**].

Table 3.1: *Raman band position, FWHM of G and D bands and I_D/I_G ratio of DLC thin film as a function of laser intensity*

Laser intensity (kW/cm^2)	**Position of G band (cm^{-1})**	**Position of D band (cm^{-1})**	**FWHM of G band (cm^{-1})**	**FWHM of D band (cm^{-1})**	**I_D/I_G**
11	1551	1381	198	194	0.39
28	1553	1384	198	199	0.40
57	1556	1388	193	203	0.46
114	1557	1387	185	212	0.59
127	1558	1387	183	218	0.84
191	1569	1396	159	280	1.66
254	1571	1389	149	293	2.21
318	1566	1362	162	269	2.19
382	1562	1360	171	234	1.69

From deconvoluted Raman spectra, peak position of G and D bands, corresponding FWHM and I_D/I_G ratio, were obtained and listed in *Table 3.1* as a function

of laser intensity. At lowest laser irradiance, 11 kW/cm^2, the G band of DLC film was observed to be shifted towards the lower wavenumber (~1551 cm^{-1}) from its position in graphitic films which is reported at ~1583 cm^{-1} [**20**]. The corresponding I_D/I_G ratio was found to be ~0.39. The shift of G band towards lower wavenumber and the low value of I_D/I_G ratio suggest the higher sp^3/sp^2 bonding ratio of carbon atoms in PLD-DLC film [**21**]. Further, the higher concentration of sp^3 bonds of carbon atoms was confirmed by the dispersion of G band, *Figure 3.3*. The G band dispersion is only observed in disordered carbon materials and is proportional to the degree of disorder [**6**]. The peak position of G band shifts towards higher wavenumber with the decrease in excitation laser wavelength for disordered carbon. In the present study, the dispersion rate of G band was measured using three different laser wavelengths (488 nm, 514 nm and 633 nm) and found to be ~0.34 cm^{-1}/nm, *Figure 3.3(b)*, which corresponds to more than 60% of sp^3 content [**6, 7**].

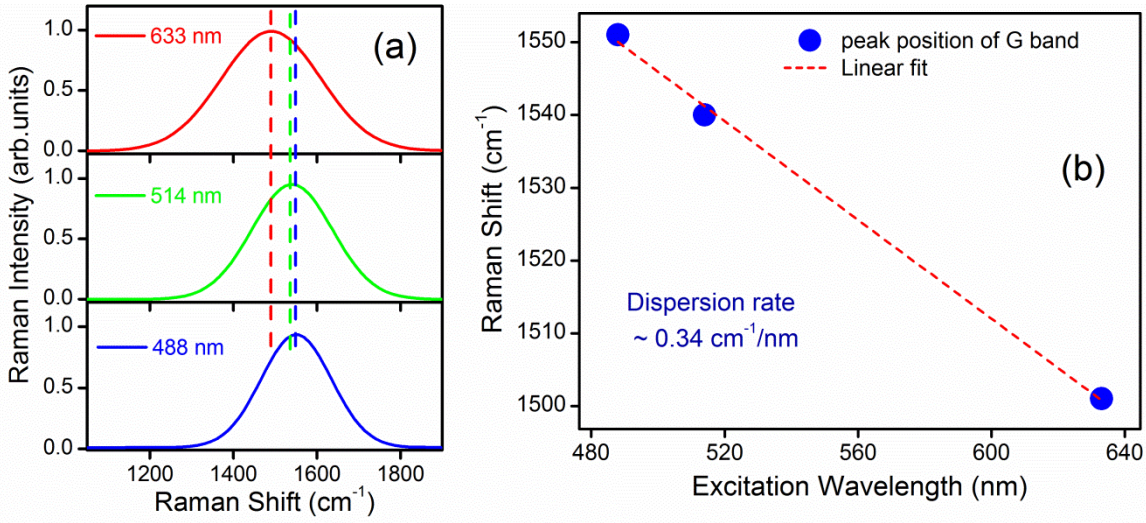

***Figure 3.3: (a)** Dispersion of G band **(b)** Dispersion rate of G band.*

To further unveil the effect of excitation laser power on Raman spectra, all the three observed Raman bands are shown separately, *Figure 3.4 (a)-(c)*, for various laser intensities. The percentage contribution of each band in the Raman spectra in the range

of 800-2000 cm^{-1} is plotted in *Figure 3.5* as a function of laser intensity. The percentage change in the integrated intensity of deconvoluted bands and the total integrated intensity (in the range of 800-2000 cm^{-1}) at various intensities of laser used to record the Raman spectra w.r.t. that of lowest one, 11 kW/cm^2, are listed in *Table 3.2*.

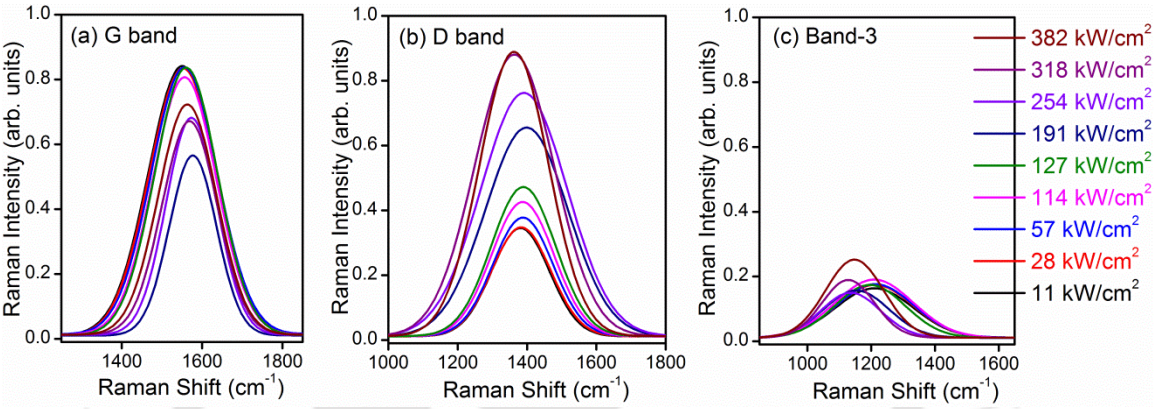

Figure 3.4: ***(a)*** *G band,* ***(b)*** *D band and* ***(c)*** *Band-3 (~1200 cm^{-1}) as a function of laser intensity.*

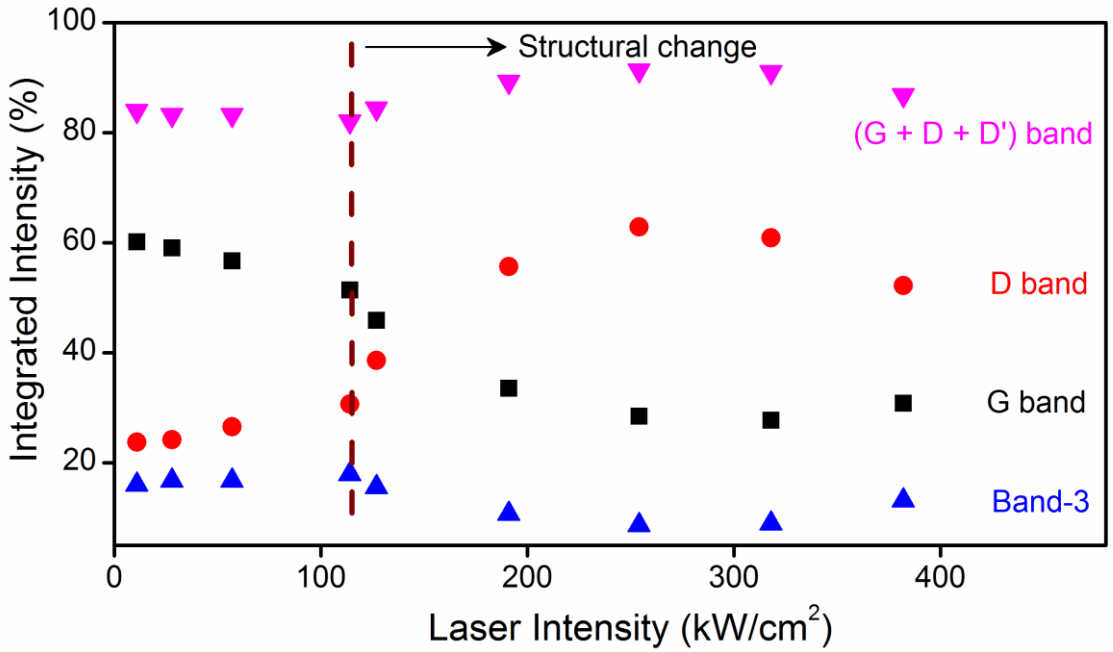

Figure 3.5: *Integrated intensity of Raman bands as a function of laser intensity.*

There was a gradual decrease in integrated intensity of G band (I_G) with the increase in laser intensity in the range of 11-114 kW/cm^2 to a maximum of ~10% whereas that of the other bands, D band and Band-3 (~1210 cm^{-1}), it increased by ~35%

***Table 3.2**: Percentage Change in integrated intensity of Raman spectra of PLD-DLC film and their deconvoluted bands as a function of laser intensity w.r.t. laser intensity of 11 kW/cm^2.*

Laser intensity (kWcm^{-2})	**Change in integrated intensity of convoluted spectra (%)**	**Change in integrated intensity of G band, I_G (%)**	**Change in integrated intensity of D band, I_D (%)**	**Change in integrated intensity of Band-3 (%)**
11	--	--	--	--
28	1.22	- 0.72	3.18	5.52
57	2.56	- 3.35	14.57	6.89
114	4.93	- 10.36	35.22	17.41
127	16.69	-11.07	89.44	13.04
191	18.70	-33.80	178.09	-20.41
254	27.87	-39.49	238.29	-31.09
318	40.41	-35.31	259.68	-21.66
382	43.53	-26.44	215.44	-17.32

and ~17% , respectively, *Figure 3.5*. The changes in integrated intensity of these bands were also reflected by the change in respective FWHM and I_D/I_G ratio as listed in *Table 3.1*. The changes in the position of G and D bands with the laser intensity are marginal upto the laser intensity of 114 kW/cm^2. The FWHM of G band reflects the structural ordering of sp^2 phase of carbon atoms in the DLC film. In this intensity range, FWHM of G band was observed to be decreased from 198 cm^{-1} to 185 cm^{-1} with the increase in laser intensity, *Table 3.1*, which may be due to the improvement in ordering within the sp^2 clusters. Another reason for the decrease in FWHM of G band could be the release of compressive stress of the film on exposure of laser beam during measurement [**4**]. During recording of Raman spectra, the heating in the focal region raises the temperature locally which results into releasing the stress in the film. The relaxation of stress could also be due to the generation of topological defects such as odd rings; 5-fold and 7-fold rings of carbon atoms [**22**]. These topological defects give the higher value of I_D/I_G ratio.

The increase in I_D/I_G ratio was observed to be from 0.39 to 0.59 with increase in laser intensity from 11 kW/cm^2 to 114 kW/cm^2, respectively. The corresponding increase in FWHM of D band was observed to be from 194 cm^{-1} to 212 cm^{-1}. The increase in FWHM of D band and I_D/I_G ratio with laser intensity indicate the overall increase in disorder due to the local heating in the focal region.

The increase in I_D/I_G ratio inspite of improvement in the ordering of sp^2 clusters in the film was observed with the increase in laser intensity. The I_D/I_G ratio and the FWHM of G band together give the rough estimation of cluster size in *a-C* films. The larger value of FWHM of G band ($\Delta\nu$ > 50 cm^{-1}) and the smaller value of I_D/I_G ratio is indicative of a cluster size smaller than 10 Å. The G band appears from the graphitic sites only and become ordered at higher laser intensity during Raman measurement as reflected by the decrease in its FWHM. The disorder increases in non-graphitic sites with the increase in laser intensity which increases the I_D/I_G ratio inspite of reduction in defects in sp^2 clusters.

The marginal changes observed during recording of Raman spectra with the increase in laser intensity upto 114 kW/cm^2 are reversible. As the laser intensity increased beyond 114 kW/cm^2, D and G bands appeared to be resolved, *Figure 3.1 (b)*. The increase in I_D/I_G ratio with the laser intensity was observed, indicating the evolution of more sp^2 aromatic rings in DLC film. The increase in I_D/I_G ratio was small upto laser intensity of 127 kW/cm^2, but beyond that it was substantial, *Table 3.1*. This indicates that the effective conversion of sp^3 to sp^2 commences above 127 kW/cm^2 of laser intensity. The thermal energy provided by the laser in this range is sufficient to convert the metastable carbon bonds of DLC film to more stable sp^2 bonding state. As a result, diamond-like amorphous matrix shrinks while sp^2 clusters grow with the increase in laser intensity. The increase in sp^2 clusters with laser intensity can be further confirmed by

observing the enhancement in integrated intensity for all the three bands (G + D + D'), *Figure 3.5*, as all these bands are due to sp^2 sites only. The peak position of G band continued to shift to higher wavenumber with the increase in laser intensity upto 254 kW/cm^2, *Table 3.1*. The upward shift of G band signifies the aggregation of sp^2 clusters into larger domain as well as ordering among them. As the laser intensity was increased beyond 254 kW/cm^2, the downward shift of the G band was observed, indicating the fragmentation of sp^2 clusters into smaller domain. It may be due to the sufficient rise of temperature in the focal region of the film surface at such high laser intensity to break the bond or fragment into smaller clusters of sp^2. There is also increase in disordered orientation of sp^2 clusters as reflected by the decrease in I_D/I_G ratio and increase in FWHM of G band for the laser intensity beyond 254 kW/cm^2, *Table 3.1*. At laser intensity of 382 kW/cm^2, the slight decrease in overall integrated intensity (G + D + D' bands) was observed impling the reduction in sp^2 sites which could be due to damage of these sp^2 sites at such high laser intensity resulting from local heating.

The integrated intensity of G band (I_G) was observed to decrease whereas that of the D band (I_D) increased with the laser intensity, *Figure 3.5*, in the range of higher intensity above 127 kW/cm^2. The total integrated intensity of the Raman spectra in the range of 800-2000 cm^{-1} was observed to increase with the intensity of laser used to record Raman spectra indicating the increase in sp^2 clusters. The blue shift in G band position and the decrease in corresponding FWHM further confirm the increase in sp^2 clusters with the increase in laser intensity while recording the Raman spectra. These changes were irreversible as was confirmed by recording the Raman spectra later at a reduced laser intensity of 114 kW/cm^2.

3.3 Effect of laser annealing on structural changes in PLD-DLC thin film

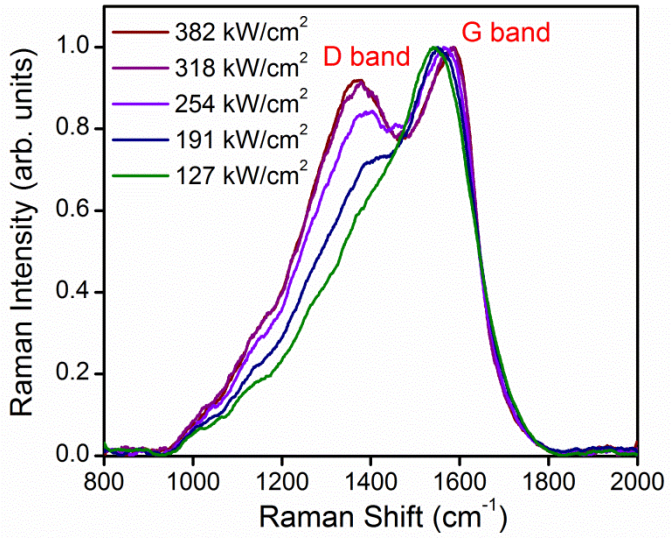

Figure 3.6: *Raman spectra of DLC thin film recorded at 114 kW/cm^2 after laser annealing for 5 min in the intensity range 127-382 kW/cm^2.*

The effect of laser intensity while recording the Raman spectra of DLC film is described in *Section 3.2*. It was observed that in the laser intensity range of 11-114 kW/cm^2, the effect is less pronounced and reversible whereas the structural changes occurred at laser intensities above 114 kW/cm^2 are prominent and irreversible. To validate it further, the DLC film was annealed for 5 min at each laser intensity in the range of 127-382 kW/cm^2 and then Raman spectra were recorded at 114 kW/cm^2, as this laser intensity doesn't bring any significant changes in the carbon bonding within the laser exposed area of the film. The Raman spectra of laser annealed DLC film are shown in *Figure 3.6*. The spectra displayed the features similar to those of respective as-deposited film of *Figure 3.1 (b)*, confirming that higher intensity of laser is capable of bringing the permanent structural changes in DLC film. The Raman spectra of DLC film recorded at a laser intensity of 382 kW/cm^2 and the one recorded at 114 kW/cm^2 after laser annealing at the intensity of 382 kW/cm^2 are shown in *Figure 3.7 (a)*. The corresponding deconvoluted Raman spectrum of the annealed film is shown in *Figure*

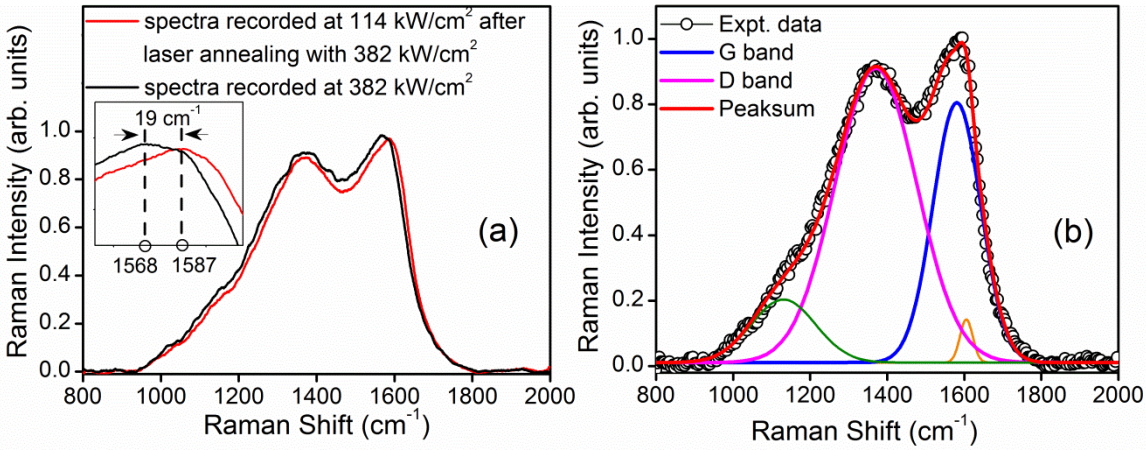

***Figure 3.7**: **(a)** Comparison of Raman spectra of as-deposited thin film and that of after laser annealing at intensity of 382 kW/cm^2 and **(b)** corresponding deconvoluted Raman spectrum of laser annealed DLC thin film.*

3.7 (b). A nearly similar emergence of G and D bands in both the situations implies the same bonding structure, the only difference is in the peak position of G band. The peak position of G band was observed to be shifted by ~19 cm^{-1} towards higher wavenumber after laser annealing. During Raman measurement, at high laser intensity, the film is under the process of annealing and the structural arrangements are not stable. But after laser annealing, the localized sp^2 clusters rearranged in the ordered graphitic domain thus causing the upward shift of G band along with decrease in its FWHM as depicted in *Figure 3.8*. *Table 3.3* lists the peak position of G and D bands, respective FWHM and

***Table 3.3**: Raman band position, FWHM of G and D bands and I_D/I_G ratio of laser annealed DLC thin film*

Annealing Laser intensity (kWcm^{-2})	**Peak position of G band (cm^{-1})**	**Peak position of D band (cm^{-1})**	**FWHM of G band (cm^{-1})**	**FWHM of D band (cm^{-1})**	**I_D/I_G**
127	1558	1397	182	210	0.66
191	1570	1385	164	254	1.26
254	1579	1380	150	299	2.26
318	1582	1378	145	265	2.17
382	1580	1377	143	240	1.87

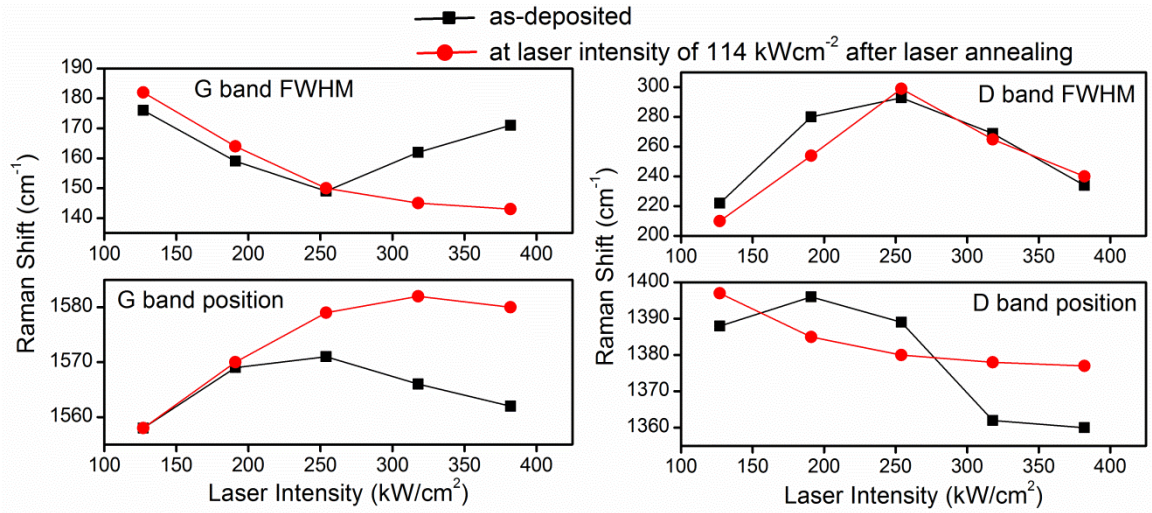

Figure 3.8: *Comparison of band parameters of G and D bands at high laser intensity and after laser annealing.*

I_D/I_G ratio (recorded at laser intensity of 114 kW/cm^2) as a function of the laser intensity used for annealing. These band features were compared with those of as-deposited film at respective laser intensities (*Figure 3.1 (b)*) and plotted in *Figure 3.8*. The peak position of G band was found to shift to higher wavenumber and approaching towards that of graphitic film with the increase in annealing laser intensity. The FWHM of G band was also observed to decrease with the laser annealing. At annealing laser intensity of 382 kW/cm^2, the FWHM was 143 cm^{-1} which is significantly lower than that of as-deposited film (~185 cm^{-1} recorded at laser intensity of 114 kW/cm^2). The upward shift in G band and decrease in its FWHM are an indication of the rearrangements of sp^2 sites towards graphitic order. The I_D/I_G ratio was found to be increased from 0.66 to 2.26 with the annealing laser intensity from 127 kW/cm^2 to 254 kW/cm^2, respectively, *Table 3.3*. The increase in FWHM of D band and I_D/I_G ratio with laser intensity further confirm the formation of more sp^2 rings. With further increase in laser intensity (318 and 382 kW/cm^2), the FWHM of D band and I_D/I_G ratio were observed to decrease from 299 to 240 cm^{-1} and 2.26 to 1.87, respectively. This implies the decrease in aromatic rings in sp^2 clusters which may be due to the conversion of rings into chains (small graphitic planes).

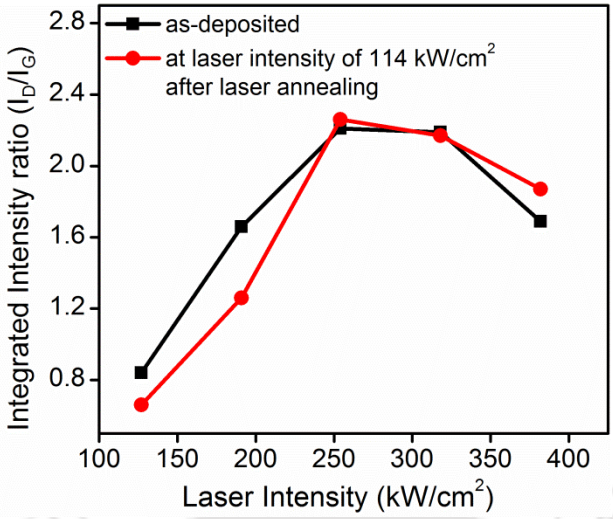

Figure 3.9: *Integrated intensity ratio, I_D/I_G, of as-deposited film and after laser annealing.*

The localized heating at high laser intensity provides the sufficient thermal activation energy to reform the bonds. This gives rise to the ordering of carbon atoms in sp^2 phase which is reflected by reduction in FWHM of G band as well as that of D band, *Table 3.3*. The I_D/I_G ratio after laser annealing was also compared with that of as-deposited film at respective laser intensities, shown in *Figure 3.9*, and found to be following the same trend. *Figure 3.8 and 3.9* show that all the changes were irreversible confirming the permanent conversion of sp^3 bonded carbon atoms to sp^2 clusters in DLC thin film at high laser intensity.

3.4 Effect of substrate on structural modification of DLC thin film at high laser intensity

At higher laser irradiation, the structural transformation of DLC film from diamond-like to graphite-like occurs due to localized accumulation of heat in the focal region. Since the film thickness is in nanometer (~120 nm) range only, the substrate plays an important role to accumulate the heat during Raman measurement. To study the substrate effect, DLC film was deposited on silicon substrate simultaneously along with the glass substrate. The Raman spectra of laser annealed DLC thin film on silicon

substrate as a function of laser intensities in the range 127-382 kW/cm^2 is shown in *Figure 3.10*.

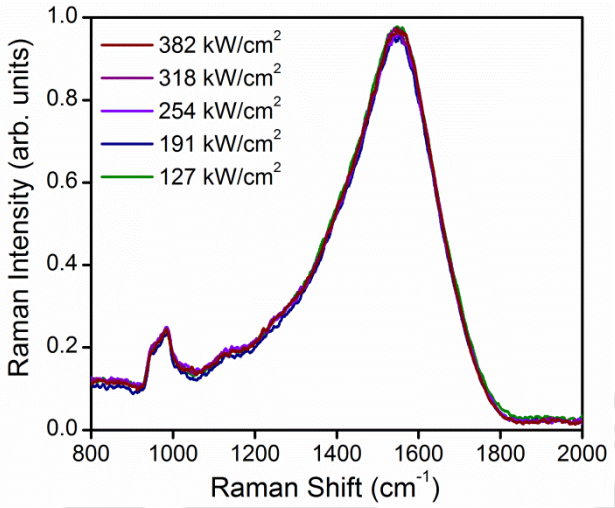

***Figure 3.10**: Raman spectra of DLC film on silicon substrate at various laser intensities.*

The laser annealed DLC film on corning glass substrate indicates the graphitization, *Figure. 3.6*, with the increase in laser intensity whereas the film deposited on silicon substrate doesn't show any such change. This is due to the difference in accumulated heat in the focal region in case of two different substrates. The accumulation of heat depends on the thermal conductivity of substrate as well as thermal conductivity and thickness of DLC film. The films on both substrates were deposited simultaneously and the thickness was found to be nearly equal. The Raman spectra of DLC film on silicon substrate (*Figure 3.10*) is almost similar to that of DLC film on glass substrate recorded at laser intensity of 114 kW/cm^2, *Figure 3.1 (a)*, indicating that the DLC films deposited on glass and silicon substrates are of same sp^3/sp^2 composition and so the difference in the accumulation of heat due to film properties can be ruled out. The accumulation of heat mainly results from the thermal conductivity of substrate. The thermal conductivity of glass is ~0.8 W/mK whereas that of silicon is ~150 W/mK. Due to low thermal conductivity of glass substrate, the film retains a large fraction of heat resulting in a large

increase in temperature in the focal region which is sufficient enough to change the carbon bonding. In case of silicon as a substrate, the amount of thermal energy absorbed by the film is removed from focal region due to the high thermal conductivity of the substrate inhibiting the rise of temperature and thus shows negligible affect on the structural transformation of the film even at high laser intensity.

Conclusion

The focusing of the laser beam at high intensities on the film surface causes the local heating which is sufficient to change the bonding structure in DLC thin film. This was confirmed by observing the increase in I_D/I_G ratio with increasing laser intensity. The weak dependence of the Raman shift of D and G bands on the irradiated laser intensity upto 114 kW/cm^2 suggests that there is no significant change in the proportion of sp^2 and sp^3 contents in DLC film. The higher laser intensity leads to thermal annealing of the DLC film which favors sp^2 clustering and sp^3 to sp^2 conversion. As a result, the Raman spectra of DLC film recorded at higher laser intensity beyond 114 kW/cm^2 show characteristic of sp^2 enriched a-C film. This was further confirmed by deliberately annealing the film with laser in the intensity range of 127-382 kW/cm^2 for 5 min and then recording the Raman spectra at laser intensity of 114 kW/cm^2. Therefore, the characterization of the DLC films via Raman spectrum should be performed at optimum laser intensity so as to prevent the film undergoing any permanent changes.

Bibliography

[**1**] Y. Wang, D.C. Alsmeyer, R.L. McCreery, "Raman spectroscopy of carbon materials: structural basis of observed spectra", *Chemistry of Materials*, **2** (1990) 557-563.

[**2**] M. Yoshikawa, G. Katagiri, H. Ishida, A. Ishitani, T. Akamatsu, "Raman spectra of diamondlike amorphous carbon films", *Solid State Communications*, **66** (1988) 1177-1180.

[**3**] G. Morell, O. Quiñones, Y. Díaz, I.M. Vargas, B.R. Weiner, R.S. Katiyar, "Measurement and analysis of diamond Raman bandwidths", *Diamond and Related Materials*, **7** (1998) 1029-1032.

[**4**] J. Schwan, S. Ulrich, V. Batori, H. Ehrhardt, S.R.P. Silva, "Raman spectroscopy on amorphous carbon films", *Journal of Applied Physics*, **80** (1996) 440-447.

[**5**] F. Tuinstra, J.L. Koenig, "Raman spectrum of graphite", *The Journal of Chemical Physics*, **53** (1970) 1126-1130.

[**6**] A.C. Ferrari, J. Robertson, "Raman spectroscopy of amorphous, nanostructured, diamond–like carbon, and nanodiamond", *Philosophical Transactions of the Royal Society of London A*, **362** (2004) 2477-2512.

[**7**] W.G. Cui, Q.B. Lai, L. Zhang, F.M. Wang, "Quantitative measurements of sp^3 content in DLC films with Raman spectroscopy", *Surface and Coatings Technology*, **205** (2010) 1995-1999.

[**8**] M. Lejeune, O. Durand-Drouhin, S. Charvet, A. Zeinert, M. Benlahsen, "On the induced microstructure changes of the amorphous carbon nitride films during annealing", *Journal of Applied Physics*, **101** (2007) 123501.

[**9**] J.A. Thornton, D.W. Hoffman, "Stress-related effects in thin films", *Thin Solid Films*, **171** (1989) 5-31.

[**10**] A.C. Ferrari, B. Kleinsorge, N.A. Morrison, A. Hart, V. Stolojan, J. Robertson, "Stress reduction and bond stability during thermal annealing of tetrahedral amorphous carbon", *Journal of Applied Physics*, **85** (1999) 7191-7197.

[**11**] M. Lejeune, R. Bouzerar, M. Benlahsen, O. Durand-Drouhin, A. Zeinert, "Instability of hydrogenated amorphous carbon films towards defect creation at high disorder", *Applied Physics Letters*, **79** (2001) 3443-3445.

[**12**] T.A. Friedmann, K.F. McCarty, J.C. Barbour, M.P. Siegal, D.C. Dibble, "Thermal stability of amorphous carbon films grown by pulsed laser deposition", *Applied Physics Letters*, **68** (1996) 1643-1645.

[**13**] E. Cappelli, C. Scilletta, S. Orlando, V. Valentini, M. Servidori, "Laser annealing of amorphous carbon films", *Applied Surface Science*, **255** (2009) 5620-5625.

[**14**] D. Beeman, J. Silverman, R. Lynds, M.R. Anderson, "Modeling studies of amorphous carbon", *Physical Review B*, **30** (1984) 870-875.

[**15**] S.R. Sails, D.J. Gardiner, M. Bowden, J. Savage, D. Rodway, "Monitoring the quality of diamond films using Raman spectra excited at 514.5 nm and 633 nm", *Diamond and Related Materials*, **5** (1996) 589-591.

[**16**] N. Wada, P.J. Gaczi, S.A. Solin, ""“Diamond-like” 3-fold coordinated amorphous carbon", *Journal of Non-Crystalline Solids*, **35–36, Part 1** (1980) 543-548.

[**17**] S. Neuville, "Quantum electronic mechanisms of atomic rearrangements during growth of hard carbon films", *Surface and Coatings Technology*, **206** (2011) 703-726.

[**18**] A.C. Ferrari, J. Robertson, "Interpretation of Raman spectra of disordered and amorphous carbon", *Physical Review B*, **61** (2000) 14095-14107.

[**19**] R.J. Nemanich, S.A. Solin, "First- and second-order Raman scattering from finite-size crystals of graphite", *Physical Review B*, **20** (1979) 392-401.

[**20**] S. Reich, C. Thomsen, "Raman spectroscopy of graphite", *Philosophical Transactions of the Royal Society of London A*, **362** (2004) 2271-2288.

[**21**] S. Zhang, X.T. Zeng, H. Xie, P. Hing, "A phenomenological approach for the I_d/I_g ratio and sp^3 fraction of magnetron sputtered a-C films", *Surface and Coatings Technology*, **123** (2000) 256-260.

[**22**] M. Lejeune, M. Benlahsen, R. Bouzerar, "Stress and structural relaxation in amorphous hydrogenated carbon films", *Applied Physics Letters*, **84** (2004) 344-346.

Chapter 4

Characterization of pulsed laser deposited DLC and graphitic thin films

Diamond-like carbon (DLC) thin film consists of sp^3 and sp^2 bonding of carbon atoms. The variation in sp^3/sp^2 fraction tunes its physical properties; hardness, friction coefficient, wear resistance, thermal conductivity, optical properties, etc. [**1-4**]. These properties make DLC films an important candidate in the field of research and industry [**5-10**]. For the application of DLC films at high temperature, the films should be hydrogen-free as it is more stable at higher temperature as compared to that of hydrogenated DLC films [**11-13**]. Such films can be easily fabricated by pulsed laser deposition (PLD) technique as it doesn't involve any hydrogen gas (or its compound) as a precursor. The properties of DLC films can be tailored by deposition parameters [**14-18**]. One of these parameters is a substrate temperature which can tune the sp^3/sp^2 ratio over a broad range [**15, 19, 20**]. Deposition at room temperature (RT) favours sp^3 bonding whereas high temperature favours the formation of sp^2 dominating films. The films containing nearly 100% sp^2 are termed as graphitic films. The graphitic thin films exhibit good thermal and electrical conductivity, high transparency, biocompatibility, etc. [**21-24**]. These properties lead to its application as flexible transparent electrodes in nanoelectronics and as a coating for body implants [**24, 25**].

In this chapter, the effect of substrate temperature, laser fluence and helium gas

pressure on the structural and optical properties of DLC films is presented. The effect of helium gas pressure is also studied on fabrication of ordered graphitic thin films.

4.1 Experimental details

A schematic of PLD system used for the deposition of DLC thin films is shown in *Figure 2.1* (*Chapter 2*). DLC thin films were deposited over a broad range of deposition parameters in order to obtain the higher sp^3 fraction of carbon atoms in the film. In the present thesis, substrate temperature was selected as the first parameter to study its effect on sp^3/sp^2 ratio in DLC film. The substrate temperature was varied from RT to 750 °C. The films were deposited for 5 min onto fused silica substrate at a base pressure of ~10^{-5} mbar and a laser fluence of ~5.0 J/cm^2. The higher sp^3/sp^2 ratio was found in the film deposited at RT. Thus at RT, the effect of laser fluence on the sp^3 fraction in DLC was studied. For this, DLC thin films were deposited for 30 min on corning glass and silicon substrates at laser fluence of 5.0 J/cm^2, 6.7 J/cm^2, 8.3 J/cm^2, 10.0 J/cm^2 and 11.7 J/cm^2 at ~10^{-5} mbar. At laser fluence of 11.7 J/cm^2, the ejection of large particulates from the graphite target was observed. To overcome this, films were deposited in the presence of helium gas. The effect of helium pressure on DLC thin films was studied by depositing the films on corning glass substrate at 0.05 mbar, 0.1 mbar, 0.5 mbar and 1 mbar of helium pressure while keeping the deposition temperature and deposition time fixed at RT and 30 min, respectively. The effect of laser fluence on DLC thin films was also studied in the presence of helium gas ambient. For this, at each value of helium pressure, the DLC films were deposited at various laser fluences; 10.0 J/cm^2, 11.7 J/cm^2, 13.3 J/cm^2 and 15.0 J/cm^2 for 30 min on corning glass substrate as listed in *Table 4.1*.

The film deposited at substrate temperature of 750 °C was found to be graphitic in nature. In order to study the effect of helium gas pressure onto the structural order of sp^2 bonded carbon atoms in graphitic film, the third harmonic of a Q-switched Nd:YAG laser was used. The graphitic films were deposited on corning glass substrate at a base pressure of 10^{-5} mbar and helium pressure of 0.1 mbar, 1 mbar, 5 mbar and 10 mbar. The deposition was performed for 5 min duration and at a laser fluence of ~5.0 J/cm^2.

The structural information and bonding fraction (sp^3/sp^2) in the pulsed laser deposited DLC (PLD-DLC) thin films were analysed by micro-Raman spectrometer. The Raman measurements were performed at a laser intensity of 114 kW/cm^2, *Chapter 3*. For quantitative estimation of sp^3/sp^2 ratio, the dispersion in peak position of G band was measured by recording the Raman spectra at three different laser excitation wavelengths; 488 nm, 514 nm and 633 nm. The absence of hydrogen in DLC thin films was confirmed by recording the Fourier transform infrared (FTIR) transmission spectra. Spectroscopic ellipsometer was used to study the linear optical properties of PLD films. The surface morphology was recorded using Atomic force microscope.

4.2 Effect of deposition parameters on DLC thin films

The DLC thin films were deposited over the wide range of parameters listed in *Table 4.1*. In the following subsections the effect of substrate temperature, laser fluence and helium gas pressure is detailed.

Table 4.1: *Deposition parameters for the fabrication of DLC thin films*

Deposition pressure	**Laser fluence**	**Deposition time**	**Substrate**	**Substrate temperature**
10^{-5} mbar (base pressure)	5.0 J/cm^2	5 min	fused silica	RT
				100 °C
				200 °C
				300 °C
				400 °C
				500 °C
				600 °C
				700 °C
				750 °C
	5.0 J/cm^2	30 min	corning glass, silicon	RT
	6.7 J/cm^2			
	8.3 J/cm^2			
	10.0 J/cm^2			
	11.7 J/cm^2			
0.05 mbar helium	10.0 J/cm^2	30 min	corning glass	
0.1 mbar helium				
0.5 mbar helium				
1 mbar				
0.05 mbar helium	11.7 J/cm^2			
0.1 mbar helium				
0.5 mbar helium				
1 mbar helium				
0.05 mbar helium	13.3 J/cm^2			
0.1 mbar helium				
0.5 mbar helium				
1 mbar helium				
0.05 mbar helium	15.0 J/cm^2			
0.1 mbar helium				
0.5 mbar helium				
1 mbar helium				

4.2.1 Effect of substrate temperature on PLD-DLC thin films

To study the effect of substrate temperature, films were deposited on fused silica substrate at RT and elevated substrate temperature of 100 °C, 200 °C, 300 °C, 400 °C, 500 °C, 600 °C, 700 °C and 750 °C. The other deposition parameters were kept fixed as listed in *Table 4.1*. The film thickness was measured by stylus profilometer and found to be in the range of 27-33 nm. Thus, the thickness is nearly independent of temperature.

4.2.1.1 Raman spectra of DLC thin films deposited at various substrate temperature

The microstructure and the bonding configuration in the PLD carbon thin films were evaluated using micro-Raman spectrometer at the excitation laser wavelength of 514 nm. The Raman spectra of carbon thin films deposited at RT, 100 °C, 200 °C, 300 °C, 400 °C ,500 °C, 600 °C, 700 °C and 750 °C are shown in *Figure 4.1*. The spectrum for the sample deposited at RT shows a broad band centred at ~1540 cm^{-1} with a broad

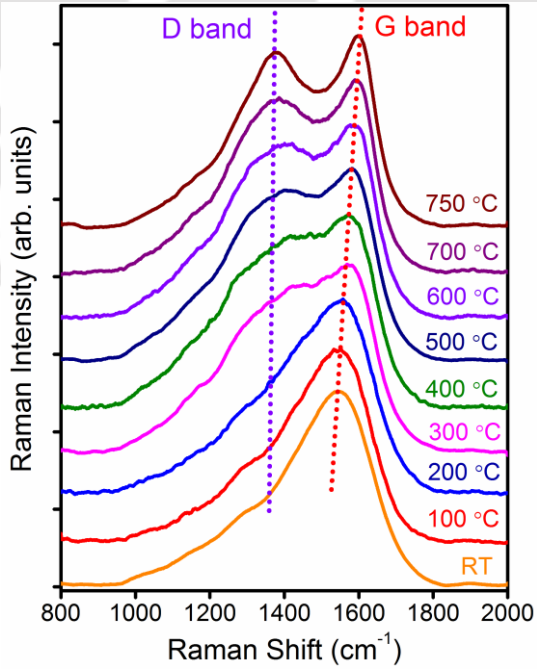

***Figure 4.1**: Raman spectra of DLC thin films deposited on fused silica substrate as a function of substrate temperature.*

tail towards lower wavenumber, indicating that the film is enriched with the sp^3 bonded carbon atoms [**26**]. The films deposited at the substrate temperatures of 300 °C and above exhibit the evolution of D (~1350 cm^{-1}) and G (~1580 cm^{-1}) bands distinctly; the characteristic of disordered sp^2 and sp^3 network of carbon atoms [**1, 27**]. The D band corresponds to the breathing vibrations of aromatic rings and activated from the structural disorder in the film. The G band is assigned to the stretching modes of C-C sp^2 bonds in aromatic rings or in chains containing C=C sp^2 bonds [**27**]. The position of G band lies at ~1575 cm^{-1} in the case of single crystal graphite whereas for disordered graphite, it lies in the range of 1580-1600 cm^{-1} [**27, 28**]. The G band shifts towards lower wavenumber when it originates from the sp^2 clusters embedded in the amorphous matrix

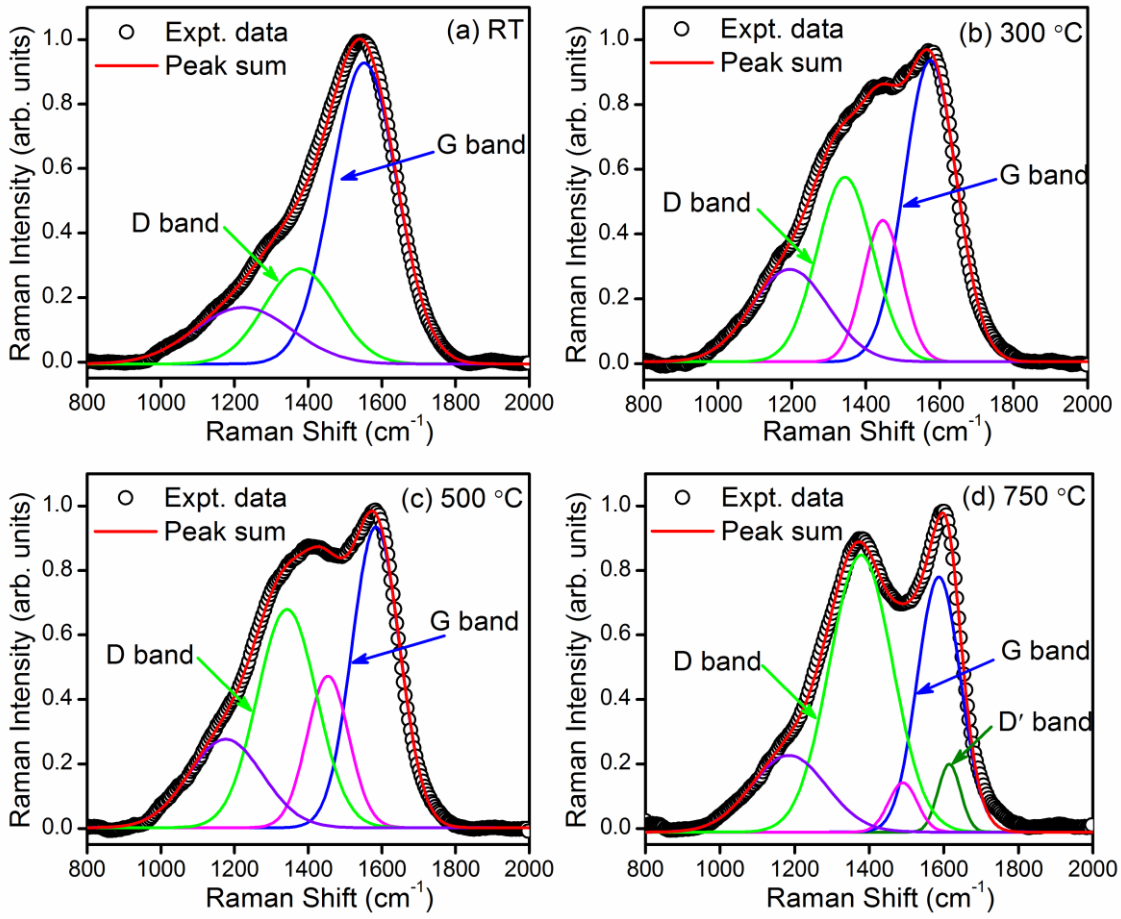

Figure 4.2: *Deconvoluted Raman spectra of carbon thin films deposited at* ***(a)*** *RT,* ***(b)*** *300 °C,* ***(c)*** *500 °C and* ***(d)*** *750 °C.*

of diamond-like structures [**26**]. *Figure 4.2 (a-d)* shows the deconvoluted spectra for the film deposited at substrate temperature of RT, 300 °C, 500 °C and 750 °C, respectively. The deconvoluted Raman spectra of all the samples display the dominating G band. The Raman shift of G band increases from 1552 cm^{-1} for the film deposited at RT to 1586 cm^{-1} for that of at 750 °C as shown in *Figure 4.3 (a).* The ratio of the integrated intensity of D band to that of G band, I_D/I_G, is also shown in the same figure exhibiting the increasing trend with respect to the temperature changing from ~0.34 at RT to ~1.59 at 750 °C. The evolution of distinct D and G band and increase in Raman shift of G band towards its graphitic range (1580-1600 cm^{-1}) along with the increase in I_D/I_G ratio with increase in substrate temperature suggests that diamond-like amorphous matrix is shrinking while sp^2 clusters are growing with the increasing deposition temperature [**29, 30**].

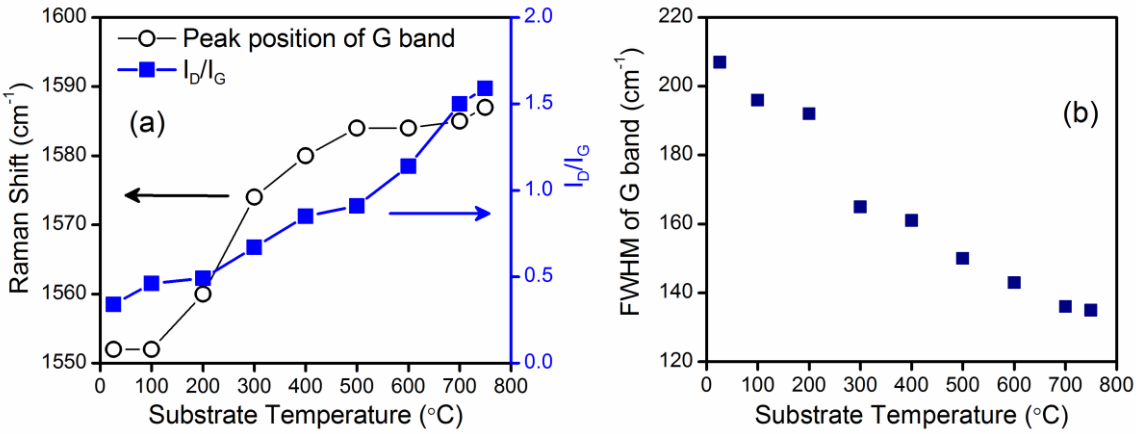

Figure 4.3: (a) *Peak position of G band and I_D/I_G ratio as a function of substrate temperature and* ***(b)*** *Variation of FWHM of G band with substrate temperature.*

The variation in FWHM of G band as a function of substrate temperature is shown in *Figure 4.3 (b)* which decreases from 208 cm^{-1} at RT to 135 cm^{-1} at 750 °C further confirming the growth of sp^2 clusters. This is due to the conversion of sp^3 sites into sp^2 aromatic rings as a result of enhanced surface diffusion at the elevated substrate temperature during deposition. Thus, the thin film deposited at substrate temperature of

750 °C is more graphite-like compared to that of the other films [**20, 27**]. *Figure 4.4 (a)* shows the decrease in I_D/I_G ratio with the corresponding increase in FWHM of G band indicating that the sp^2 cluster size is very small and is of the order of 10 Å [**31**]. The size of sp^2 clusters in amorphous carbon films can be estimated by using *Equation (4.1)* [**27**].

$$\frac{I_D}{I_G} = C'(\lambda)L_a^2 \tag{4.1}$$

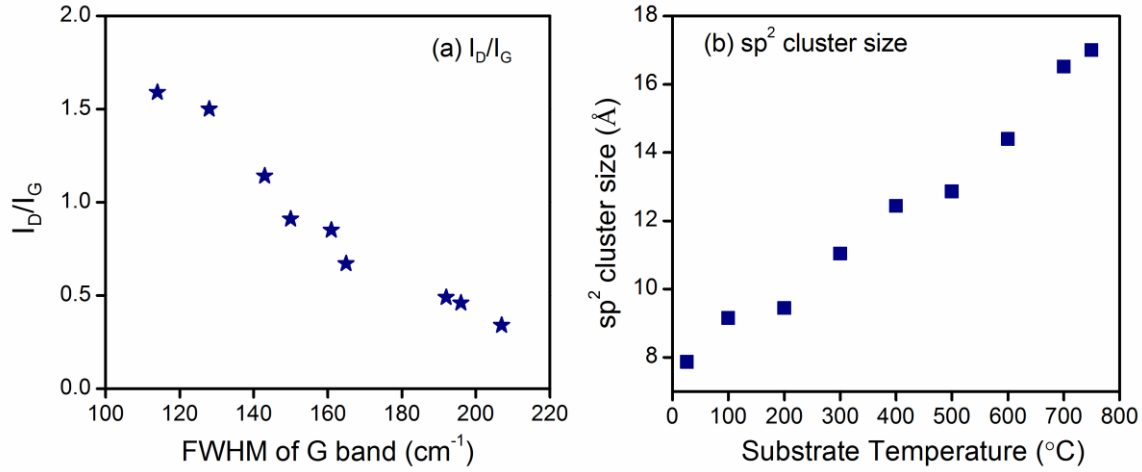

Figure 4.4: (a) *I_D/I_G ratio as a function of FWHM of G band and* ***(b)*** *sp^2 cluster size as a function of substrate temperature.*

where, C'(514 nm)=0.0055. The sp^2 cluster size estimated from *Equation (4.1)* was found to be increasing with the substrate temperature, as depicted in *Figure 4.4 (b).* The increase in substrate temperature increases the diffusivity of carbon adatoms which coalesces with each other thus forming clusters of bigger size.

The sp^3/sp^2 ratio can be quantitatively obtained by the dispersion of G band using *Equation (1.1), Chapter 1* [**32**]. The dispersion of G band was measured by recording the Raman spectra at three different excitation laser wavelengths; 488 nm, 514 nm and 633 nm, *Figure 4.5 (a).* The dispersion of G band was observed to be decreasing with the increase in deposition temperature and vanished for the film deposited at the substrate temperature of 750 °C, *Figure 4.5 (b).* The corresponding sp^3 content in the film

deposited at RT, estimated using *Equation (1.1), Chapter 1*, was found to be ~68 % which decreases to ~25 % and ~10 % at substrate temperature of 300 °C and 500 °C, respectively and the film becomes nearly free from sp^3 bonded carbon atoms at the deposition temperature of 750 °C.

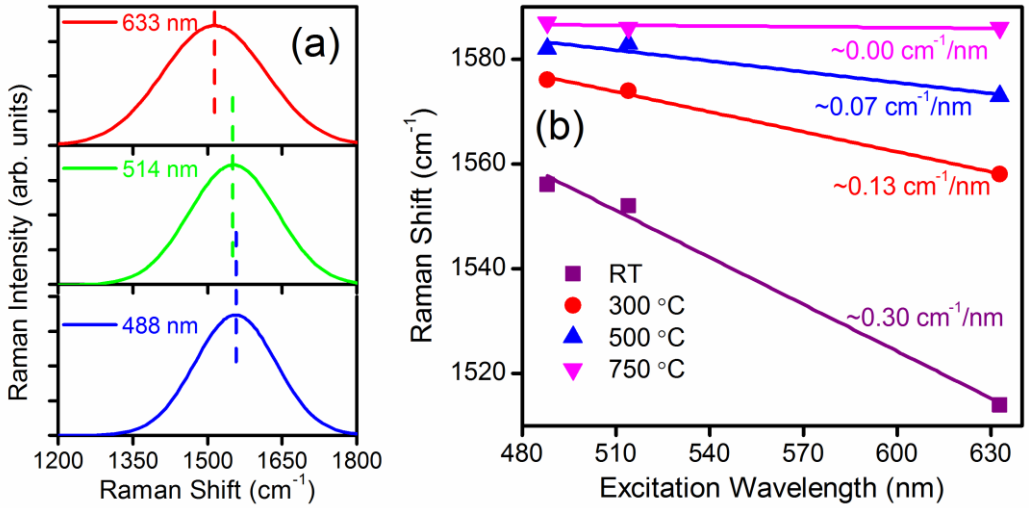

Figure 4.5: (a) *Dispersion of G band for film deposited at RT and* ***(b)*** *Dispersion rate of G band for films deposited at RT, 300 °C, 500 °C and 750 °C.*

Apart from D and G bands, there is another Raman band positioned at ~1200 cm^{-1}, *Figure 4.2*, corresponding to a transverse vibration mode of sp^3 carbon atoms in a chain configuration due to the interfacing of amorphous carbon matrix of olefin sp^3 sites bonded to the diamond crystallites [**33**]. Another band in the range of 1450-1490 cm^{-1} evolved in the films deposited at higher temperatures (300 °C and above) only which may originate from olefin sp^2-sp^3 carbon bonds at the edges of diamond-like structures [**33**]. At substrate temperature of 750 °C, the dominating sites are sp^2, thus there is a reduction in the intensity of this band, as shown in *Figure 4.2 (d)*. An additional Raman band at ~1614 cm^{-1} (D' band) is also observed for the film deposited at 750 °C. This band appears due to the formation of microcrystalline graphite, further confirming that the film is enriched in sp^2 bonds at high deposition temperatures [**34**].

4.2.1.2 Spectroscopic ellipsometric study for linear optical properties of DLC films as a function of deposition temperature

In order to study the effect of substrate temperature on the optical properties, the films were subjected to the ellipsometric measurements. Ellipsometer measures the change in polarization of the reflected light w.r.t. the incident light. The measured data were converted into the spectra of refractive index (*n*) and extinction coefficient (*k*) to study the optical properties of carbon films. These *n* and *k* spectra contain the substrate effect and are called pseudo *n* and *k*. An approximated dispersion model is required to extract the information of deposited film from pseudo *n* and *k*. For amorphous materials, the dispersion model was proposed by Forouhi and Bloomer by assuming the parabolic conduction and valence bands with no allowed electronic states in between them [**35**]. As DLC films are amorphous in nature, there is a possibility of the existence of allowed states within the Forouhi-Bloomer (FB) energy gap. McGahan et al. modified the FB model for amorphous hydrogenated carbon films and calculated refractive index, *n(E)*, as a function of energy, *E*, numerically [**36**]. FB model was further modified by Yong Liu et al. to describe the dispersion of the optical constants of a-Si thin films by considering the non-parabolic conduction and valence bands [**37**]. In modified FB (mFB) model, the refractive index and extinction coefficient are given by *Equation (4.2) and (4.3)*, respectively [**37**].

$$n(E) = n(\infty) + \frac{(-B_0 D - 2C_0)E + 2B_0 F + C_0 D}{E(E - D) + F} \tag{4.2}$$

$$k(E) = \frac{A + B(E - E_g) + C(E - E_g)^2}{E(E - D) + F} \tag{4.3}$$

where,

$$B_0 = \frac{(B - 2CE_g + CD)}{Q}$$

$$C_0 = \frac{(A - BE_g + CE_g^2 - CF)}{Q}$$

$$Q = \sqrt{4F - D^2}$$

A, *B*, *C*, *D* and *F* are constants, while $4F - D^2 > 0$. *n(∞)* is the refractive index at infinite photon energy, *E* is photon energy and E_g corresponds to the optical band gap. *Figure 4.6 (a) and (b)* shows the mFB fit for pseudo refractive index and extinction coefficient, respectively, for carbon films deposited at RT, 300 °C, 500 °C and 750 °C. The refractive index and extinction coefficient of carbon films at a wavelength of 633 nm and the optical band gap obtained by the calculation of spectroscopic ellipsometric (SE) measurement results are listed in *Table 4.2* as a function of substrate temperature.

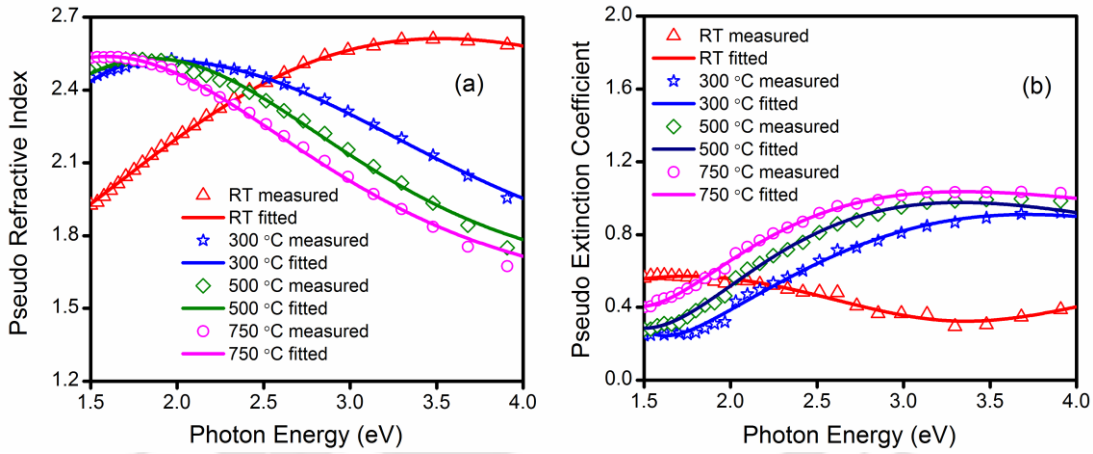

Figure 4.6: *mFB fit for* ***(a)*** *pseudo refractive index and* ***(b)*** *pseudo extinction coefficient for films deposited at RT, 300 °C, 500 °C and 750 °C.*

Table 4.2: *Refractive index, extinction coefficient and optical band gap of carbon thin films as a function of substrate temperature*

Substrate temperature	Refractive index	Extinction coefficient	Band gap (eV)
RT	2.29	0.16	1.62
300 °C	3.32	1.29	1.09
500 °C	3.74	1.58	1.03
750 °C	3.61	1.69	0.96

In amorphous carbon films, the sp^2 sites segregates into clusters within sp^3 matrix. The sp^2 fraction and arrangements of sp^2 sites influence the optical band gap. Since π-states of sp^2 sites lie closer to the Fermi level and the optical band gap varies in inverse proportion to the sp^2 cluster size. For the film deposited at RT, the size of sp^2 cluster embedded in sp^3 matrix is small, *Figure 4.4 (b)*, resulting in the widening of π-π^* gap and the corresponding optical band gap was found to be 1.62 eV. The optical band gap was found to be decreasing with the increase in deposition temperature which is due to the increase in sp^2 cluster size.

The increase in sp^2 cluster size changes the bond strength and bond orientation in the arrangements of carbon atoms leading to the change in charge distribution which influences the polarizability. According to the Clausius-Mossotti relation, the polarizability is related to the dielectric constant and hence to the refractive index. In case of homopolar semiconductors (i.e. C, Si, Ge, Sn), the dielectric constant (thus also the refractive index, $n = \sqrt{\varepsilon}$) is related to the optical band gap energy (E_g) according to the *Equation (4.4)* [**38, 39**].

$$\varepsilon = 1 + \left(\frac{E_p}{E_g} \right)^2 \qquad (4.4)$$

where, E_p is the energy corresponding to the plasma frequency for carbon. *Equation (4.4)* indicates that the refractive index will increase with the decrease in band gap, as also observed in *Table 4.2*. The increase in refractive index with decreasing band gap is due to increase in microscopic bond polarizability as a result of increase in π-states with the increase in substrate temperature.

The extinction coefficient, *k*, for the film deposited at RT was found to be 0.16. The low *k*-value indicates that the film consists of predominantly sp^3 bonded carbon atoms, as also obtained from Raman spectra. The increase in substrate temperature

favours the formation of sp^2 clusters which provides more π-states and leads to the increase in absorption in the visible range. This results in the increase in *k*-value with the substrate temperature and reaches a maximum value of 1.69 for the film deposited at the substrate temperature of 750 °C.

4.2.2 Effect of laser fluence on PLD-DLC thin films

In the previous section 4.2.1, it was observed that film deposited at RT was rich in sp^3 bonded carbon atoms. Therefore, to study the effect of laser fluence on the sp^3 content, PLD DLC films were deposited on corning glass and silicon (undoped) substrate at RT for a duration of 30 min at various laser fluences; 5.0 J/cm^2, 6.7 J/cm^2, 8.3 J/cm^2, 10.0 J/cm^2 and 11.7 J/cm^2. The other parameters were kept constant as listed in *Table 4.1*.

4.2.2.1 Raman spectra of DLC thin films as a function of laser fluence

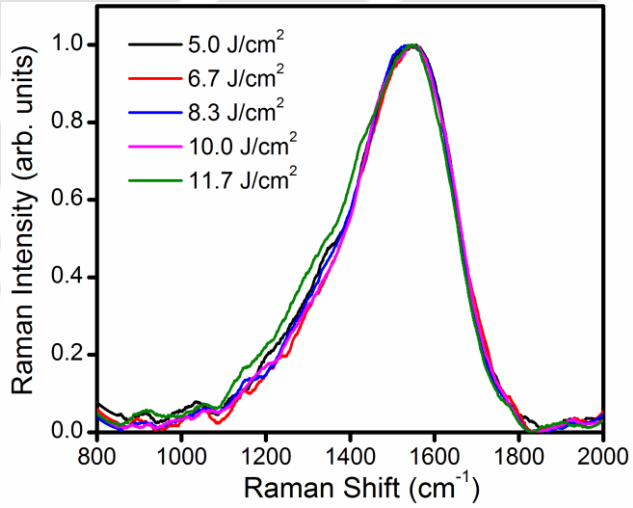

Figure 4.7: *Raman spectra of DLC thin films deposited at RT as a function of laser fluence.*

The Raman spectra of DLC thin films, recorded using micro-Raman spectrometer with excitation laser wavelength of 514 nm are shown in *Figure 4.7*. All these samples exhibited a broad band around ~1550 cm^{-1} having long tail towards the lower

wavenumber, indicating the signature of higher sp^3 fraction in these films [**26**]. *Figure 4.8* shows the deconvoluted Raman spectra of DLC film deposited at a laser fluence of 5.0 J/cm^2, only as an example, exhibiting G band, D band, Band-3 and peak sum. The peak positions of G and D band, I_D/I_G ratio and sp^3 fraction are listed in *Table 4.3*. Since the visible laser wavelength excites only sp^2 sites, there is a marginal difference in the peak position of G and D bands for all samples [**40**]. The I_D/I_G ratio of the film deposited at the laser fluence of 8.3 J/cm^2 shows the minimum value but the difference in all the samples is small. The low value of I_D/I_G is a signature of higher sp^3/sp^2 fraction in the DLC thin film.

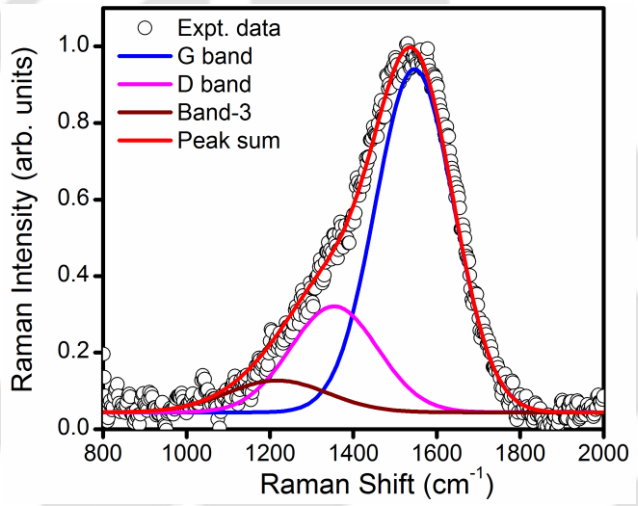

Figure 4.8: *Deconvoluted Raman spectra of DLC thin film deposited at a laser fluence of 5.0 J/cm^2.*

Table 4.3: *Raman band parameters of DLC thin films as a function of laser fluence*

Laser fluence (J/cm^2)	**Position of G band (cm^{-1})**	**Position of D band (cm^{-1})**	**I_D/I_G**	**sp^3 (%)**
5.0	1548	1353	0.34	71
6.7	1546	1362	0.31	73
8.3	1545	1351	0.26	78
10.0	1546	1359	0.30	76
11.7	1543	1362	0.35	76

The dispersion of G band for all the films are shown in *Figure 4.9* and the estimated sp^3 *(%)* is listed in *Table 4.3*. All the samples possess sp^3 rich carbon bonding as its content is above 70%.

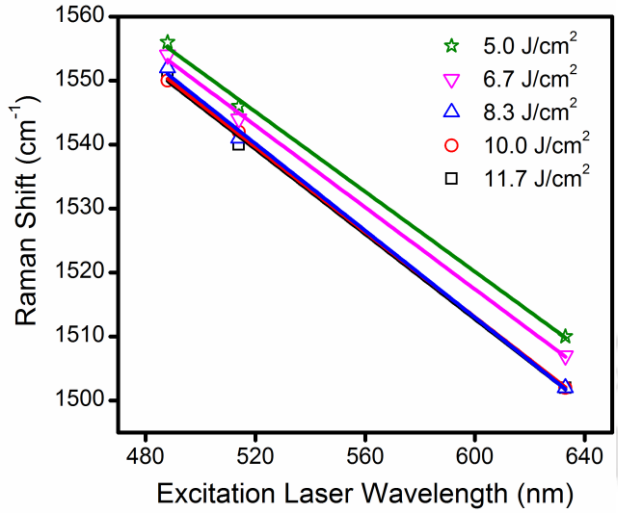

Figure 4.9: *Dispersion rate of G band for DLC thin films deposited at RT and laser fluence of 5.0 J/cm^2, 6.7 J/cm^2, 8.3 J/cm^2, 10.0 J/cm^2 and 11.7 J/cm^2.*

The increase in laser fluence from 5.0 J/cm^2 to 8.3 J/cm^2 produces the plasma species with higher kinetic energy and promotes the formation of sp^3 bonded carbon atoms and hence there is a slight increase in sp^3 content in the film. On further increase in laser fluence, the sp^3 fraction decreased slightly. The carbon adatoms diffuse over the film surface with the excessive kinetic energy and favours the formation of sp^2 bonding.

4.2.2.2 FTIR spectra of DLC thin films as a function of laser fluence

FTIR spectra of DLC thin films were recorded to observe the presence of hydrogen in the film. For this, DLC films were deposited onto undoped silicon wafer. The spectra were recorded using FTIR spectrometer in the range of 500 - 4000 cm^{-1} and shown in *Figure 4.10*. In IR spectra, a broad band was observed below 2000 cm^{-1}, which is attributed to the stretching mode of sp^2 bonded carbon atoms [**41**]. The large transmission (low absorption) in this region indicates that all the films contain small

fraction of sp^2. The absence of clear signature of band around 3000 cm^{-1} indicates that PLD DLC films are nearly free from hydrogen.

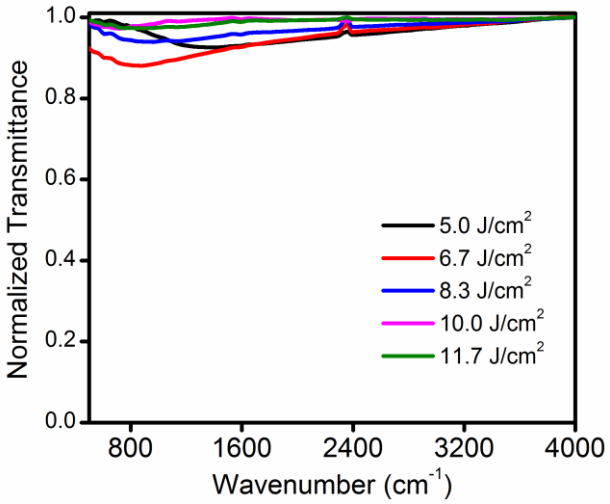

Figure 4.10: *FTIR transmission spectra for DLC thin films deposited at RT and laser fluence of 5.0 J/cm^2, 6.7 J/cm^2, 8.3 J/cm^2, 10.0 J/cm^2 and 11.7 J/cm^2.*

4.2.2.3 Optical constants of DLC thin films as a function of laser fluence via spectroscopic ellipsometry

The pseudo refractive index and extinction coefficient as a function of photon energy fitted to mFB dispersion relation, *Equation (4.2)* and *(4.3)*, respectively, are shown in *Figure 4.11*.

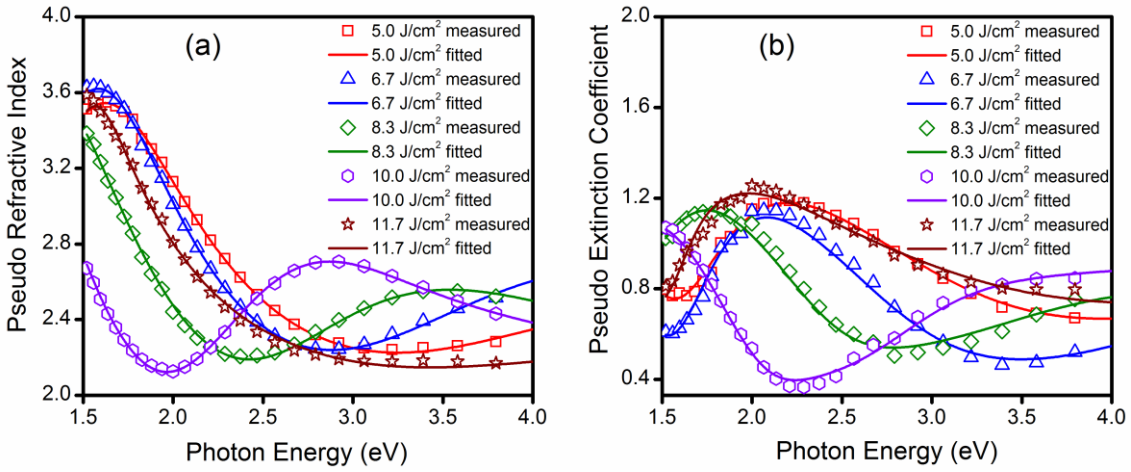

Figure 4.11: *mFB fit for **(a)** pseudo refractive index and **(b)** pseudo extinction coefficient for DLC thin films deposited at RT as a function of laser fluence.*

Table 4.4 lists the optical constants for all these samples obtained using mFB model as a function of laser fluence. The thickness of the film was increased from 67 nm to 119 nm for the film deposited at the laser fluence of 5.0 J/cm^2 to 10.0 J/cm^2, respectively. The increase in laser fluence increases the ablation from the graphite target and provides the higher flux of plasma species arriving at the substrate surface which leads to the increase in film thickness. The further increase in laser fluence to 11.7 J/cm^2 causes the plasma species to strike the substrate surface with extremely high kinetic energy and sputtered back, resulting into slight decrease in film thickness. The refractive index, extinction coefficient and optical band gap for all the samples show the values with marginal difference indicating that all films are of nearly similar structure as also confirmed by Raman spectra, *Table 4.3*.

Table 4.4: *Thickness, band gap, refractive index and extinction coefficient of DLC thin films as a function of laser fluence*

Laser fluence (J/cm^2)	**Thickness (nm)**	**Band gap (eV)**	**Refractive index**	**Extinction coefficient**
5.0	67	0.86	2.73	0.37
6.7	76	1.06	2.68	0.25
8.3	96	1.12	2.57	0.25
10.0	119	1.11	2.57	0.29
11.7	113	0.83	2.19	0.39

4.2.2.4 Optical band gap using UV-Visible-NIR transmission spectra

The transmission spectra of DLC thin films deposited at RT on corning glass substrate, recorded using Ellipsometer, are shown in *Figure 4.12*. The transmission spectra showed hardly any significant dependence on the laser fluence for DLC thin films deposited in this range of laser fluence. The films exhibited high transmission in near-infrared (NIR) region. The maximum absorption is observed around ~270 nm for all

the samples. The absorption edge at ~270 nm is due to π-π* transitions of carbon atoms. The transmission curves for all the films showed broad absorption band in the range of 250-600 nm and above 600 nm the transmittance increased continuously to a maximum of 70-75% with the increase in wavelength upto 1600 nm. The broad absorption band is due to the presence of sp^2 bonds of carbon atoms having low band gap.

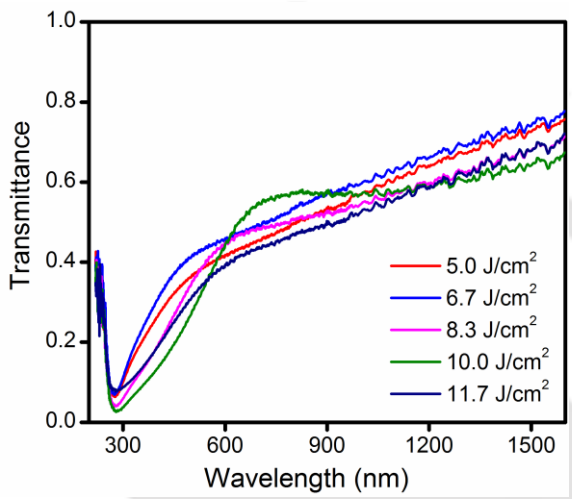

Figure 4.12: *Transmission spectra of DLC thin films deposited at RT as a function of laser fluence of 5.0 J/cm^2, 6.7 J/cm^2, 8.3 J/cm^2, 10.0 J/cm^2 and 11.7 J/cm^2.*

As DLC thin film is amorphous in nature, it exhibits indirect band gap which is related to the absorption coefficient given by *Equation (4.5)*.

$$(\alpha h\upsilon)^{1/2} = B(h\upsilon - E_g) \tag{4.5}$$

where, 'B' is a constant, '$h\nu$' is the photon energy, 'E_g' is the optical band gap energy and 'α' is the linear absorption coefficient which can be determined from transmission spectrum using Beer-Lambert law, *Equation (4.6)*.

$$\alpha(\upsilon) = \frac{\ln(1/T)}{d} \tag{4.6}$$

where, 'T' is the optical transmittance and 'd' is the film thickness. The plot of $(\alpha h\nu)^{1/2}$ vs. $h\nu$ provide the optical band gap, as shown in *Figure 4.13*. The intercept of the extrapolated linear region of the Tauc plot curve on '$h\nu$' axis measures the optical band

gap of the film. The variation of optical band gap as a function of laser fluence is listed in *Table 4.5*.

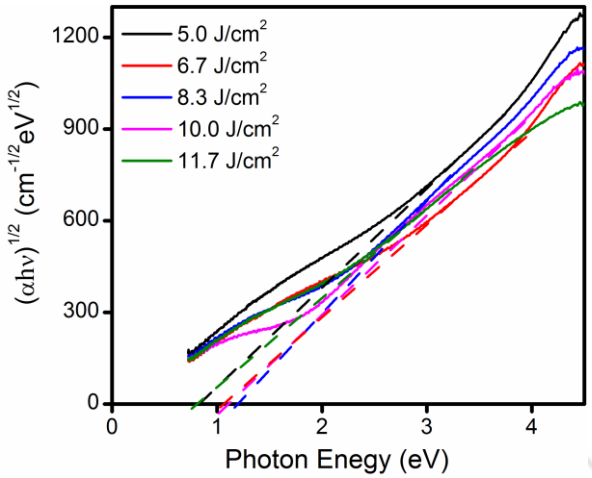

Figure 4.13: *Tauc plot for DLC thin films deposited at RT and laser fluence of 5.0 J/cm^2, 6.7 J/cm^2, 8.3 J/cm^2, 10.0 J/cm^2 and 11.7 J/cm^2.*

Table 4.5: *Tauc gap of DLC thin films as a function of laser fluence*

Laser fluence (J/cm^2)	5.0	6.7	8.3	10.0	11.7
Band gap (eV)	0.84	1.00	1.20	1.10	0.80

A comparison of optical band gap obtained from Tauc plot and that of obtained from mFB model is shown in *Figure 4.14* and observed to be following the similar trend in both the cases.

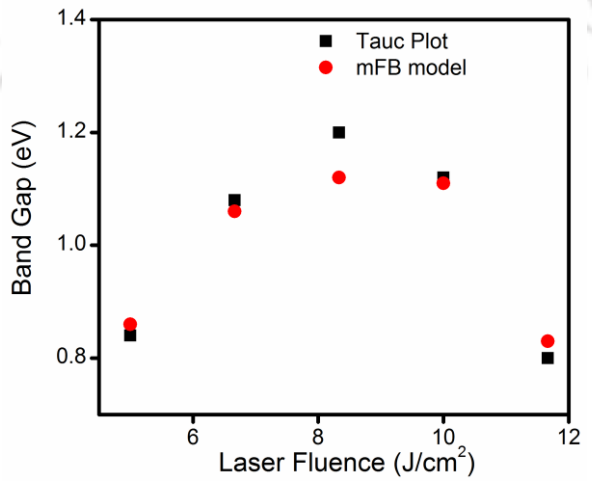

Figure 4.14: *Comparison of Tauc energy gap and mFB energy gap for DLC thin films as a function of laser fluence.*

4.2.3 Effect of helium gas pressure on PLD-DLC thin films

In *section 4.2.2*, the effect of laser fluence on the DLC thin films in background pressure of ~10^{-5} mbar is studied where hardly any significant effect on the sp^3 fraction in the film was observed. But, at higher laser fluence the ejection of large particulates from the target was observed and getting deposited onto the substrate directly. To overcome this problem, helium gas was introduced as background gas in the ablation chamber during deposition of the film. The DLC thin films were deposited under the helium pressures; 0.05 mbar, 0.1 mbar, 0.5 mbar and 1 mbar and at each pressure, the films were also deposited at four laser fluences; 10.0 J/cm^2, 11.7 J/cm^2, 13.3 J/cm^2 and 15.0 J/cm^2. The DLC thin films were deposited for 30 min on corning glass substrate while keeping other deposition parameters fixed, as detailed in *Table 4.1*.

4.2.3.1 Structural characterization using Raman spectroscopy of PLD-DLC films as function of helium pressure

The Raman spectra of DLC thin films were recorded using 514 nm of Argon ion laser as an excitation source. The Raman spectra of films deposited at 0.05 mbar and 0.1 mbar of helium pressure are observed to be similar irrespective of the laser fluence, as shown in *Figure 4.15 (a) and (b)*, respectively. The films deposited at the 0.5 mbar (for laser fluence of 10.0 J/cm^2 and 11.7 J/cm^2 only) and 1 mbar of helium pressure (for all fluences) displayed poor Raman response as shown in *Figure 4.15 (c) and (d)*, respectively, probably because of very less thickness, high transparency and low signal to noise ratio. At 0.5 mbar, film deposited at a laser fluence of 15.0 J/cm^2 showed Raman spectra with high signal to noise ratio as compared to that of films deposited at lower laser fluences and therefore, films deposited at a laser fluence of 15.0 J/cm^2 were selected to study the effect of helium pressure on sp^3/sp^2 ratio of carbon bonding.

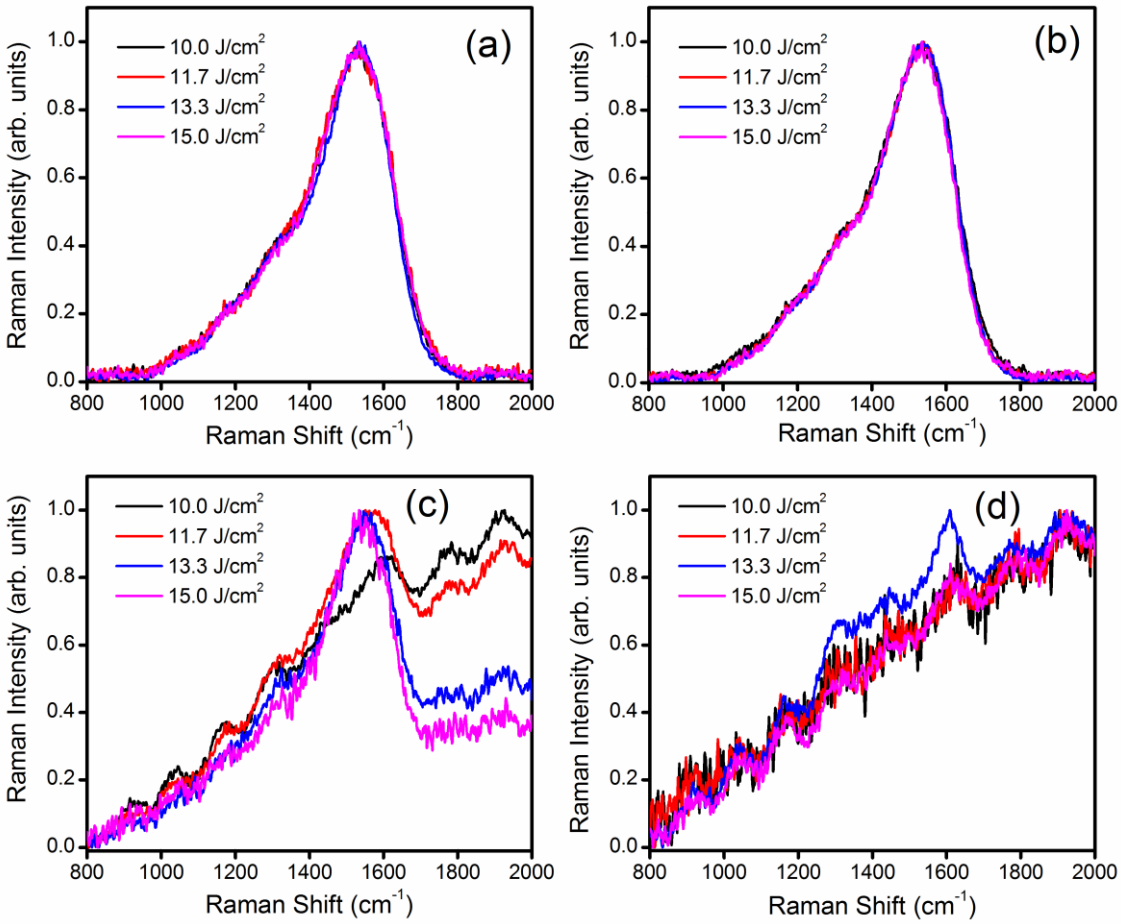

Figure 4.15: *Raman spectra of DLC thin films deposited at laser fluence of 10.0 J/cm^2, 11.7 J/cm^2, 13.3 J/cm^2 and 15.0 J/cm^2 and helium pressure of* ***(a)*** *0.05 mbar,* ***(b)*** *0.1 mbar,* ***(c)*** *0.5 mbar and* ***(d)*** *1 mbar.*

Figure 4.16 (a-c) shows the deconvoluted Raman spectra into three Gaussian components; centred at ~1540 cm^{-1} (G band), ~1350 cm^{-1} (D band) and ~1150 cm^{-1} for DLC film deposited at laser fluence of 15.0 J/cm^2 and helium gas pressure of 0.05 mbar, 0.1 mbar and 0.5 mbar, respectively. The spectra showed a Raman band centred at ~1550 cm^{-1} along with an asymmetric broadening towards the lower wavenumber, which is a signature of DLC [**26**]. The G band shifts to lower wavenumber from 1542 cm^{-1} to 1535 cm^{-1} with the increase in ambient gas pressure from 0.05 mbar to 0.5 mbar. The I_D/I_G ratio was observed to be 0.41, 0.39 and 0.27 for films deposited at helium gas pressure of 0.05, 0.1 and 0.5 mbar, respectively. The decrease in I_D/I_G ratio and the shifting of G

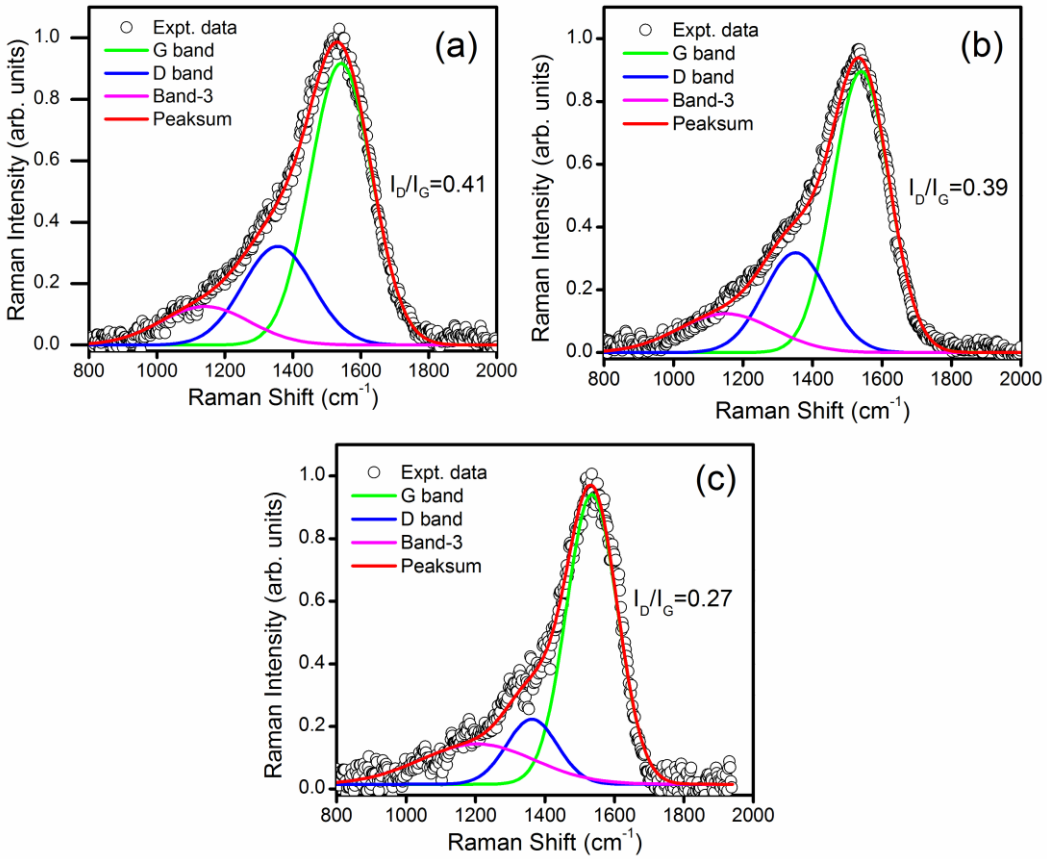

***Figure 4.16**: Deconvoluted Raman spectra of DLC thin films deposited at a laser fluence of 15.0 J/cm^2 as a function of helium pressure **(a)** 0.05 mbar, **(b)** 0.1 mbar and **(c)** 0.5 mbar.*

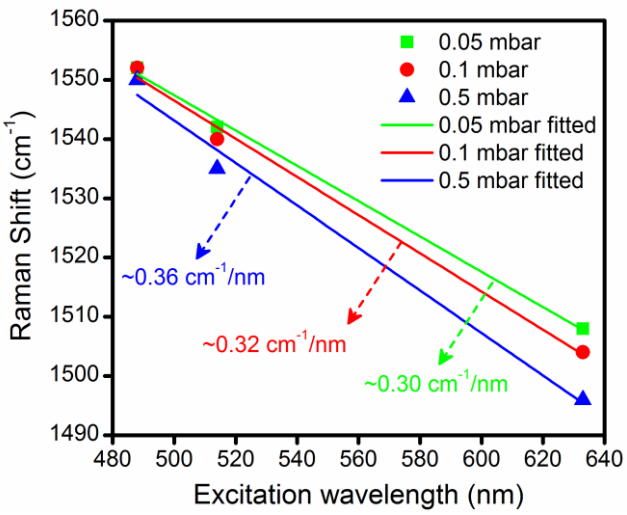

***Figure 4.17:** Dispersion rate of G band for DLC thin films deposited at a laser fluence of 15.0 J/cm^2 and helium pressure of 0.05mbar, 0.1 mbar and 0.5 mbar.*

band to lower wavenumber indicate the decrease in graphite-like phase and hence the film became more diamond-like with the increase in helium pressure. The higher fraction

of sp^3 bonds of carbon atoms was also confirmed by the dispersion of G band using *Equation (1.1), Chapter 1*. The dispersion of G band is shown in *Figure 4.17* and was observed to increase with the increase in helium pressure. The corresponding sp^3 content in the film deposited at 0.05 mbar of helium pressure was ~68 % which increases to ~73 % and ~83 % for the films deposited at helium pressure of 0.1 mbar and 0.5 mbar, respectively.

Apart from D and G bands, another peak appeared at ~1150 cm^{-1} (Band-3) in DLC thin films due to the presence of microcrystalline diamond or amorphous diamond within amorphous carbon matrix [**31, 42**].

4.2.3.2 Linear optical parameters using spectroscopic ellipsometry for PLD-DLC films as a function of helium pressure

Figure 4.18 (a-b) shows the mFB fit for pseudo refractive index and extinction coefficient of DLC thin films deposited at a laser fluence of 15.0 J/cm^2 and helium pressure ranging 0.05 - 1 mbar. For the films deposited at 0.05 mbar and 0.1 mbar of helium pressure, the values of *k* are slightly large in the visible range as compared to that

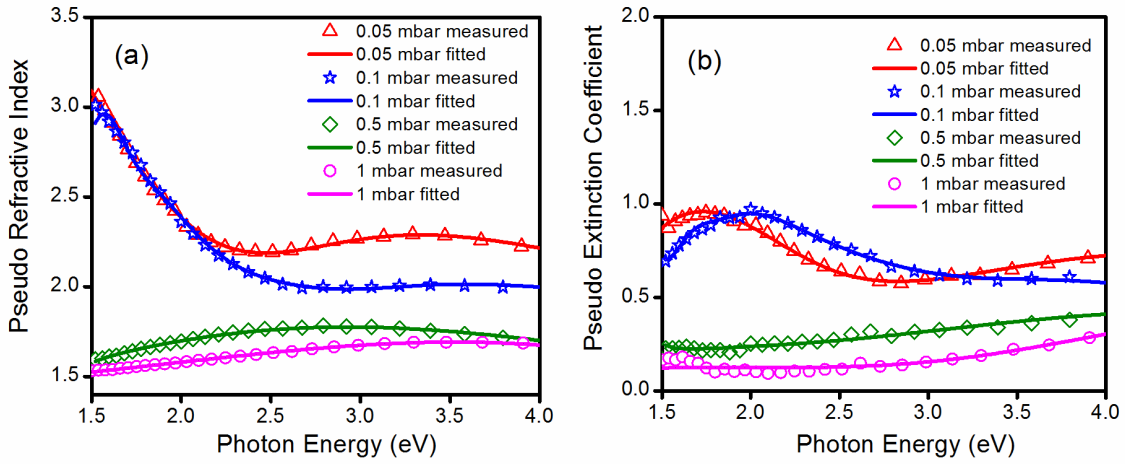

Figure 4.18: *mFB fit for* ***(a)*** *pseudo refractive index and* ***(b)*** *pseudo extinction coefficient for DLC thin films deposited at a laser fluence of 15.0 J/cm^2 and helium pressure of 0.05 mbar, 0.1 mbar, 0.5 mbar and 1 mbar.*

of in UV region indicating more $\pi - \pi^*$ transitions involved and hence low fraction of sp^3 bonding of carbon, in confirmation with the Raman spectra (*section 4.2.3.1*). With the increase in gas pressure further to 0.5 mbar and 1 mbar, the extinction coefficient showed the increasing trend from visible to UV range which is the evidence of increase in $\sigma - \sigma^*$ electronic transitions and hence sp^3 carbon bonding. The estimated thickness and optical band gap energy of DLC films obtained using mFB dispersion relation, *Equation (4.2)* and *(4.3)*, as a function of laser fluence and helium gas pressure, are listed in *Table 4.6* and *Table 4.7*, respectively.

Table 4.6: *Thickness of DLC thin films as a function of deposition condition*

Laser fluence → **Helium pressure ↓**	**Thickness (nm)**			
	10.0 J/cm^2	**11.7 J/cm^2**	**13.3 J/cm^2**	**15.0 J/cm^2**
0.05 mbar	121	140	120	107
0.1 mbar	138	189	207	220
0.5 mbar	20	38	36	44
1 mbar	14	16	30	34

The thickness of DLC thin films showed non-monotonous behaviour with the deposition conditions. For the film deposited at helium pressure of 0.05 mbar, the thickness was found to increase from 121 nm to 140 nm for the laser fluence of 10.0 J /cm^2 and 11.7 J/cm^2, respectively, which is due to the increase in ablated mass at the higher laser fluence. The further increase in laser fluence decreased the film thickness to 120 nm and 107 nm at laser fluence of 13.3 J/cm^2 and 15.0 J/cm^2, respectively. The decrease in film thickness at these laser fluences for the helium gas pressure of 0.05 mbar is due to sputtering back of the carbon species from the substrate as a result of increased incident energy of those species. For the helium gas pressure of 0.1 mbar, 0.5 mbar and 1 mbar, the film thickness was found be increased with the increase in the laser

fluence. At higher pressure of helium gas, the kinetic energy of the particles impinging on the substrate reduced due to the enhanced collisional process and hence all the particles get attached without being bounced back at higher laser fluence resulting in increase in film thickness. For any given laser fluence, the film thickness was found to be increased with the increase in gas pressure from 0.05 mbar to 0.1 mbar which is due to the increase in flux density of the carbon species as a result of the confinement of expanding laser produced plasma (LPP). With the further increase in the gas pressure to 0.5 mbar and 1 mbar, due to the excessive confinement of the plasma the number of carbon species reaching to the substrate decreases resulting into the decrease in film thickness.

The band gap energy of DLC thin films was observed to be increasing with the helium pressure irrespective of the laser fluence. It was less than 2 eV at 0.05 mbar and was in the range of 3.13 - 3.47 eV at 1 mbar, *Table 4.7*. The variation in optical band gap as a function of laser fluence was less pronounced compared to that of helium pressure. The increase in the band gap is associated with the increase in sp^3/sp^2 ratio in the film. The increase in sp^3/sp^2 ratio with the helium pressure is also indicated by the Raman spectra. Films deposited at the helium pressure of 0.5 and 1 mbar exhibited high transparency which is in accordance with the large value of band gap (*Figure 4.19*).

Table 4.7: *Band gap of DLC thin films as a function of deposition condition*

Laser fluence → **Helium pressure ↓**	**Band gap (eV)**			
	10.0 J/cm^2	**11.7 J/cm^2**	**13.3 J/cm^2**	**15.0 J/cm^2**
0.05 mbar	1.21	1.33	1.42	1.43
0.1 mbar	2.01	1.75	1.84	1.83
0.5 mbar	2.43	2.72	2.95	3.03
1 mbar	3.13	3.23	3.47	3.42

The refractive indices of DLC thin films obtained from ellipsometric measurements are listed in *Table 4.8* at a wavelength of 633 nm. The values were found to be decreasing with the helium pressure. The dependence of refractive index on the laser fluence and helium pressure can be attributed to the variation in the bonding of carbon atoms. The bond strength and bond orientation in the arrangement of carbon atoms depend on sp^3/sp^2 fraction in DLC films. The increase in sp^3 fraction in the DLC film reduces the microscopic bond polarizability due to the decrease in bond length and bond angle leading to decrease in refractive index. This is consistent with the increase in sp^3 content in the DLC films with the increase in helium pressure as also confirmed by Raman spectra.

Table 4.8: *Refractive index of DLC thin films at λ=633 nm as a function deposition condition*

Laser fluence → **Helium pressure ↓**	**Refractive index**			
	10.0 J/cm^2	**11.7 J/cm^2**	**13.3 J/cm^2**	**15.0 J/cm^2**
0.05 mbar	2.83	2.59	2.26	2.30
0.1 mbar	2.41	2.39	2.52	2.54
0.5 mbar	2.09	1.83	2.31	1.95
1 mbar	1.97	1.95	1.67	1.67

The extinction coefficient for DLC thin films at 633 nm as obtained from ellipsometric measurements as a function of laser fluence and helium gas pressure is listed in Table 4.9. The value of $k<1$ for all the films indicating that the films are predominantly consisting of sp^3 carbon bonds **[43, 44]**. The extinction coefficient value of the films deposited at helium pressure of 0.1 mbar is comparatively larger which may be due to the increased film thickness, Table 4.6. The films deposited at 1 mbar at all the four laser fluences have minimum extinction coefficient value. Since the value of extinction coefficient is related to the structural characteristic of films, DLC thin films fabricated at 1 mbar of helium gas pressure are more diamond-like.

Table 4.9: *Extinction coefficient of DLC thin films at λ=633 nm as a function of deposition condition*

Laser fluence → Helium pressure ↓	**Extinction coefficient**			
	10.0 J/cm^2	**11.7 J/cm^2**	**13.3 J/cm^2**	**15.0 J/cm^2**
0.05 mbar	0.74	0.85	0.32	0.30
0.1 mbar	0.64	0.53	0.58	0.73
0.5 mbar	0.26	0.37	0.32	0.36
1 mbar	0.23	0.26	0.25	0.13

4.2.3.3. Transmission spectroscopy for optical band gap

The transmission spectra of the DLC thin films deposited on corning glass substrate, recorded using Ellipsometer, are shown in *Figure 4.19*. The films exhibited high transmission in IR and NIR region. The maximum absorption was observed at ~270 nm for all the samples, which corresponds to π-π* transition of carbon atoms. The transmission spectra for the films deposited at 0.05 and 0.1 mbar of helium gas pressure showed broad absorption band in the range of 250-700 nm and above 700 nm the transmission increased continuously to a maximum of 70-80% with the increase in

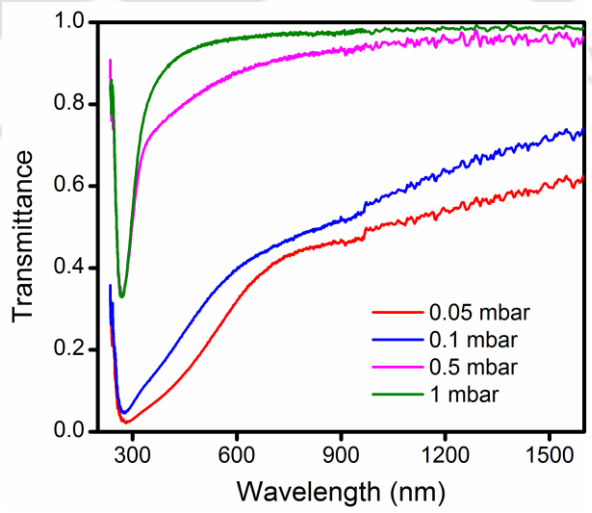

Figure 4.19: *Transmission spectra of DLC thin films deposited at a laser fluence of 15.0 J/cm^2 and helium pressure of 0.05 mbar, 0.1 mbar, 0.5 mbar and 1 mbar.*

wavelength upto 1600 nm. The broad absorption band is due to the presence of comparatively more sp^2 bonds of carbon atoms having low band gap and hence the films absorb light across the whole visible spectrum. The films deposited at 0.5 and 1 mbar of helium gas pressure, being very thin, are highly transparent in the region above 500 nm. The high transmission is due to low content of sp^2 bonded carbon atoms in DLC films deposited at 0.5 and 1 mbar.

The optical band gap of DLC thin films were also obtained from transmission spectra using Tauc plot as shown in *Figure 4.20*. The band gap variation as a function of helium pressure and laser fluence is listed in *Table 4.10*.

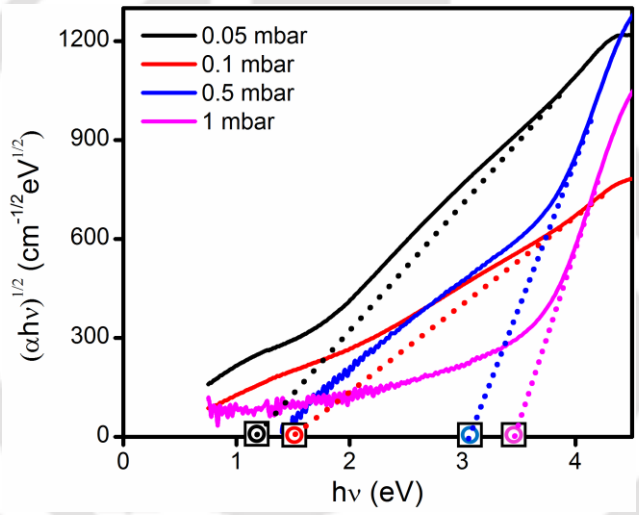

Figure 4.20: *Tauc plot for DLC thin films deposited at a laser fluence of 15.0 J/cm^2 and helium pressure of 0.05 mbar, 0.1 mbar, 0.5 mbar and 1 mbar.*

Table 4.10: *Tauc band gap of DLC thin films as a function of laser fluence and helium gas pressure*

Laser fluence → Helium pressure ↓	**Band gap (eV)**			
	10.0 J/cm^2	**11.7 J/cm^2**	**13.3 J/cm^2**	**15.0 J/cm^2**
0.05 mbar	1.20	1.39	1.25	1.17
0.1 mbar	1.56	1.39	1.40	1.53
0.5 mbar	3.15	2.97	3.12	3.06
1 mbar	3.20	3.28	3.29	3.45

The optical band gap obtained from Tauc plot was compared to that of obtained from mFB model and shown in *Figure 4.21*. The general trend of optical band gap w.r.t. to helium pressure and laser fluence in both cases is similar.

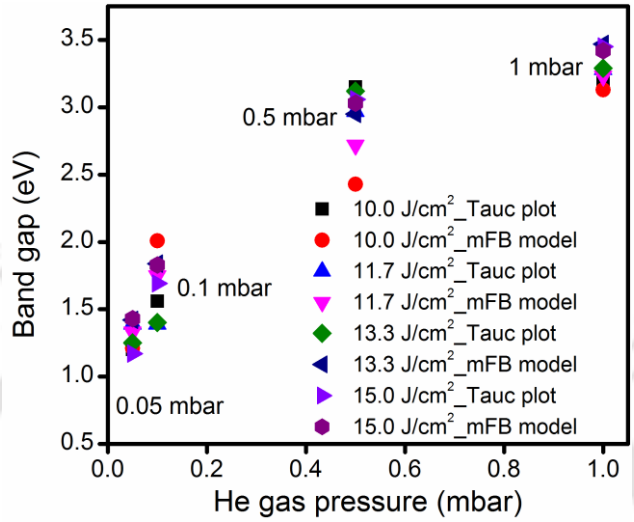

Figure 4.21: *Comparison of Tauc energy gap and mFB energy gap for DLC thin films deposited in helium ambient.*

4.2.3.4 Effect of laser fluence and helium pressure on the particle size distribution of PLD-DLC thin films

The AFM images (2 µm × 2 µm) of DLC thin films deposited on corning glass substrate at 1 mbar of helium pressure as a function of laser fluence ranging from 10.0 J/cm^2 to 15.0 J/cm^2 are shown in *Figure 4.22*. It clearly exhibited the formation of grain-like structure on the surface of DLC films. The particle density was observed to be increased with the increase in laser fluence. The particle size distribution and Gaussian fit onto it is shown in *Figure 4.23* as a function of laser fluence. At the laser fluence of 10.0 J/cm^2, the grain size was estimated to be 16 nm which was increased to 26 nm and 93 nm with the increase in laser fluence to 11.7 J/cm^2 and 13.3 J/cm^2, respectively. The increase in particle size is due to the increase in the density of LPP of graphite target at higher laser fluence which facilitates the coalescing of smaller sized particles to form

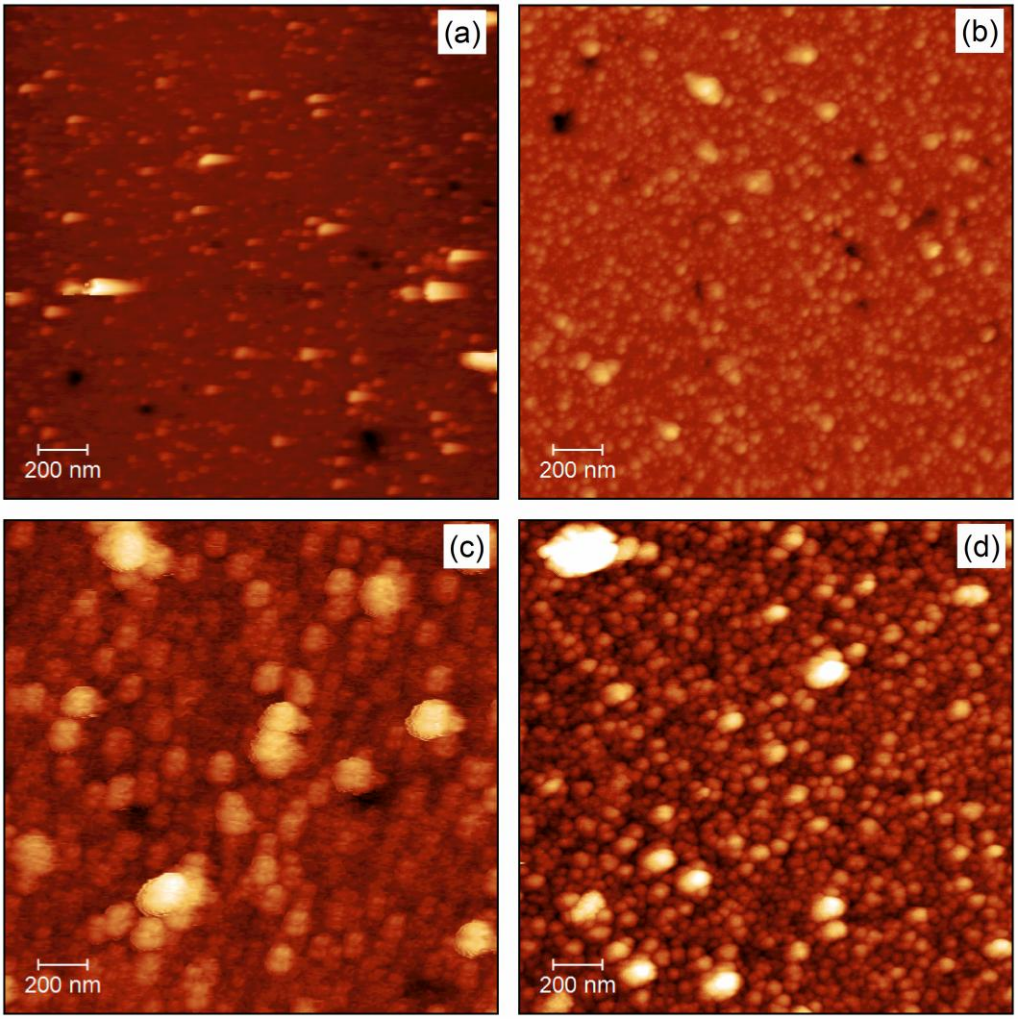

Figure 4.22: *Surface morphology of DLC thin films deposited at helium pressure of 1 mbar and laser fluence of* ***(a)*** *10.0 J/cm^2,* ***(b)*** *11.7 J/cm^2,* ***(c)*** *13.3 J/cm^2 and* ***(d)*** *15.0 J/cm^2.*

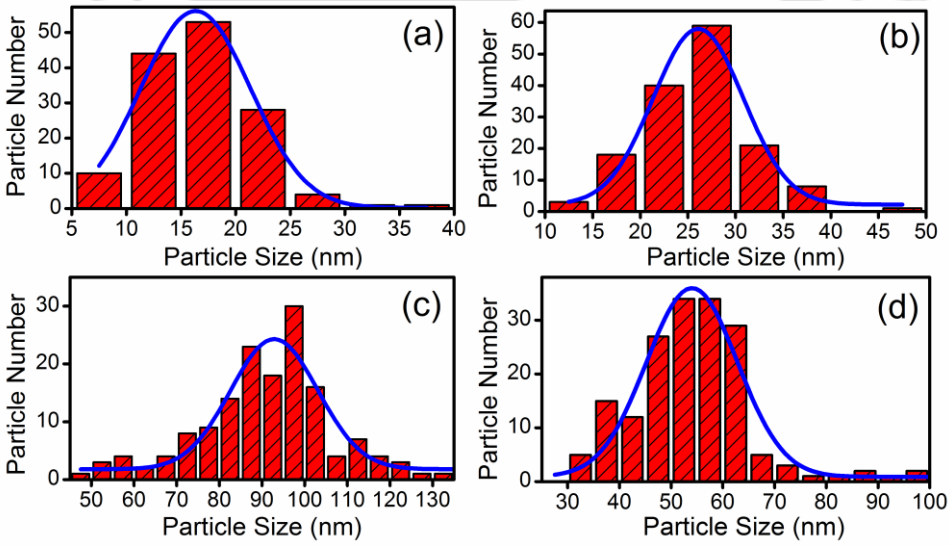

Figure 4.23: *Particle size distribution of DLC thin films deposited at helium pressure of 1 mbar and laser fluence of* ***(a)*** *10.0 J/cm^2,* ***(b)*** *11.7 J/cm^2,* ***(c)*** *13.3 J/cm^{2}and* ***(d)*** *15.0 J/cm^2.*

bigger particles. With further increase in laser fluence to 15.0 J/cm^2, while the density of the expanding plasma increases simultaneously there is an increase in the plasma temperature. Therefore particles strike on the substrate with higher kinetic energy and capable of fragmenting the already deposited particles into smaller sizes. This leads to the decrease in particle size to 54 nm for the film deposited at the laser fluence of 15.0 J/cm^2.

To study the effect of helium pressure on the surface morphology of DLC thin films, 2 µm × 2 µm AFM images of films deposited onto corning glass substrate at a laser fluence of 15.0 J/cm^2 are shown in *Figure 4.24* and corresponding particle size

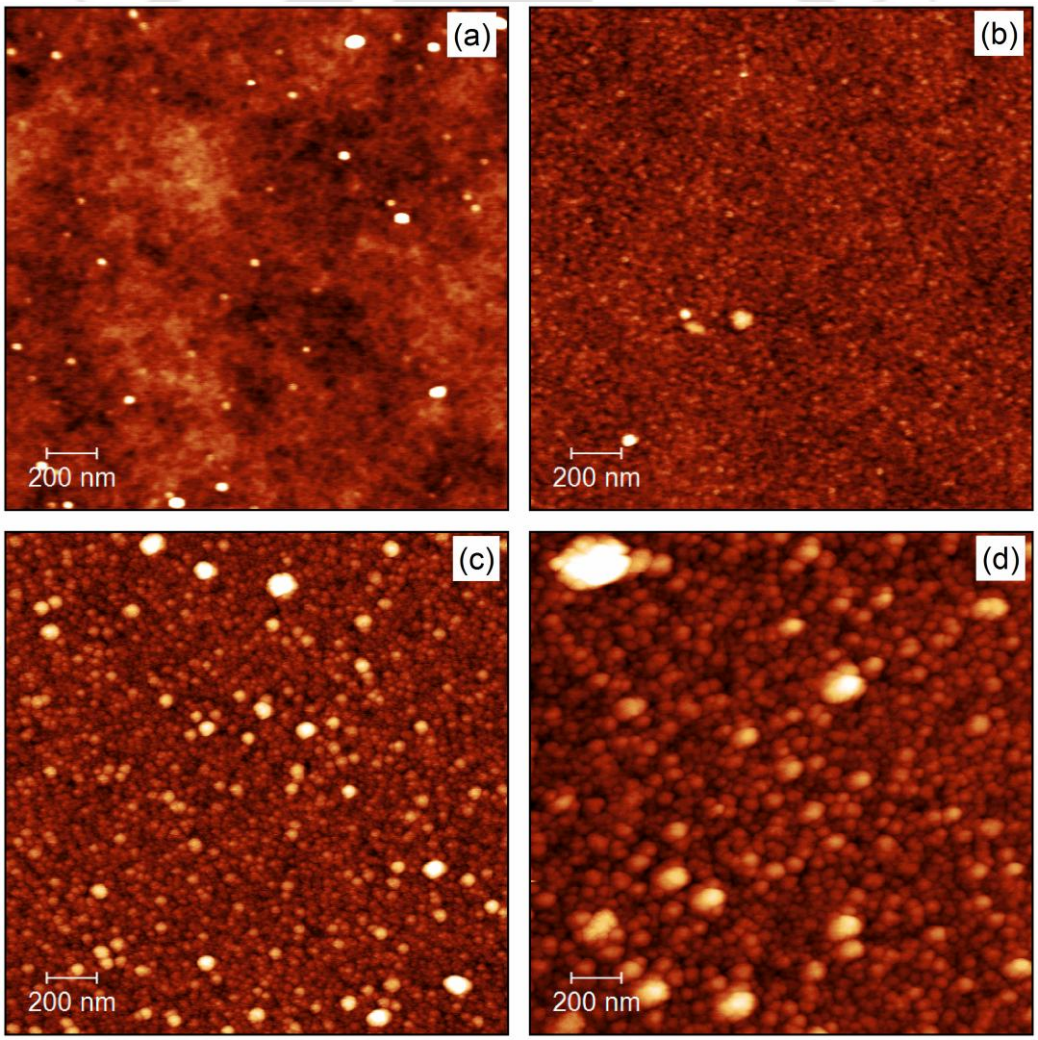

Figure 4.24: *Surface morphology of DLC thin films deposited at a laser fluence of 15.0 J/cm^2 and helium pressure of* ***(a)*** *0.05 mbar,* ***(b)*** *0.1 mbar,* ***(c)*** *0.5 mbar and* ***(d)*** *1 mbar.*

distribution is shown in *Figure 4.25*. The film deposited at a helium pressure of 0.05 mbar, the grain-like structure is thinly distributed, *Figure 4.24 (a)* and it was difficult to assess the particle size distribution for this film. At the helium pressure of 0.1 mbar, the average particle size was estimated to be 20 nm which was increased to 32 nm and 54 nm for the film deposited at 0.5 mbar and 1 mbar, respectively. With the increase in helium pressure, the expansion of the laser induced plasma is curtailed which increases the collisions between the plasma species and helium gas molecules. The increase in collisions reduces the kinetic energy of LPP species and simultaneously enhances the recombination rate due to higher plasma density which increases the density of adatoms on the surface thereby increasing the deposition of bigger sized grains.

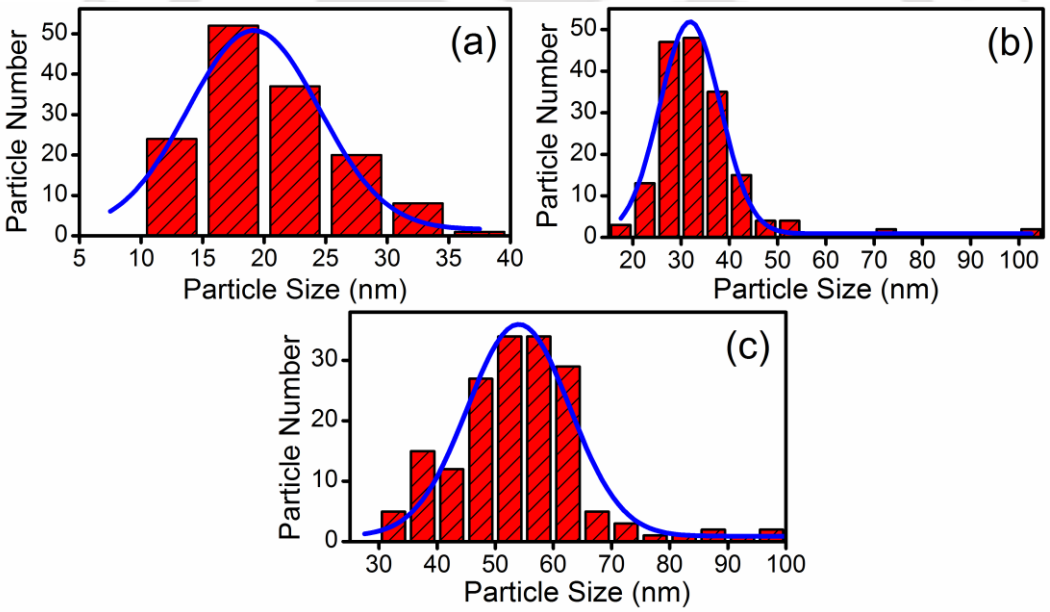

Figure 4.25: *Particle size distribution of DLC thin films deposited at a laser fluence of 15.0 J/cm^2 and helium pressure of* ***(a)*** *0.1 mbar,* ***(b)*** *0.5 mbar and* ***(c)*** *1 mbar.*

4.3 Fabrication of graphitic thin films

In the *section 4.2.1,* it was observed that the film deposited at 750 °C was rich in sp^2 carbon bonding and thus it is graphitic in nature. In this section, the effect of helium gas on the PLD graphitic thin films deposited at 750 °C is reported. All the films were

deposited on corning glass substrate. The other deposition parameters are listed in *Table 4.11*.

Table 4.11: *Deposition parameters for graphitic thin film fabrication*

Deposition temperature	750 ºC
Deposition time	5 min
Laser fluence	5.0 J/cm^2
Substrate	corning glass
Deposition pressure	10^{-5} mbar
	0.1 mbar helium
	1 mbar helium
	5 mbar helium
	10 mbar helium

4.3.1 Raman spectra of graphitic thin films as a function of helium pressure

The Raman spectra of PLD graphitic thin films were recorded using Ar-ion laser having excitation laser wavelength of 488 nm and shown in *Figure 4.26*. The appearance of distinct G and D bands in all the spectra reveal that the structure of film is dominated by sp^2 bonded carbon atoms. The films deposited at a base pressure of ~10^{-5} mbar and 0.1 mbar of helium pressure exhibit distinct but broad G and D bands, indicating that films are amorphous and has a signature of glassy carbon [**45**]. Glassy carbon is a partially graphitized form of carbon and composed of layers of graphite-like microcrystallites. The narrowing of D and G bands with the increase in helium pressure reveals the structural transition of the films from glassy carbon to graphitic. For detailed analysis, the Raman spectra were deconvoluted in the range of 800 cm^{-1} to 2000 cm^{-1} using the Gaussian and Lorentzian functions. Gaussian line arises from the random distribution of phonon lifetime of disordered materials and Lorentzian line represents the crystalline structure due to its finite lifetime broadening [**27**]. The deconvoluted Raman

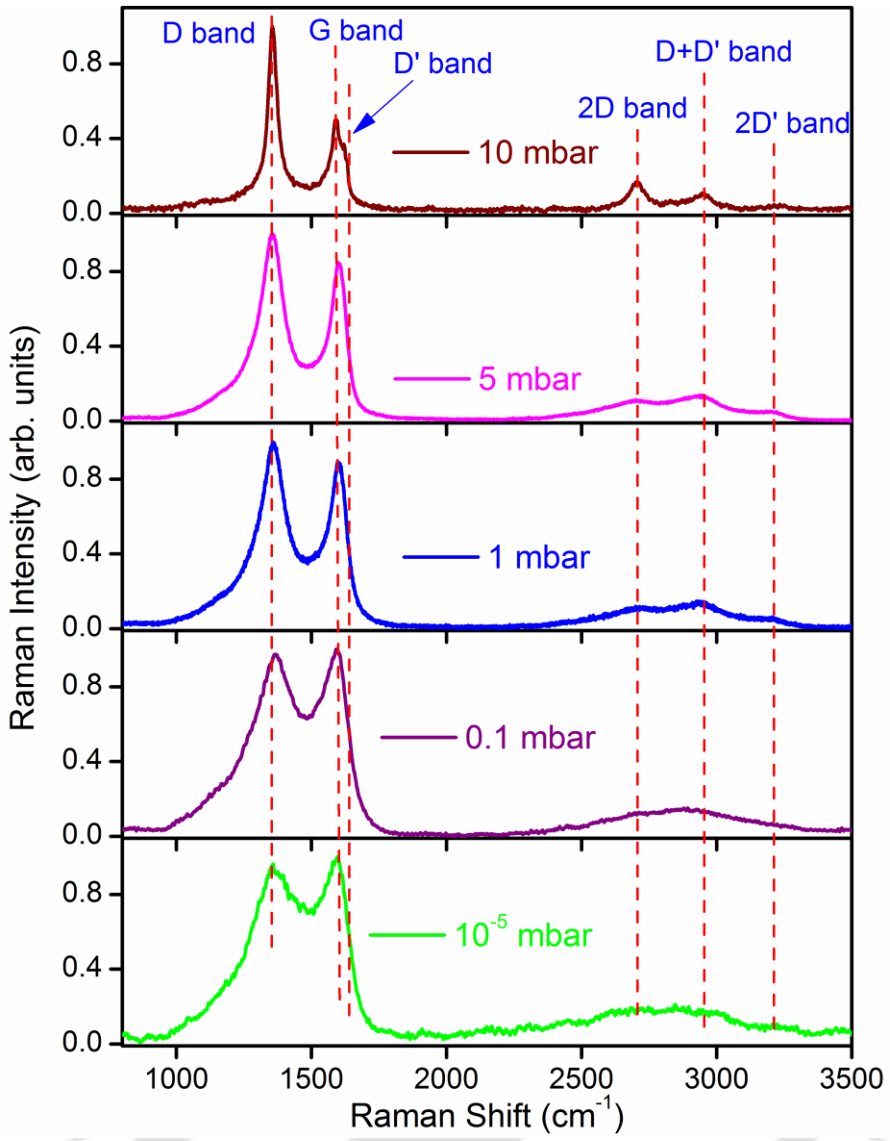

Figure 4.26: *Raman spectra of graphitic thin films as a function of helium pressure.*

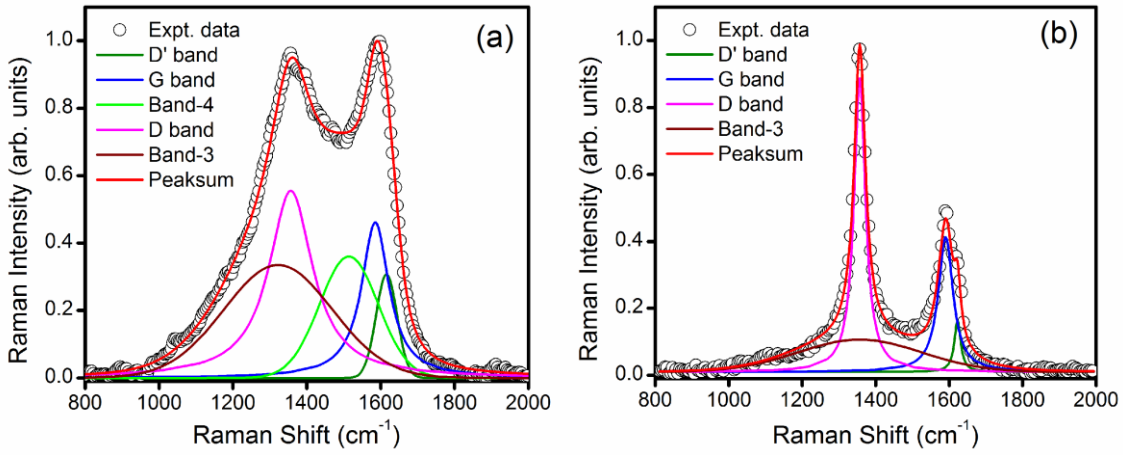

Figure 4.27: *Deconvoluted Raman spectra of graphitic thin films deposited at* ***(a)*** *10^{-5} mbar and* ***(b)*** *helium pressure of 10 mbar.*

spectra of the film deposited in the background pressure of ~10^{-5} mbar and helium pressure of 10 mbar are shown in *Figure 4.27*. The type of line-shape function for all the five deconvoluted bands; D, G, D', Band-3 and Band-4, for all the samples along with the integrated intensity ratio of Lorentzian components to that of Gaussian components, $\frac{I_{Lorentz}}{I_{Gaussian}}$, is listed in *Table 4.12*. For the film deposited at a base pressure of ~10^{-5} mbar, the deconvoluted G and D bands are Lorentzian and centred at 1585 cm^{-1} and 1357 cm^{-1} with FWHM of 90 cm^{-1} and 148 cm^{-1}, respectively.

Table 4.12: *Nature of deconvoluted Raman bands of graphitic thin films*

Deconvoluted Raman bands → Deposition Pressure ↓	**type of broadening of deconvoluted bands**					
	D band	**G band**	**D' band**	**Band-3**	**Band-4**	$\frac{I_{Lorentz}}{I_{Gaussian}}$
10^{-5} mbar	Lorentz	Lorentz	Gaussian	Gaussian	Gaussian	0.82
0.1 mbar helium	Lorentz	Lorentz	Gaussian	Gaussian	Gaussian	1.13
1 mbar helium	Lorentz	Lorentz	Lorentz	Gaussian	Gaussian	1.71
5 mbar helium	Lorentz	Lorentz	Lorentz	Gaussian	Gaussian	2.00
10 mbar helium	Lorentz	Lorentz	Lorentz	Gaussian	-	2.24

The Lorentzian line-shape of G and D bands appears due to the orderings of sp^2 bonded carbon atoms. The other deconvoluted components; Band-3,Band-4 and D' band centred at 1322 cm^{-1}, 1514 cm^{-1} and 1615 cm^{-1}, respectively, are Gaussian due to the amorphous nature of the film. The Band-3 and Band-4 ascribe to the disordered carbon networks whereas D' band originates from the microcrystalline graphitic sites. With the increase in helium pressure, the FWHM of G and D bands was found to be decreased to 46 cm^{-1} and 39 cm^{-1}, respectively, for the film deposited at helium pressure of 10 mbar, *Table 4.13*. Such narrow FWHM of G and D bands resembles to that of crystalline graphitic

material. The conversion of Gaussian line-shape of D' band into the Lorentzian line-shape with the increase in helium pressure and disappearance of disordered Band-4 at the helium pressure of 10 mbar, *Table 4.12*, indicate the evolution of crystalline structure. The integrated intensity ratio of Lorentzian bands to that of Gaussian bands, $\frac{I_{Lorentz}}{I_{Gaussian}}$, was found to be increasing with the helium pressure, *Table 4.12*, which is another conformation of increase in crystallinity in the film. Apart from these bands, crystalline graphitic material shows bands in the range of 2400 cm^{-1} to 3300 cm^{-1} [**46**].

Table 4.13: *Deconvoluted Raman band parameters of graphitic thin films as a function of ambient pressure*

Deposition pressure	**Peak position of G band (cm^{-1})**	**Peak position of D band (cm^{-1})**	**FWHM of G band (cm^{-1})**	**FWHM of D band (cm^{-1})**
10^{-5} mbar	1585	1357	90	148
0.1 mbar helium	1585	1365	90	139
1 mbar helium	1595	1360	63	102
5 mbar helium	1593	1356	48	96
10 mbar helium	1590	1356	46	39

As the film deposited at ambient pressure of ~10^{-5} mbar is highly amorphous, the signature of distinct bands in the range of 2400-3300 cm^{-1} is hardly visible. The evolution of bands in this range was observed with the increase in helium pressure and for the film deposited at the helium pressure of 10 mbar, distinct bands appeared at 2705 cm^{-1}, 2950 cm^{-1} and 3230 cm^{-1} which are designated as 2D, D+D' and 2D', respectively [**47**]. The increase in helium pressure increases the laser induced plasma density due to confinement and hence enhancing the collisions between ablated species and ambient gas molecules. This leads to decrease in kinetic energy of impinging particles so as to prevent the direct penetration of those particles to the substrate and hence the adatoms

diffuses over the substrate surface. Simultaneously, the substrate temperature of 750 °C enhances the diffusion of adatoms to long range order which favours the ordering of sp^2 sites.

4.3.2 Measurment of linear optical constants of graphitic thin films using spectroscopic ellipsometer

The linear optical properties of the graphitic thin films were studied using spectroscopic ellipsometer. The measurements were carried out in the energy range of 1.5 - 4.0 eV. The spectra of pseudo refractive index and pseudo extinction coefficient were fitted to mFB dispersion relation, *Equation (4.2)* and *(4.3)* and are shown in *Figure 4.28*. All the films consist of only sp^2 bonded carbon atoms and hence exhibited marginal variation in the optical band gap energy, *Table 4.14*. The refractive index for the film deposited at ~10^{-5} mbar was higher, 3.34, and decreased to 2.42 for the film deposited at the helium pressure of 10 mbar, *Table 4.14*. The films deposited at higher helium pressure were compartively more ordered which may be the cause for decrease in refractive index. The extinction coefficient of the film deposited at ~10^{-5} mbar was

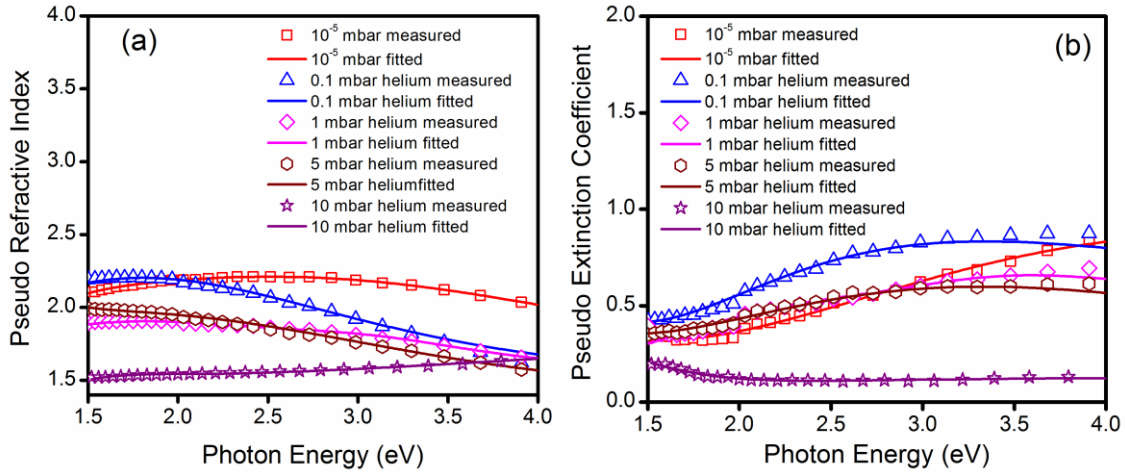

Figure 4.28: *mFB fit for* ***(a)*** *pseudo refractive index and* ***(b)*** *pseudo extinction coefficient for graphitic thin films deposited at background pressure of ~10^{-5} mbar and helium pressure of 0.1 mbar, 1 mbar, 5 mbar and 10 mbar.*

calculated to be 1.57 which was higher than those deposited at higher pressure of helium gas. The decrease in extinction coefficient for the film deposited at higher helium pressure might be due to increase in orderedness of film structure.

Table 4.14: *Band gap, refractive index and extinction coefficient of graphitic thin films as function of deposition pressure*

Deposition pressure	Band gap (eV)	Refractive index	Extinction coefficient
10^{-5} mbar	1.19	3.34	1.57
0.1 mbar helium	1.08	2.69	0.92
1 mbar helium	1.05	2.27	0.81
5 mbar helium	1.23	2.46	0.82
10 mbar helium	1.06	2.42	0.72

4.3.3. UV-Visible-NIR transmission spectra of graphitic thin films

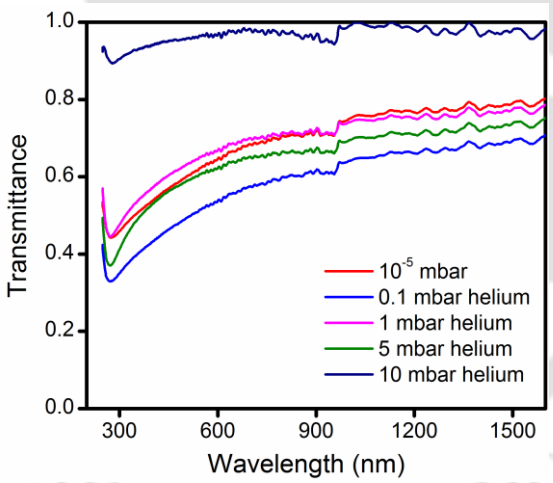

Figure 4.29: *Transmission spectra of graphitic thin films as a function of deposition pressure.*

The transmission spectra of graphitic thin films were recorded using ellipsometer, shown in *Figure 4.29*. All the films showed high transmission (65-80 %) in NIR region. The maximum absorption was observed at ~270 nm due to π-π* transition of carbon atoms. The film deposited at 10 mbar of helium pressure which was very thin (~10 nm) and highly ordered, confirmed by Raman spectra, exhibits high transparency in visible as well as in NIR region.

4.3.4 Surface morphology of graphitic thin films as a function of helium pressure

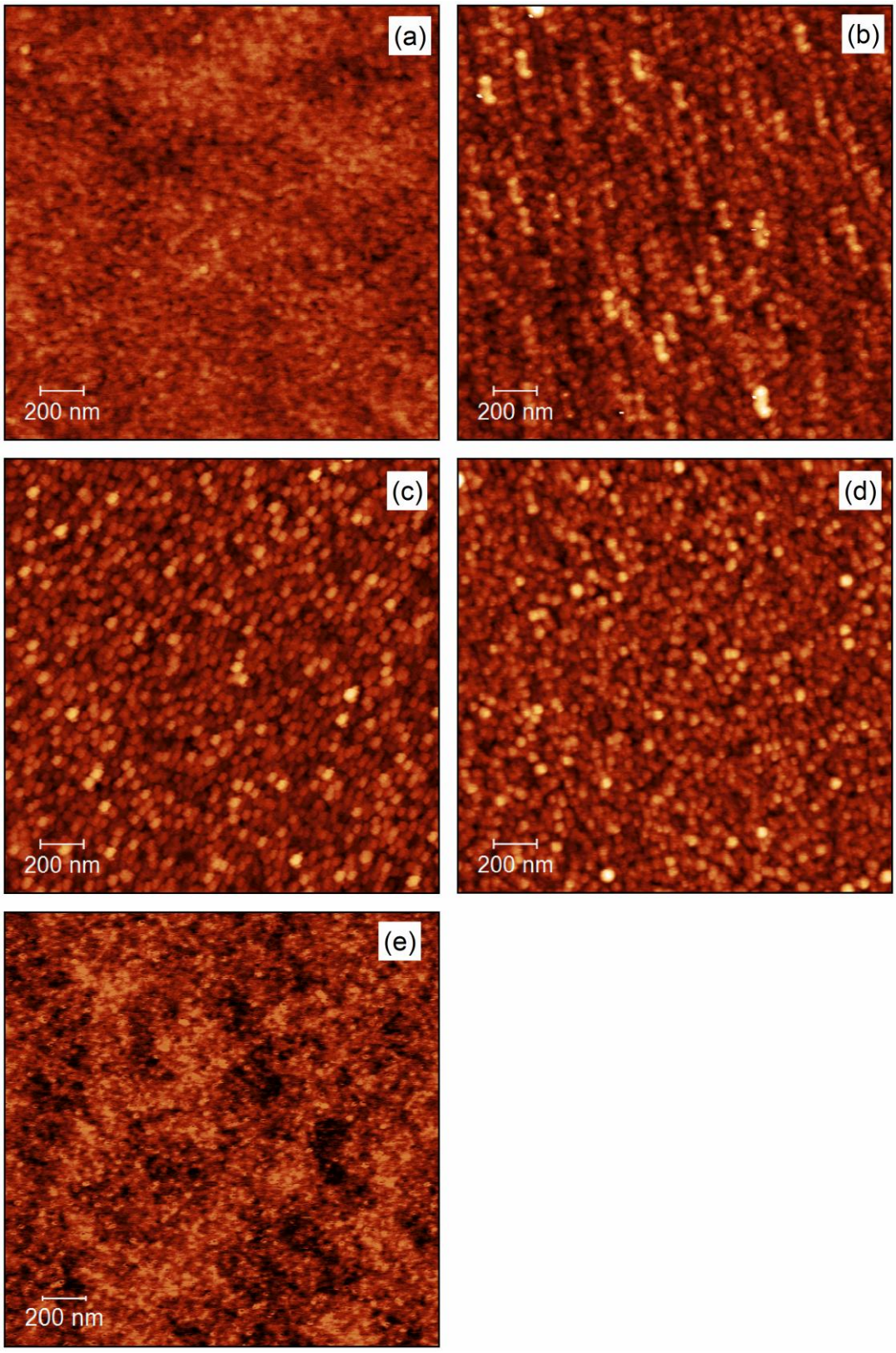

Figure 4.30: *Surface morphology of graphitic thin films as a function of deposition pressure* ***(a)*** *10^{-5} mbar,* ***(b)*** *0.1 mbar helium,* ***(c)*** *1 mbar helium,* ***(d)*** *5 mbar helium and* ***(e)*** *10 mbar helium.*

The AFM images (2 µm × 2 µm) of graphitic thin films grown onto corning glass as a function of deposition pressure are shown in *Figure 4.30*. The AFM images displayed the uniformity over the surface of thin films with the increase in helium pressure. At low pressure, ~10^{-5} mbar, the expansion of laser induced plasma is like that of a free expansion and so the density of the particles falling on the substrate is drastically curtailed resulting into very thin layer of deposition. The grains boundaries in this particular film are hazy and so it was difficult to estimate the particle size distribution. The formation of well-defined grains was observed with the increase in helium pressure. At helium pressure of 0.1 mbar and 1 mbar and the average particle size was estimated to be 30 nm and 28 nm, respectively, which increased to 42 nm for the film deposited at a helium pressure of 5 mbar, *Figure 4.31*. At helium pressure of 10 mbar, the flux density of arriving species onto the substrate was decreased due to the over confinement of LPP, as a result the film thickness is very low and hardly any grains were observed on the film surface, *Figure 4.30 (e)*.

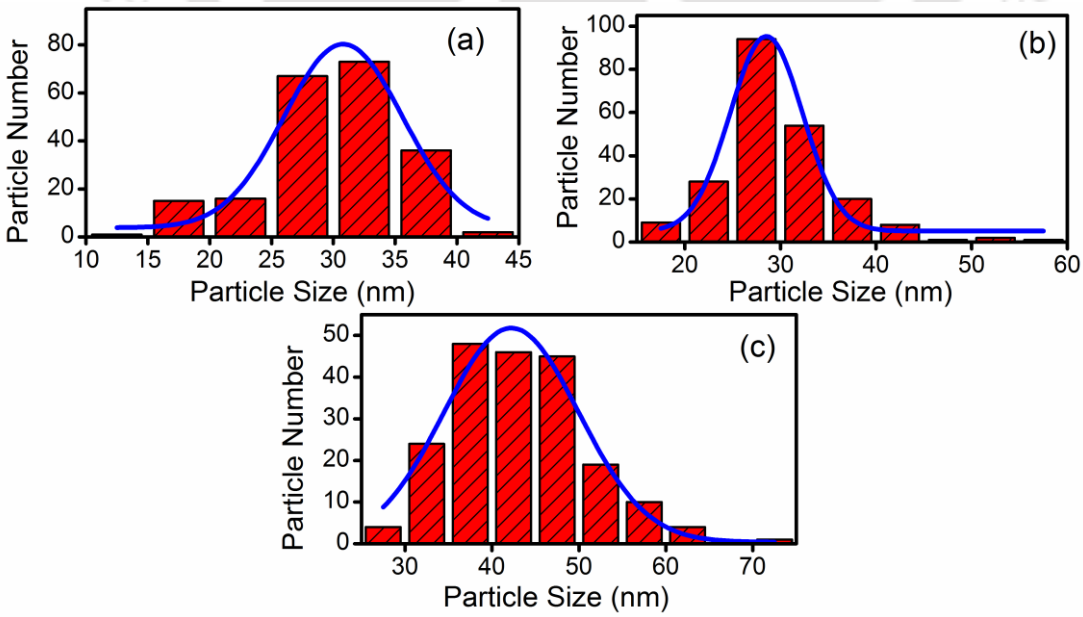

Figure 4.31: *Particle size distribution for the graphitic thin films deposited at helium pressure of (a) 0.1 mbar, (b) 1 mbar and (b) 5 mbar.*

Conclusion

DLC thin films were deposited using PLD technique over a number of deposition parameters. The effect of substrate temperature, laser fluence and helium gas pressure on the structural and optical properties of DLC thin films was studied. The Raman spectra showed the diamond-like nature for the film deposited at RT and with the increase in substrate temperature the film structure transformed to the graphite-like. The dispersion of G band position was used to estimate the $sp^3(\%)$ bonding of carbon atoms in DLC thin films and found to be ~68 % for the film deposited at RT which decreases to ~0 % at the substrate temperature of 750 °C. DLC thin films deposited at RT using various laser fluences; 5.0 J/cm^2 to 11.7 J/cm^2 in the background pressure of ~10^{-5} mbar were observed to be containing the similar ratio of carbon bonding. The increase in sp^3/sp^2 ratio of carbon bonding in DLC thin films was observed with the increase in helium gas pressure. The pseudo refractive index and extinction coefficient of DLC thin films, measured with SE, were fitted using modified FB model for the determination of thickness, optical band gap energy, refractive index and extinction coefficient. The optical band gap of the films estimated from SE using mFB model and that obtained from transmission spectra using Tauc plot followed the similar trend. The variation in refractive index and extinction coefficient of the films obtained from SE measurements supports the results obtained from Raman spectroscopy. The effect of helium gas onto the formation of graphitic thin films deposited at 750 °C was also studied by varying the pressure from 0.1 mbar to 10 mbar. The narrow FWHM of G and D bands for the film deposited at 10 mbar of helium pressure compared to that of deposited at lower pressure indicate the formation of ordered sp^2 bonded carbon atoms. The appearance of distinct Raman bands in the range of 2400-3300 cm^{-1} further confirmed the ordered graphitic nature of the film deposited at 10 mbar of helium pressure.

भारतीय प्रौद्योगिकी संस्थान गुवाहाटी
Indian Institute of Technology Guwahati

Bibliography

[**1**] J. Robertson, "Diamond-like amorphous carbon", *Materials Science and Engineering R*, **37** (2002) 129-281.

[**2**] S. Xu, D. Flynn, B.K. Tay, S. Prawer, K.W. Nugent, S.R.P. Silva, Y. Lifshitz, W.I. Milne, "Mechanical properties and Raman spectra of tetrahedral amorphous carbon films with high sp^3 fraction deposited using a filtered cathodic arc", *Philosophical Magazine B*, **76** (1997) 351-361.

[**3**] P. Patsalas, "Optical properties of amorphous carbons and their applications and perspectives in photonics", *Thin Solid Films*, **519** (2011) 3990-3996.

[**4**] S.R.P. Silva (ed.), "Properties of Amorphous Carbon ", *INSPEC ,The Institution of Electrical Engineers*, London ,United Kingdom, 2003.

[**5**] A.H. Lettington, "Applications of diamond-like carbon thin films", *Carbon*, **36** (1998) 555-560.

[**6**] A.C. Ferrari, "Diamond-like carbon for magnetic storage disks", *Surface and Coatings Technology*, **180–181** (2004) 190-206.

[**7**] C.A. Love, R.B. Cook, T.J. Harvey, P.A. Dearnley, R.J.K. Wood, "Diamond like carbon coatings for potential application in biological implants—a review", *Tribology International*, **63** (2013) 141-150.

[**8**] K. Kanda, S. Takehana, S. Yoshida, R. Watanabe, S. Takano, H. Ando, F. Shimakura, "Application of diamond-coated cutting tools", *Surface and Coatings Technology*, **73** (1995) 115-120.

[**9**] W.S. Choi, K. Kim, J. Yi, B. Hong, "Diamond-like carbon protective anti-reflection coating for Si solar cell", *Materials Letters*, **62** (2008) 577-580.

[**10**] W.I. Milne, "Electronic devices from diamond-like carbon", *Semiconductor Science and Technology*, **18** (2003) S81-S85.

[**11**] C.W. Ong, X.A. Zhao, J.T. Cheung, S.K. Lam, Y. Liu, C.L. Choy, P.W. Chan, "Thermal stability of pulsed laser deposited diamond-like carbon films", *Thin Solid Films*, **258** (1995) 34-39.

[**12**] T.A. Friedmann, K.F. McCarty, J.C. Barbour, M.P. Siegal, D.C. Dibble, "Thermal stability of amorphous carbon films grown by pulsed laser deposition", *Applied Physics Letters*, **68** (1996) 1643-1645.

[**13**] D.R. Tallant, J.E. Parmeter, M.P. Siegal, R.L. Simpson, "The thermal stability of diamond-like carbon", *Diamond and Related Materials*, **4** (1995) 191-199.

[**14**] M. Rusop, S.M. Mominuzzaman, T. Soga, T. Jimbo, M. Umeno, "Effect of helium gas on the deposition of diamond like carbon thin films by pulsed laser ablation", *International Journal of Modern Physics B*, **16** (2002) 871-875.

[**15**] T. Yoshitake, T. Nishiyama, H. Aoki, K. Suizu, K. Takahashi, K. Nagayama, "The effects of substrate temperature and laser wavelength on the formation of carbon thin films by pulsed laser deposition", *Diamond and Related Materials*, **8** (1999) 463-467.

[**16**] K.J. Koivusaari, J. Levoska, S. Leppävuori, "Pulsed-laser deposition of diamond-like carbon: Relations between laser fluence, velocity of carbon ions, and bonding in the films", *Journal of Applied Physics*, **85** (1999) 2915-2920.

[**17**] T. Yoshitake, T. Nishiyama, K. Nagayama, "The role of hydrogen and oxygen gas in the growth of carbon thin films by pulsed laser deposition", *Diamond and Related Materials*, **9** (2000) 689-692.

[**18**] H.C. Ong, R.P.H. Chang, "Effect of laser intensity on the properties of carbon plasmas and deposited films", *Physical Review B*, **55** (1997) 13213-13220.

[**19**] B.K. Tay, X. Shi, E.J. Liu, H.S. Tan, L.K. Cheah, "Effects of substrate temperature on the properties of tetrahedral amorphous carbon films", *Thin Solid Films*, **346** (1999) 155-161.

[**20**] E. Cappelli, S. Orlando, G. Mattei, C. Scilletta, F. Corticelli, P. Ascarelli, "Nano-structured oriented carbon films grown by PLD and CVD methods", *Applied Physics A*, **79** (2004) 2063-2068.

[**21**] Q. Zheng, P.V. Braun, D.G. Cahill, "Thermal conductivity of graphite thin films grown by low temperature chemical vapor deposition on Ni (111)", *Advanced Materials Interfaces*, **3** (2016) 1600234.

[**22**] S. Yamanaka, T. Nishino, T. Fujimoto, Y. Kuga, "Production of thin graphite sheets for a high electrical conductivity film by the mechanical delamination of ternary graphite intercalation compounds", *Carbon*, **50** (2012) 5027-5033.

[**23**] G.I. Dovbeshko, V.R. Romanyuk, D.V. Pidgirnyi, V.V. Cherepanov, E.O. Andreev, V.M. Levin, P.P. Kuzhir, T. Kaplas, Y.P. Svirko, "Optical properties of pyrolytic carbon films versus graphite and graphene", *Nanoscale Research Letters*, **10** (2015) 234.

[**24**] V. PesÁkovÁ, Z. Kle´zl, K. Bali´k, M. Adam, "Biomechanical and biological properties of the implant material carbon-carbon composite covered with pyrolytic carbon", *Journal of Materials Science: Materials in Medicine*, **11** (2000) 793-798.

[**25**] C. Berger, Z. Song, T. Li, X. Li, A.Y. Ogbazghi, R. Feng, Z. Dai, A.N. Marchenkov, E.H. Conrad, P.N. First, W.A. de Heer, "Ultrathin epitaxial graphite: 2D electron gas properties and a route toward graphene-based nanoelectronics", *The Journal of Physical Chemistry B*, **108** (2004) 19912-19916.

[**26**] A.C. Ferrari, J. Robertson, "Raman spectroscopy of amorphous, nanostructured, diamond–like carbon, and nanodiamond", *Philosophical Transactions of the Royal Society of London A*, **362** (2004) 2477-2512.

[**27**] A.C. Ferrari, J. Robertson, "Interpretation of Raman spectra of disordered and amorphous carbon", *Physical Review B*, **61** (2000) 14095-14107.

[**28**] F. Tuinstra, J.L. Koenig, "Raman spectrum of graphite", *The Journal of Chemical Physics*, **53** (1970) 1126-1130.

[**29**] M.A. Tamor, W.C. Vassell, "Raman ‘‘fingerprinting’’ of amorphous carbon films", *Journal of Applied Physics*, **76** (1994) 3823-3830.

[**30**] N.H. Cho, D.K. Veirs, J.W. Ager, M.D. Rubin, C.B. Hopper, D.B. Bogy, "Effects of substrate temperature on chemical structure of amorphous carbon films", *Journal of Applied Physics*, **71** (1992) 2243-2248.

[**31**] J. Schwan, S. Ulrich, V. Batori, H. Ehrhardt, S.R.P. Silva, "Raman spectroscopy on amorphous carbon films", *Journal of Applied Physics*, **80** (1996) 440-447.

[**32**] W.G. Cui, Q.B. Lai, L. Zhang, F.M. Wang, "Quantitative measurements of sp^3 content in DLC films with Raman spectroscopy", *Surface and Coatings Technology*, **205** (2010) 1995-1999.

[**33**] S. Neuville, "Quantum electronic mechanisms of atomic rearrangements during growth of hard carbon films", *Surface and Coatings Technology*, **206** (2011) 703-726.

[**34**] R.J. Nemanich, S.A. Solin, "First- and second-order Raman scattering from finite-size crystals of graphite", *Physical Review B*, **20** (1979) 392-401.

[**35**] A.R. Forouhi, I. Bloomer, "Optical dispersion relations for amorphous semiconductors and amorphous dielectrics", *Physical Review B*, **34** (1986) 7018-7026.

[**36**] W.A. McGahan, T. Makovicka, J. Hale, J.A. Woollam, "Modified Forouhi and Bloomer dispersion model for the optical constants of amorphous hydrogenated carbon thin films", *Thin Solid Films*, **253** (1994) 57-61.

[**37**] Y. Liu, G. Xu, C. Song, W. Weng, P. Du, G. Han, "Modification on Forouhi and Bloomer model for the optical properties of amorphous silicon thin films", *Thin Solid Films*, **515** (2007) 3910-3913.

[**38**] D.R. Penn, "Wave-number-dependent dielectric function of semiconductors", *Physical Review*, **128** (1962) 2093-2097.

[**39**] R. Lossy, D.L. Pappas, R.A. Roy, J.P. Doyle, J.J. Cuomo, J. Bruley, "Properties of amorphous diamond films prepared by a filtered cathodic arc", *Journal of Applied Physics*, **77** (1995) 4750-4756.

[**40**] S.R. Sails, D.J. Gardiner, M. Bowden, J. Savage, D. Rodway, "Monitoring the quality of diamond films using Raman spectra excited at 514.5 nm and 633 nm", *Diamond and Related Materials*, **5** (1996) 589-591.

[**41**] S.E. Rodil, "Infrared spectra of amorphous carbon based materials", *Diamond and Related Materials*, **14** (2005) 1262-1269.

[**42**] A.C. Ferrari, J. Robertson, "Origin of the 1150-cm^{-1} Raman mode in nanocrystalline diamond", *Physical Review B*, **63** (2001) 121405.

[**43**] A.A. Khan, D. Mathine, J.A. Woollam, Y. Chung, "Optical properties of "diamondlike" carbon films: An ellipsometric study", *Physical Review B*, **28** (1983) 7229-7235.

[**44**] J. Zhu, J. Han, X. Han, S. Meng, A. Liu, X. He, "Optical properties of amorphous diamond films evaluated by non-destructive spectroscopic ellipsometry", *Optical Materials*, **28** (2006) 473-479.

[**45**] M.I. Nathan, J.E. Smith, K.N. Tu, "Raman spectra of glassy carbon", *Journal of Applied Physics*, **45** (1974) 2370.

[**46**] J.H. Kwak, S.S. Lee, H.J. Lee, G. Anoop, H.J. Lee, W.S. Kim, S.-W. Ryu, H.S. Kim, J.Y. Jo, "Direct growth of nano-crystalline graphite films using pulsed laser deposition with in-situ monitoring based on reflection high-energy electron diffraction technique", *Applied Physics Letters*, **108** (2016) 123107.

[**47**] B. Ryan, C. Luiz Gustavo, N. Lukas, "Raman characterization of defects and dopants in graphene", *Journal of Physics: Condensed Matter*, **27** (2015) 083002.

Chapter 5

Fabrication and characterization of few- and multi-layer graphene via PLD technique

Graphene is a thermodynamically stable two-dimensional hexagonal lattice structure of sp^2 bonded carbon atoms. It possesses exceptional thermal, electrical, optical and mechanical properties leading to its potential applications in research and industry as transparent electrodes, field emitters, biosensors etc. [**1-6**]. The first experimentally produced graphene was reported in 2004 using mechanical cleavage process [**7**]. Afterwards, several techniques have been explored for synthesis of graphene. Majority of the techniques require catalytic metal for the growth and then it is to be transferred onto desired substrate making it two-step process [**8, 9**]. Whereas, in PLD technique, laser ablated species are of high kinetic energy and hence it facilitates the formation of graphene layers directly onto any desired substrate thus making the process single step only. The fabrication of Graphene via PLD technique was reported by Zhang and Feng using excimer laser onto Ni substrate at the elevated temperature ranging 1100 °C to 1300 °C [**10**]. The effect of substrate cooling rate after the deposition and laser energy in fabricating graphene layers on a Ni plate using PLD technique was explained by Koh et al. [**11**].

In the present chapter, the evolution of graphene from few layers to multilayer onto the fused silica substrate as a function of deposition temperature by pulsed laser

ablation of graphite target without using any catalyst is detailed. Multilayer graphene (MLG) and few-layer graphene (FLG) were characterized by Raman spectrometer, Transmission electron microscope (TEM) and Field emission scanning electron microscope (FESEM).

5.1 Experimental details

The PLD setup used for the fabrication of few- and multi- layer graphene is described in *Section 2.1*, *Chapter 2*,. The graphite target was ablated by focusing the second harmonic of high power *Q*-switched Nd:YAG laser in oxygen gas at a pressure of 0.1 mbar and deposited onto the fused silica substrates placed at ~3 cm apart from the target. Prior to pressuring the ablation chamber with oxygen gas, it was evacuated to a base pressure of ~10^{-6} mbar. The graphene layers were deposited for 15 min at deposition temperatures ranging from room temperature (RT) to 700 °C.

The Raman spectra of graphene layers were recorded with the micro-Raman setup using three different laser excitation sources: 488 nm, 514 nm and 633 nm in a back scattering geometry, at RT. Field emission scanning electron microscope and Transmission electron microscope images were recorded to study the surface morphology and selected area electron diffraction (SAED) pattern of the graphene layers, respectively.

5.2 Raman spectra of few- and multi- layer graphene

The Raman spectra of the graphene layers deposited on fused silica substrate as a function of substrate temperature recorded at excitation laser wavelength of 514 nm are shown in *Figure 5.1*. The prominent Raman features of graphitic materials at ~1367 cm^{-1} (D band), ~1584 cm^{-1} (G band) and ~2730 cm^{-1} (2D band) are clearly observed.

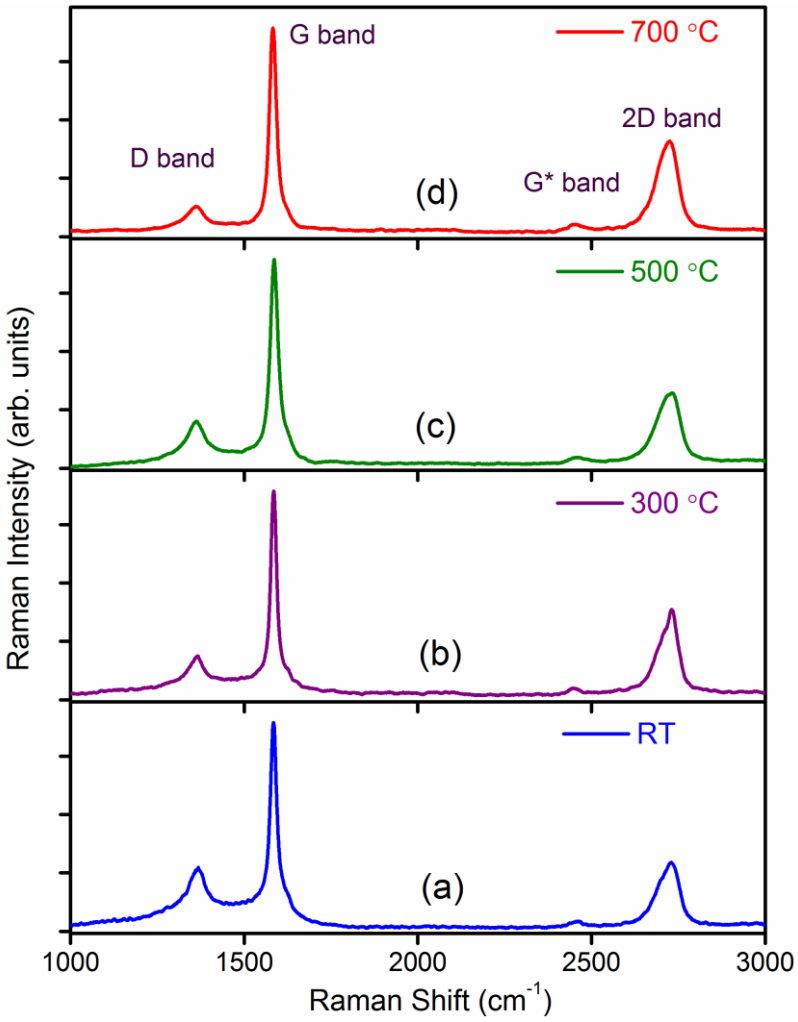

***Figure 5.1**: Raman spectra of graphene layers deposited at **(a)** RT, **(b)** 300 °C, **(c)** 500 °C and **(d)** 700 °C.*

The Raman D band arises due to the presence of disorder in graphene and depends on the breathing mode of the aromatic rings. The disorder may be due to stacking between two layers, atomic defects within the layer and edges in finite crystallite sites [**12, 13**]. The G band originates from first order Raman scattering process and corresponds to the in-plane vibration of sp^2 bonded carbon atoms [**14**]. The FWHM of the G band (obtained by Lorentzian fit) was observed to be 24.8 cm^{-1} for the graphene layers deposited at RT which decreased to 21.7 cm^{-1} for that of deposited at 700 °C. The narrowing of the FWHM of G band at higher substrate temperature indicates the increase in crystallinity in graphene layers. The intensity ratio of D and G bands (I_D/I_G) for

graphene layers as a function of substrate temperature is listed in *Table 5.1*. The intensity ratio, I_D/I_G, was observed to decrease with the increase in substrate temperature. The decrease in D band intensity and hence the intensity ratio, I_D/I_G, with the increasing substrate temperature indicates the decrease in defect and hence formation of ordered graphene layers at higher substrate temperature.

Table 5.1: *Raman intensity ratio, I_D/I_G and I_{2D}/I_G of graphene layers as a function of substrate temperature*

Deposition temperature	RT	100 °C	200 °C	300 °C	400 °C	500 °C	600 °C	700 °C
$\mathbf{I_D/I_G}$	0.31	0.36	0.27	0.22	0.22	0.21	0.16	0.13
$\mathbf{I_{2D}/I_G}$	0.33	0.34	0.35	0.39	0.39	0.37	0.44	0.47

The 2D band observed at 2730 cm^{-1} originates from a two phonon double resonance Raman process and is closely related to the band structure of the graphene layers [**15**]. The splitting of 2D band and the relative intensities of 2D and G band (I_{2D}/I_G) is indicative of number of layers in the graphene samples [**16, 17**]. *Figure 5.2* illustrates the magnified view of 2D band shape along with multiple Lorentzian peak fitting of graphene layers deposited at (a) RT (b) 300 °C (c) 500 °C and (d) 700 °C. The intensity ratio, I_{2D}/I_G, the number of sub-peaks of 2D band and the peak separation between them is sensitive to the number of graphene layers [**18**]. The 2D band shape and intensity ratio, I_{2D}/I_G, in Raman spectra show MLG formation at RT. The I_{2D}/I_G ratio for MLG was ~ 0.33 and increased with increasing substrate temperature, as listed in *Table 5.1*. At substrate temperature of 700 °C, the I_{2D}/I_G ratio for graphene layers became ~ 0.47 which corresponds to less than 5 layers [**19**]. For monolayer graphene, the 2D band has single Lorentzian peak, whereas bilayer graphene has four Lorentzian sub-peaks. Here only two sub-peaks were observed for all the samples confirming that number of

graphene layers is more than two. For the MLG, deposited at RT, the separation between two sub-peaks in 2D band was 32.25 cm^{-1} indicating the presence of ~10 layers. This wavenumber separation was found to decrease with increase in substrate temperature, indicating the decrease in number of graphene layers with increase in substrate

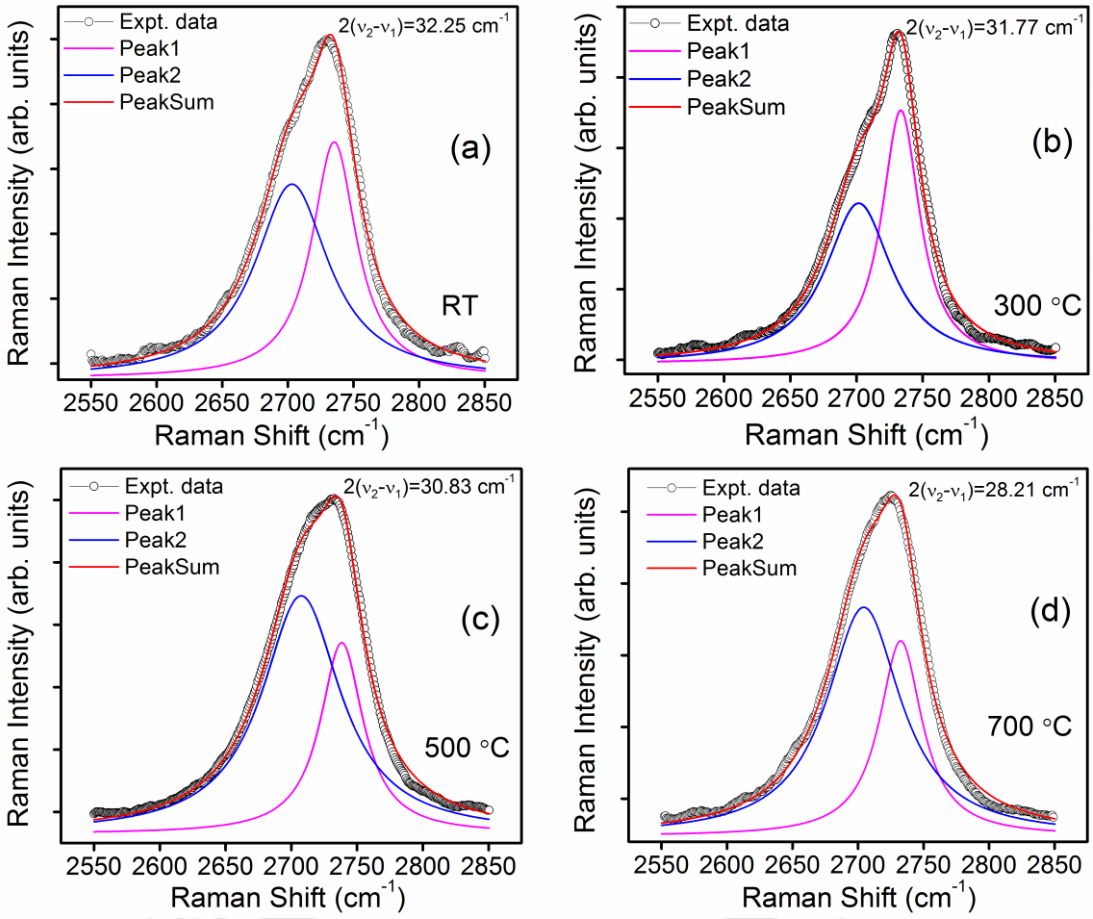

***Figure 5.2**: 2D band splitting of graphene layers deposited at **(a)** RT, **(b)** 300 °C, **(c)** 500 °C and **(d)** 700 °C.*

temperature. At substrate temperature of 700 °C, the separation between the sub-peaks was found to be 28.21 cm^{-1}, clearly indicating the presence of approximately 4-5 layers [**11**]. In addition to these bands, a broad band was observed at 2459 cm^{-1} (G* band) in all the samples. The Raman G* band originates from double resonance Raman scattering, a combination of the zone boundary in-plane longitudinal acoustic (*iLA*) phonon and the in-plane transverse optical (*iTO*) phonon modes [**20**]. The dependence of the property of

graphene layers on substrate temperature can be explained on the basis of the diffusion coefficient. At RT and low substrate temperatures, the carbon atoms with a certain amount of energy are deposited onto the fused silica substrate in highly localized manner due to the lack of sufficient mobility. As the substrate temperature increases, the mobility of the carbon adatoms increases due to increase in the diffusion coefficient, which is given by *Equation (5.1)* [**19**].

$$D = D_o \exp(-\frac{E_a}{RT}) \tag{5.1}$$

where 'D' is the diffusion coefficient, 'D_0' is the maximum diffusion coefficient (at infinite temperature), 'E_a' is the activation energy for diffusion, 'T' is the substrate temperature and 'R' is the gas constant. As the rate of diffusion increases at higher temperature, adatoms rearrange themselves to form more ordered graphene layers, which was reflected by the lower intensity ratio, I_D/I_G, in the Raman spectra with the increasing substrate temperature (*Table 5.1*). After deposition, all the samples were allowed to cool at the rate of ~3.3 °C/min up to 100 °C and then left for natural cooling. The ambient pressure of the chamber was maintained at deposition pressure (0.1 mbar of O_2 gas) throughout during cooling. The slower cooling rate provides the sufficient time for the adatoms to rearrange themselves. At the elevated substrate temperature of 700 °C, the mobility of the carbon atoms was high enough and had sufficient time to diffuse due to slow cooling rate, and hence formed FLG in agreement with the 2D band shape of Raman spectrum of FLG as shown in *Figure 5.2*.

Figure 5.3 shows the dependence of Raman spectrum of graphene layers (deposited at 700 °C) on the excitation laser wavelength. The position of G band is nearly independent of the excitation laser wavelength. All the other bands of graphene layers; D, 2D and G* exhibit the linear dispersion behaviour due to double resonance

process [**21**]. By changing the laser excitation energy, different points in momentum space for the electronic and phonon dispersion are probed [**22**]. The Raman shift position of D, G, G* and 2D band as a function of excitation laser are listed in *Table 5.2*. The Raman shift of D and 2D band increases with the laser wavelength.

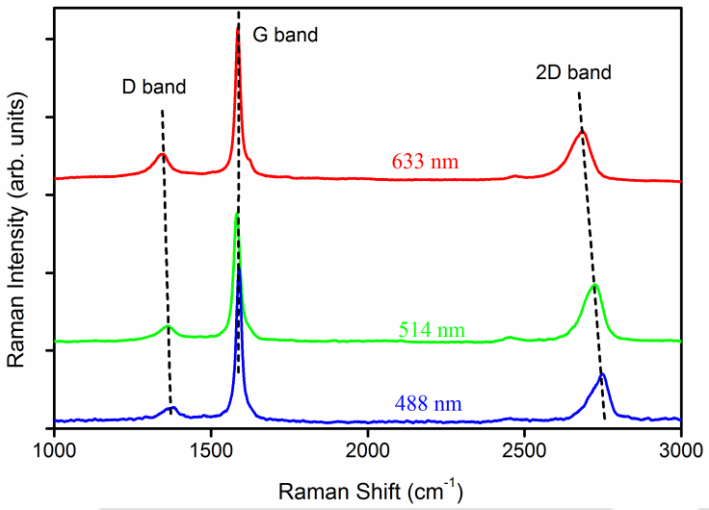

***Figure 5.3**: Variation in Raman spectrum of graphene sample prepared at 700 °C with excitation laser wavelength.*

***Table 5.2:** Dispersion of D and 2D band with the excitation laser wavelength in Raman spectra of FLG*

Excitation wavelength (nm)	**Position of D band (cm^{-1})**	**Position of G band (cm^{-1})**	**Position of G* band (cm^{-1})**	**Position of 2D band (cm^{-1})**
488	1377	1586	2452	2747
514	1367	1584	2459	2730
633	1344	1583	2472	2684

The plot of D and 2D peak position ($\bar{\nu}$) as a function of laser photon energy (E_l) is shown in *Figure 5.4*. The slopes, $\partial\bar{\nu}/\partial E_l$, for D and 2D bands were calculated from the linear fitting of the '$\bar{\nu}$' versus 'E_l' graph. The slope, $\partial\bar{\nu}_{2D}/\partial E_l$, is approximately two times of $\partial\bar{\nu}_D/\partial E_l$ which confirm that 2D band is the second harmonic of the D band, *Equations (5.2) and (5.3).*

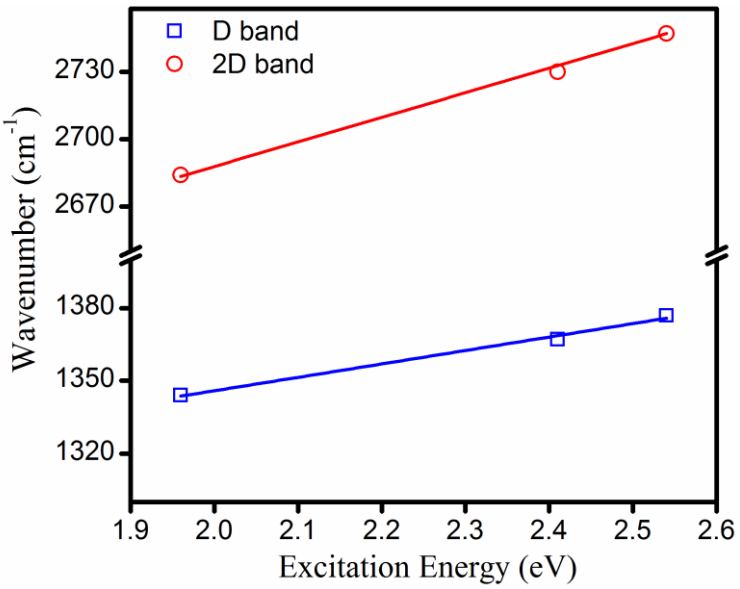

***Figure 5.4**: Dispersion of D and 2D peak position of few-layer graphene.*

$$\frac{\partial \bar{\nu}_D}{\partial E_l} = 55.3 \text{ cm}^{-1} / eV \tag{5.2}$$

$$\frac{\partial \bar{\nu}_{2D}}{\partial E_l} = 109.5 \text{ cm}^{-1} / eV \tag{5.3}$$

The Raman G* band of FLG also showed dispersive behaviour. The acoustic (LA) phonon associated with G* band has less contribution to the intense singularity in the double resonance phonon density of states. As a result, it is weaker and less pronounced compared to that of D and 2D bands. Its Raman shift decreases with the increase in laser photon energy [**12, 21**].

5.3 Transmission electron microscope images of few- and multi- layer graphene

Figure 5.5 shows the TEM images and corresponding SAED pattern of multilayer graphene deposited at RT. The graphene layers shown in TEM micrograph, Figure 5.5 (a) and (b), are randomly oriented which is also reflected in its SAED pattern with overlapping diffraction points in *Figure 5.5 (c). Figure 5.6 (a)* shows the TEM image of FLG deposited at substrate temperature of 700 °C. The corresponding ultra-high-

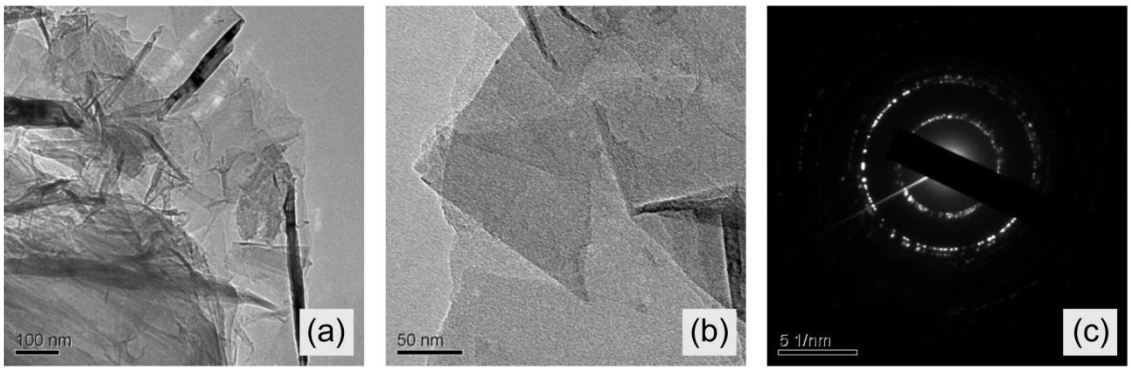

***Figure 5.5**: **(a)**, **(b)** TEM images and **(c)** SAED pattern of graphene sample prepared at RT.*

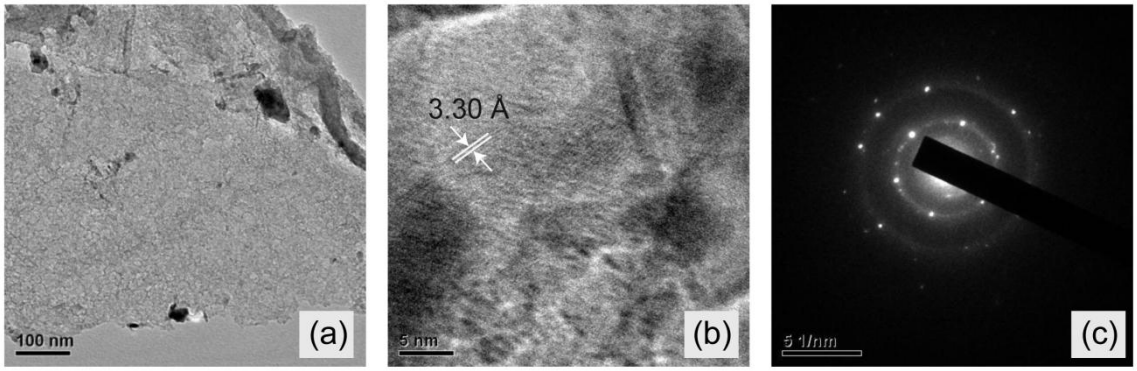

***Figure 5.6: (a)** TEM images, **(b)** HRTEM and **(c)** SAED pattern of graphene sample prepared at 700 °C.*

resolution TEM (UHRTEM) image is shown in *Figure 5.6 (b)*. To identify the crystallinity of graphene, SAED pattern was recorded from corresponding domain. As shown in *Figure 5.6 (c)*, spots in diffraction pattern were in hexagonal geometry, confirming that the FLG formed at 700 °C has high crystallinity. The lattice *d*-spacing was calculated from HRTEM image, *Figure 5.6 (b)*, and SAED pattern, *Figure 5.6 (c)*, using Gatan Digital Micrograph software attached with the TEM instrument and found to be ~3.30 Å. The interlayer spacing value is nearly close to its theoretical value 3.35 Å (crystalline graphite), confirming the good stacking of graphene layers [**23**]. These TEM results support well the observation made in Raman measurement, *Section 5.2*, and confirm that sample prepared at RT and 700 °C are MLG and FLG, respectively.

5.4 Field emission scanning electron microscopy of few- and multi- layer graphene

Figure 5.7 (a) and (b) shows the FESEM images of graphene layers prepared at RT and 700 °C, respectively. From colour contrast of the images, it can be easily seen that the number of graphene layers are less at higher substrate temperature with reduced defects, which is again in accordance with the Raman spectrum.

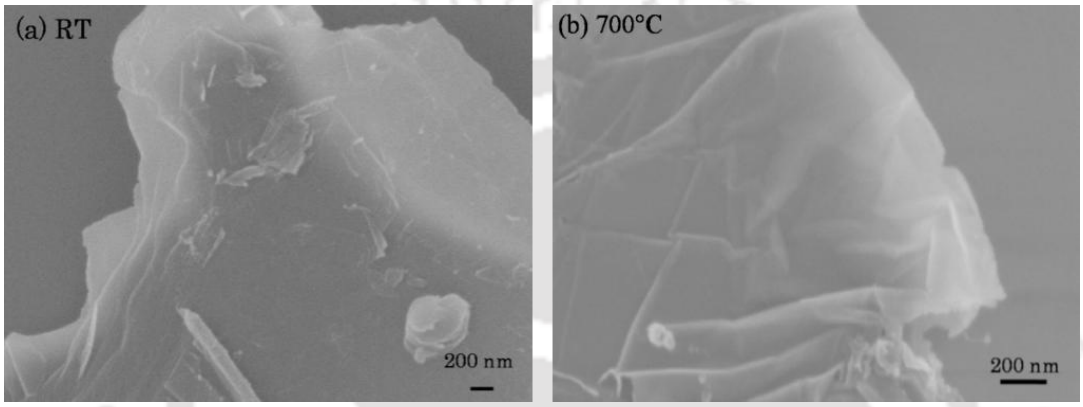

***Figure 5.7**: FESEM images of graphene layers deposited at **(a)** RT and **(b)** 700 °C.*

Conclusion

Graphene layers were prepared via PLD technique at different substrate temperatures from RT to 700 °C in a single step without using any catalyst. 4-5 graphene layers were formed at 700 °C whereas MLG were formed at lower substrate temperature. Raman spectra exhibited the D, G, 2D and G* bands of sp^2 carbon networks. The decrease in I_D/I_G ratio with the increase in substrate temperature indicated the reduction of defects at higher temperature. The presence of G* band and the splitting of 2D band confirmed the formation of multilayer and few layer graphene. The sample deposited at 700 °C indicates the formation of few layers of graphene due to the diffusion of the adatoms of carbon at elevated substrate temperature. TEM images showed the formation of folded and disordered graphene in random orientation at RT whereas few-layer graphene with high crystallinity were formed at 700 °C.

Bibliography

[**1**] M.J. Allen, V.C. Tung, R.B. Kaner, "Honeycomb carbon: A review of graphene", *Chemical Reviews*, **110** (2010) 132-145.

[**2**] R. Prasher, "Graphene spreads the heat", *Science*, **328** (2010) 185-186.

[**3**] A.K. Geim, K.S. Novoselov, "The rise of graphene", *Nature Materials*, **6** (2007) 183-191.

[**4**] F. Bonaccorso, Z. Sun, T. Hasan, A.C. Ferrari, "Graphene photonics and optoelectronics", *Nature Photonics*, **4** (2010) 611-622.

[**5**] Y.D. Kim, M.-H. Bae, J.-T. Seo, Y.S. Kim, H. Kim, J.H. Lee, J.R. Ahn, S.W. Lee, S.-H. Chun, Y.D. Park, "Focused-laser-enabled p–n junctions in graphene field-effect transistors", *ACS Nano*, **7** (2013) 5850-5857.

[**6**] T. Kuila, S. Bose, P. Khanra, A.K. Mishra, N.H. Kim, J.H. Lee, "Recent advances in graphene-based biosensors", *Biosensors and Bioelectronics*, **26** (2011) 4637-4648.

[**7**] K.S. Novoselov, A.K. Geim, S.V. Morozov, D. Jiang, Y. Zhang, S.V. Dubonos, I.V. Grigorieva, A.A. Firsov, "Electric field effect in atomically thin carbon films", *Science*, **306** (2004) 666-669.

[**8**] L.G.D. Arco, Y. Zhang, A. Kumar, C. Zhou, "Synthesis, transfer, and devices of single- and few-layer graphene by chemical vapor deposition", *IEEE Transactions on Nanotechnology*, **8** (2009) 135-138.

[**9**] A. Reina, X. Jia, J. Ho, D. Nezich, H. Son, V. Bulovic, M.S. Dresselhaus, J. Kong, "Large area, few-layer graphene films on arbitrary substrates by chemical vapor deposition", *Nano Letters*, **9** (2009) 30-35.

[**10**] H. Zhang, P.X. Feng, "Fabrication and characterization of few-layer graphene", *Carbon*, **48** (2010) 359-364.

[**11**] A.T.T. Koh, Y.M. Foong, D.H.C. Chua, "Cooling rate and energy dependence of pulsed laser fabricated graphene on nickel at reduced temperature", *Applied Physics Letters*, **97** (2010) 114102.

[**12**] J. Maultzsch, S. Reich, C. Thomsen, "Double-resonant Raman scattering in graphite: Interference effects, selection rules, and phonon dispersion", *Physical Review B*, **70** (2004) 155403.

[**13**] P. Vancsó, G.I. Márk, P. Lambin, A. Mayer, C. Hwang, L.P. Biró, "Effect of the disorder in graphene grain boundaries: A wave packet dynamics study", *Applied Surface Science*, **291** (2014) 58-63.

[**14**] F. Tuinstra, J.L. Koenig, "Raman spectrum of graphite", *The Journal of Chemical Physics*, **53** (1970) 1126-1130.

[**15**] L.M. Malard, M.A. Pimenta, G. Dresselhaus, M.S. Dresselhaus, "Raman spectroscopy in graphene", *Physics Reports*, **473** (2009) 51-87.

[**16**] A.C. Ferrari, J.C. Meyer, V. Scardaci, C. Casiraghi, M. Lazzeri, F. Mauri, S. Piscanec, D. Jiang, K.S. Novoselov, S. Roth, A.K. Geim, "Raman spectrum of graphene and graphene layers", *Physical Review Letters*, **97** (2006) 187401.

[**17**] Z. Ni, Y. Wang, T. Yu, Z. Shen, "Raman spectroscopy and imaging of graphene", *Nano Research*, **1** (2008) 273-291.

[**18**] L.-Y. Lin, D.-E. Kim, W.-K. Kim, S.-C. Jun, "Friction and wear characteristics of multi-layer graphene films investigated by atomic force microscopy", *Surface and Coatings Technology*, **205** (2011) 4864-4869.

[**19**] A.T.T. Koh, Y.M. Foong, D.H.C. Chua, "Comparison of the mechanism of low defect few-layer graphene fabricated on different metals by pulsed laser deposition", *Diamond and Related Materials*, **25** (2012) 98-102.

[**20**] D. Yoon, H. Moon, H. Cheong, J.S. Choi, J.A. Choi, B.H. Park, "Variations in the Raman spectrum as a function of the number of graphene layers", *Journal of the Korean Physical Society*, **55** (2009) 1299-1303.

[**21**] D.L. Mafra, G. Samsonidze, L.M. Malard, D.C. Elias, J.C. Brant, F. Plentz, E.S. Alves, M.A. Pimenta, "Determination of LA and TO phonon dispersion relations of graphene near the Dirac point by double resonance Raman scattering", *Physical Review B*, **76** (2007) 233407.

[**22**] M.A. Pimenta, G. Dresselhaus, M.S. Dresselhaus, L.G. Cancado, A. Jorio, R. Saito, "Studying disorder in graphite-based systems by Raman spectroscopy", *Physical Chemistry Chemical Physics*, **9** (2007) 1276-1291.

[**23**] A. Jorio, R. Saito, G. Dresselhaus, M.S. Dresselhaus, "Raman spectroscopy in graphene related systems", *Wiley-VCH*, 2011.

Chapter 6

Modified Z-scan setup using CCD camera

In 1989, Sheik-Bahae et al. reported the *Z*-scan technique, for measuring the sign and magnitude of the third-order nonlinear refractive index coefficient of a material [**1**]. Since then, the *Z*-scan technique has been widely used for measuring the nonlinear optical properties of materials because of its experimental simplicity and sensitivity compared to that of other techniques involving relatively complex experimental setup [**2-4**]. The nonlinear absorption (NLA) coefficient and nonlinear refractive index (NLR) coefficient are determined from the open aperture (OA) and closed aperture (CA) *Z*-scan transmittance curve, respectively. The schematic of experimental setup proposed by Sheik et al. is shown in *Figure 6.1 (a) and (b)* for OA and CA *Z*-scan, respectively. In this conventional *Z*-scan setup, a photodiode is used to record the transmitted intensity and hence requires a hard aperture to record the intensity of central portion of the transmitted beam for CA *Z*-scan.

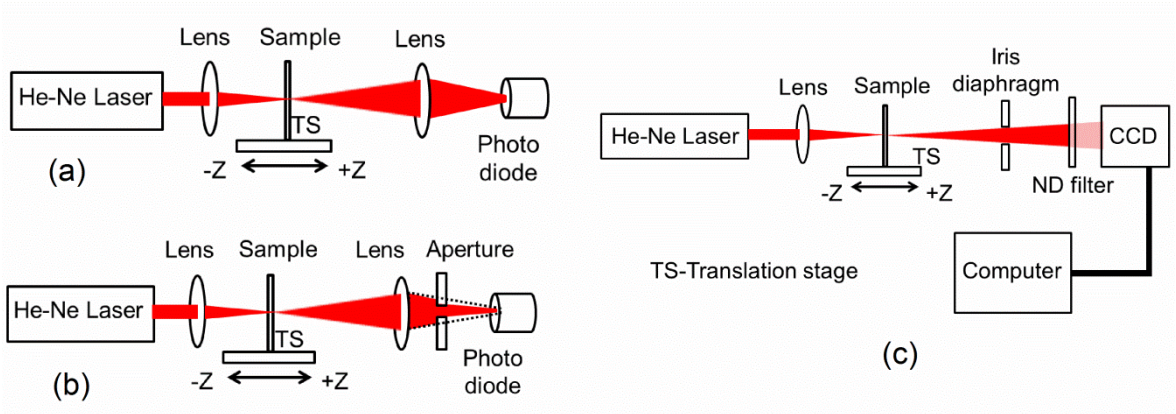

Figure 6.1: *Schematic of* ***(a)*** *conventional Z-scan setup in open aperture configuration* ***(b)*** *conventional Z-scan setup in closed aperture configuration and* ***(c)*** *modified Z-scan setup.*

In the present chapter, the modification in the conventional *Z*-scan experimental setup is demonstrated by replacing the photodiode with a charge-coupled device (CCD) camera as shown in *Figure 6.1 (c)*. The *Z*-scan measurements using CCD reported earlier were based on (a) subtracting the reference beam from signal beam [**5**], (b) replacing aperture with an opaque disk [**6**] and (c) measuring the beam dimension [**7**]. In the present setup, the hard aperture for CA *Z*-scan has been replaced by a software aperture and the transmitted intensity was obtained simply by integrating the image gray values. This modified *Z*-scan setup using CCD offers several advantages over conventional system using a photodiode: (a) the dynamic range of a CCD detector is very large and its pixel size is in few micrometres, which enhances the sensitivity compared to that of the conventional *Z*-scan setup, (b) a suitable synthetic aperture was applied onto the image using Matlab program, making it independent of the beam pointing instability of the laser, (c) a hard aperture (usually circular pinhole in conventional *Z*-scan) doesn't follow the shape of the beam and so it can't be used for beams having profile other than Gaussian beam. In the modified *Z*-scan setup, the synthetic aperture employed numerically by Matlab program, can be easily defined so as to match the incident laser beam profile, (d) it reduces the experiment running time, as data was obtained for both, open as well as closed aperture configuration in a single *Z*-scan and (e) focusing lens in front of the detector is not required. In CA *Z*-scan measurement, an aperture is used to separate out the contribution of absorptive nonlinearity from the nonlinearity due to refractive index. A closed *Z*-scan curve having height of peak and depth of valley being equal is devoid of contribution of NLA [**1**]. If the aperture size is not appropriate then the CA curve is not symmetric and hence the calculated NLR coefficient will be incorrect. In CA *Z*-scan setup using photodiode, the experiment is to be repeated for various apertures to obtain the optimum aperture size such that peak and valley of the curve are equal. The

CCD camera records the profile of the transmitted beam and so data for variant aperture size from the same set of images can be obtained by applying the aperture via software after recording the full images. Thus, the data is extracted for both, OA and CA from same set of images and the effect of any fluctuations in the laser beam is automatically cancelled out and simultaneous recording of the reference beam is not required.

6.1 Experimental details

To demonstrate the modified *Z*-scan experimental setup, an amorphous carbon thin film was used as a nonlinear medium. The carbon thin film was deposited by the pulsed laser deposition (PLD) technique. The deposition was carried out using a Q-switched Nd:YAG laser at a base pressure of ~10^{-5} mbar. The film was deposited for 5 min onto fused silica at a substrate temperature of 750 °C using graphite target. The thickness, *L*, of the film was measured using stylus profilometer and found to be ~30 nm which is much less than the Rayleigh length of the He-Ne laser beam and hence fulfils the thin sample approximation for *Z*-scan technique. The linear absorption coefficient 'α' was calculated from the absorption spectra using the expression $\alpha = -(1/L)\ln(I/I_i)$, where '*I'* is the transmitted intensity through the carbon thin film and 'I_i*'* is the incident laser intensity onto it. The linear absorption coefficient of the carbon film at 632.8 nm was found to be 2.74×10^5 cm^{-1}. The NLO behaviour of the carbon film was studied using modified *Z*-scan setup with a He-Ne laser. The schematic of modified *Z*-scan setup for the measurement of NLA and NLR coefficients is shown in *Figure 6.1 (c).* To determine the NLR coefficient with good accuracy, the aperture size (*S*) was optimized by varying it in the range of 0.20-0.60, where the aperture size '*S*' is defined as the ratio of transmitted intensity through the aperture to that of without it when the sample is positioned at far field (beyond the Rayleigh length).

6.2 Analysis of CCD images for extracting NLA and NLR coefficients

The images of the transmitted beam were recorded by scanning the film up to 20 mm on either side of the focal position of the lens. The recorded CCD image of the transmitted beam through the thin film positioned at 20 mm from the focal point is shown in *Figure 6.2 (a)* for OA and *(b)* corresponding cropped image for CA for S~ 0.40.

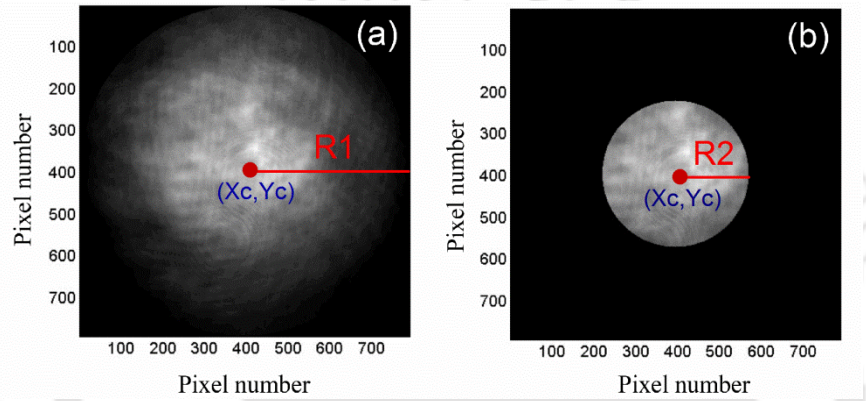

Figure 6.2: *CCD image of transmitted beam through film positioned at 20 mm from focal point:* ***(a)*** *open aperture and* ***(b)*** *closed aperture Z-scan for S~0.40.*

The transmitted intensity through the film was obtained by integrating the gray values of the recorded CCD image. In order to plot the transmission curve for OA as well as CA *Z*-scan from same set of CCD images a program in Matlab was developed. The flow chart for this program is illustrated in *Figure 6.3 and 6.4*. The input to the program was produced from the CCD. The program selects the images in sequence from the position '*z1'* to '*z2'*, the limits of scan range, in an interval of '*Δz'*, the step size. The coordinates for the center of the image are labeled as (Xc,Yc) and radius of the OA image for *z1* position is '*R1'* and that of CA is '*R2*', *Figure 6.2 (a) and (b)*, respectively. The flow chart for obtaining the integrated intensity as a function of '*z*' is illustrated in *Figure 6.3*. For a Gaussian beam, the aperture is circular and defined in the program accordingly. The flow chart in *Figure 6.4* describes the process to obtain the image with circular aperture from the recorded CCD image. After obtaining the integrated intensity

and hence the transmission, program automatically plots the transmitted intensity as a function of position for OA as well as CA, *Figure 6.5 and 6.6(b),* respectively. If height of the peak and depth of the valley are not equal then the radius '*R2'* for CA is changed manually in the program and is allowed to run again. This exercise is repeated till the satisfactorily result is obtained.

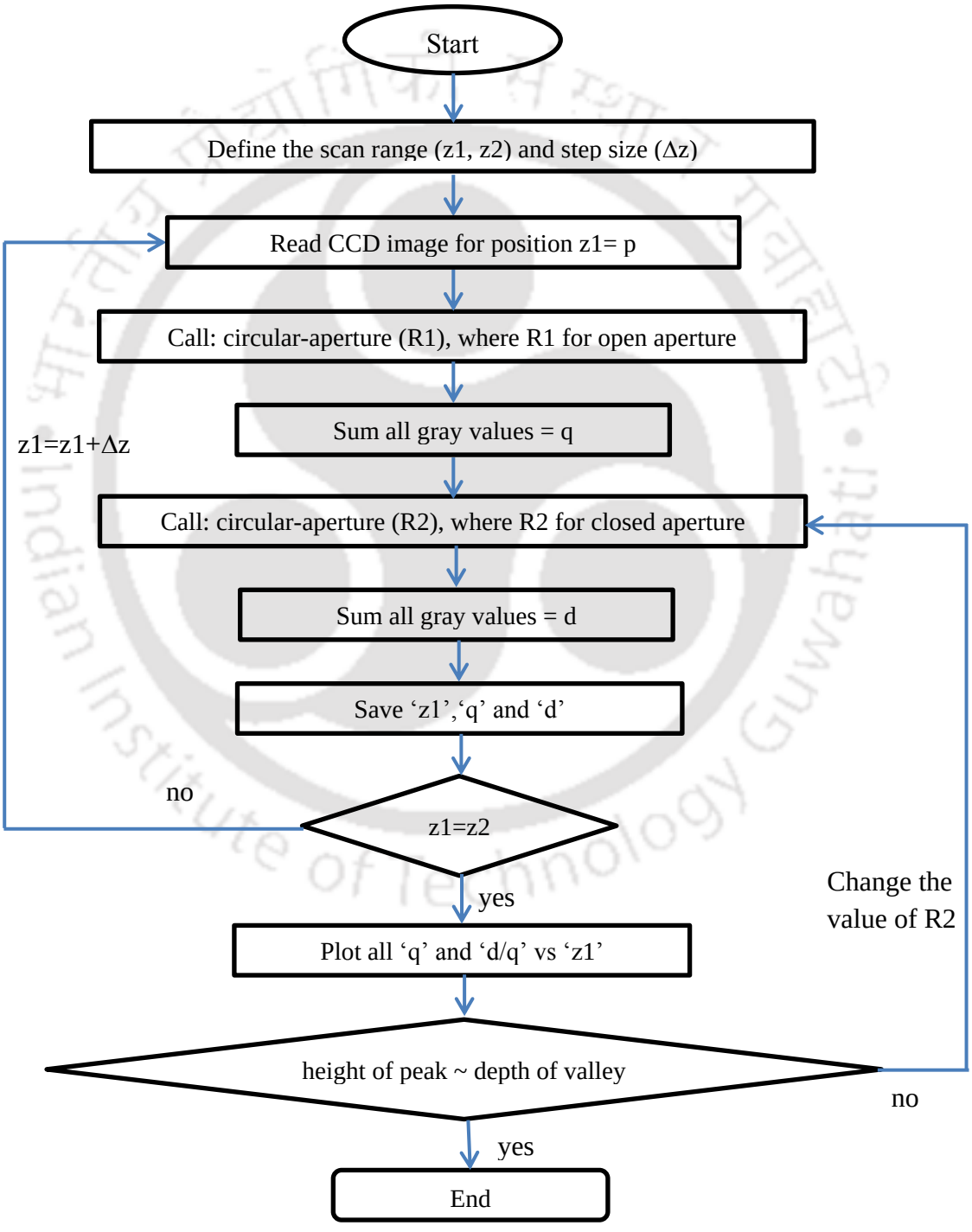

Figure 6.3: *Flow chart for obtaining OA and CA Z-scan transmission curve.*

Circular-aperture (R):

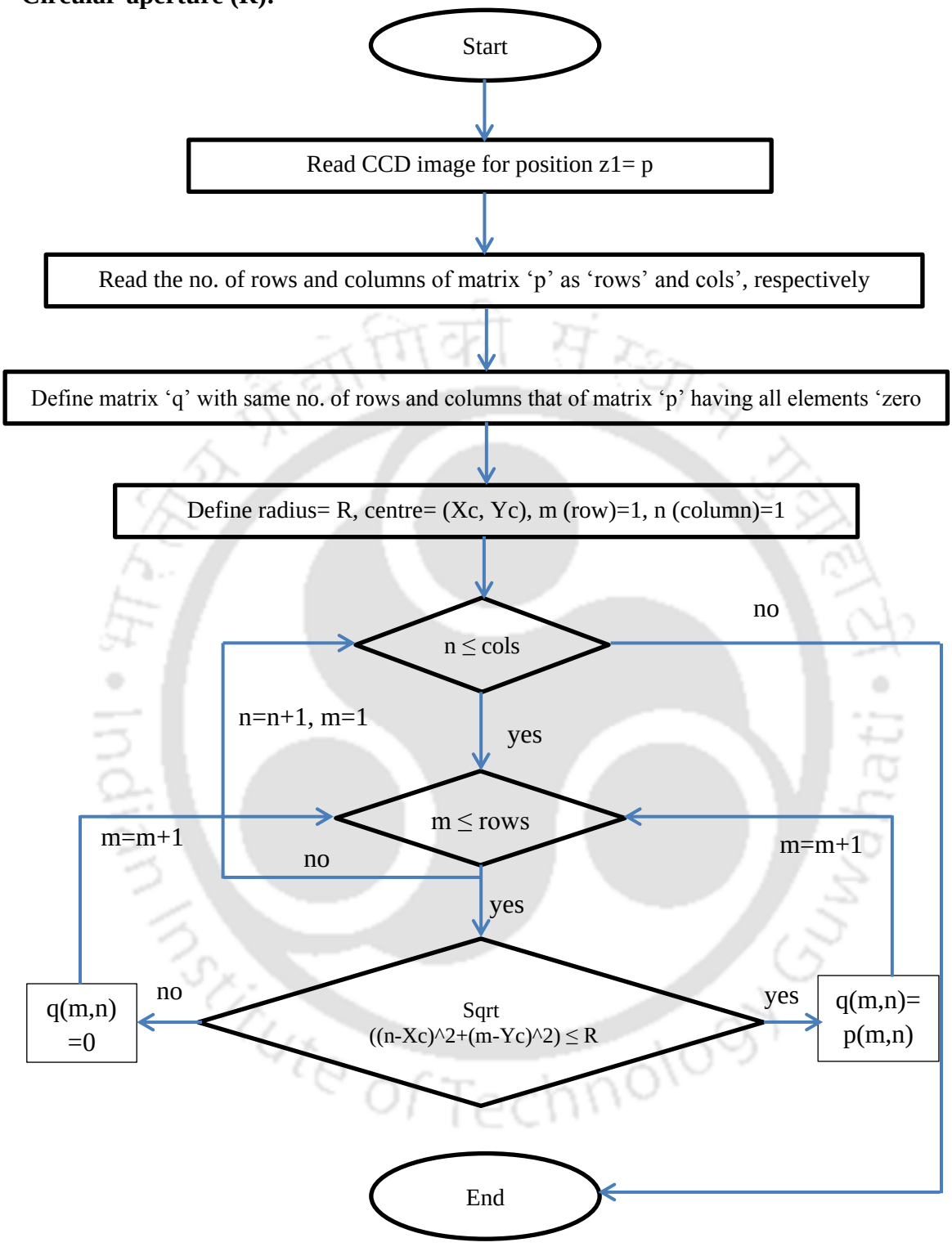

***Figure 6.4**: Flow chart for function: Circular aperture (R).*

6.2.1 Estimation of NLA coefficient

The transmitted intensity for OA was normalized with that of the far field intensity in order to obtain the normalized transmittance. *Figure 6.5* shows the normalized transmittance plot, T_{op}, as a function of film position '*z*' w.r.t. focal plane. The OA *Z*-scan profile shows valley around the focal position and symmetric to either side of it, indicating the reverse saturation absorption (RSA) effect in the film. The experimental data was fitted to *Equation (6.1)* [**8**]. The fitted data is marked as solid curve in *Figure 6.5.*

$$T_{op} = 1 - \frac{c}{1 + bz^2} \tag{6.1}$$

where, $c = \beta I_o L_{eff} / 2^{3/2}$, $b = 1/z_o^2$, z_o is Rayleigh length, I_o is the intensity of laser beam at the focus, β is the NLA coefficient and L_{eff} is the effective thickness of the carbon film which is given by *Equation (6.2).*

$$L_{eff} = \frac{1 - \exp(-\alpha L)}{\alpha} \tag{6.2}$$

The NLA coefficient was calculated from the fitted parameter '*c*' and found to be 8.22 ± 0.91 cm/W.

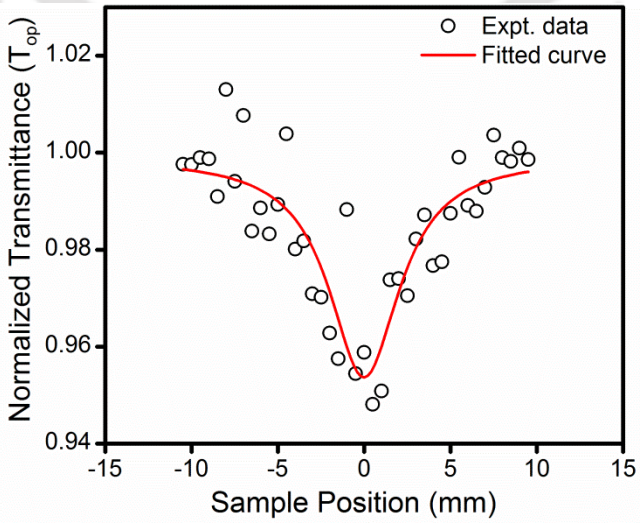

***Figure 6.5**: Normalized transmittance curve for carbon thin film for open aperture Z-scan.*

6.2.2 Optimization of aperture size for CA *Z*-scan

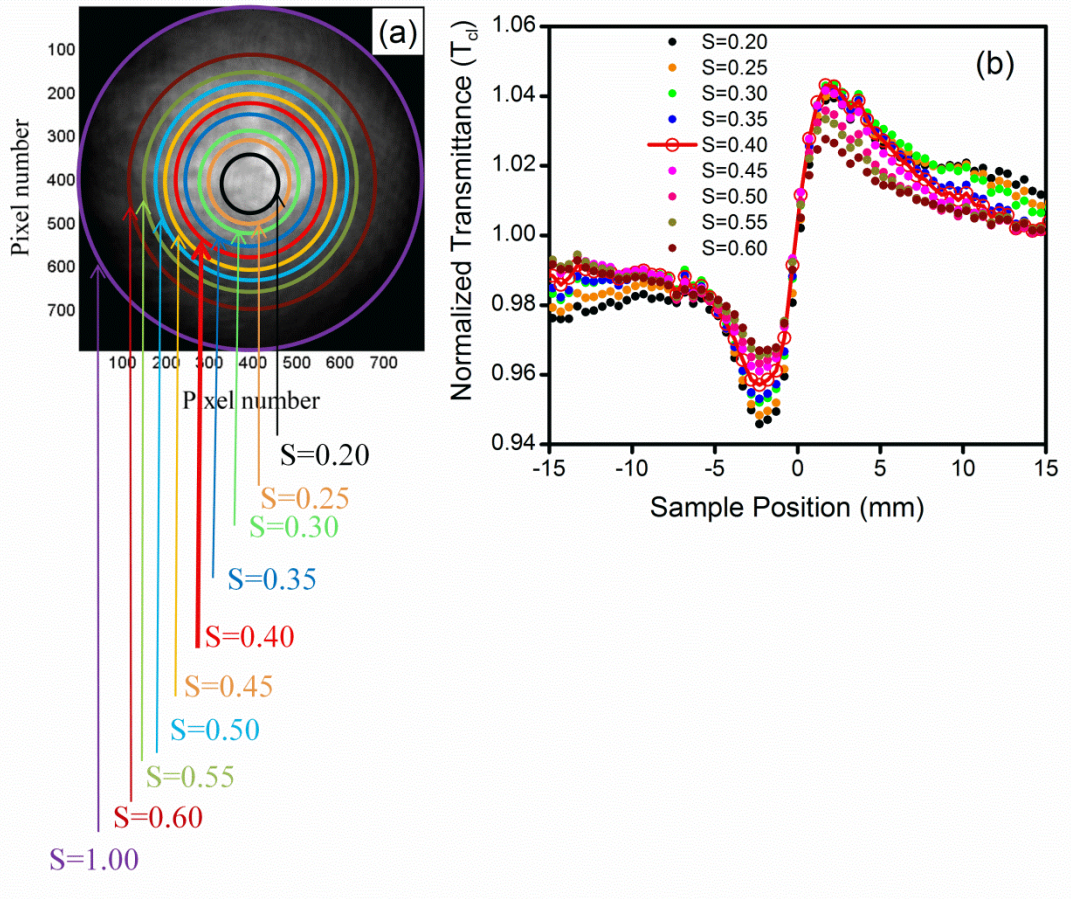

Figure 6.6: (a) *Marking of apertures on CCD image for various values of 'S' and* ***(b)*** *CA Z-scan curve for various aperture sizes; S~0.20, 0.25, 0.30, 0.35, 0.40, 0.45, 0.50, 0.55 and 0.60.*

In order to determine the NLR coefficient from CCD images with good accuracy, the contribution of NLA is to be subtracted by optimum aperture size such that the peak height and the depth of the valley are equal in CA *Z*-scan curve. For this, the aperture size '*S*' was varied in the range of 0.20 – 0.60 with a step size of 0.05 as marked in the CCD image of *Figure 6.6 (a)* and corresponding normalized transmittance, T_{cl}, for CA *Z*-scans are plotted in *Figure 6.6 (b)*. The symmetry of CA curve was estimated by the parameter ΔI_{pv} = *Δ(peak intensity)* - *Δ(valley intensity)*, where *Δ(peak intensity)* and *Δ(valley intensity)* are defined by

Δ(peak intensity) = peak intensity - 1

Δ(valley intensity) = 1 - valley intensity

The plot for ΔI_{pv} as a function of '*S*' is shown in *Figure 6.7*. The minimum value of ΔI_{pv} in the CA transmission curve is at $S \sim 0.40$, corresponds to best symmetry. Hence $S \sim 0.40$ is the optimum aperture size for the determination of the NLR coefficient.

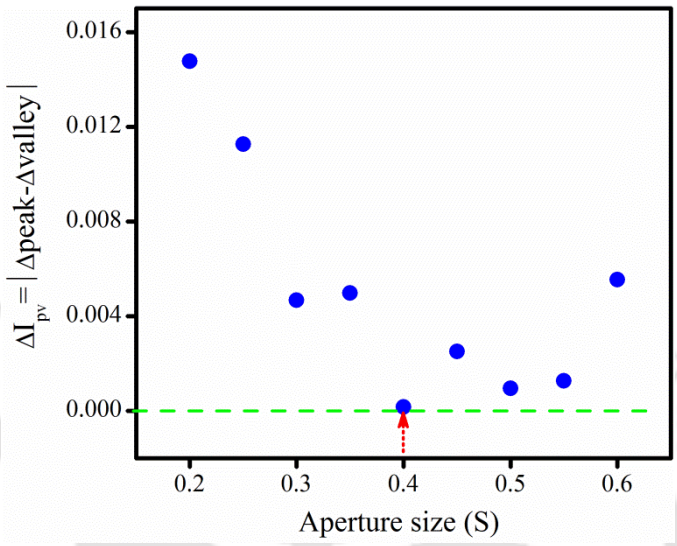

Figure 6.7: *ΔI_{pv} for CA transmission curve as a function of aperture size 'S'.*

6.2.3 Estimation of NLR coefficient

The transmitted intensity for CA was normalized with that of the far field intensity in order to obtain the normalized transmittance and shown in *Figure 6.8* for the optimum aperture S~0.40. It shows a prefocal minima (valley) followed by a postfocal maxima (peak), suggesting positive refractive nonlinearity. The experimental data was fitted to the normalized CA transmission profile [**9**], given by *Equation (6.3).*

$$T_{cl} = 1 + \frac{4az}{(1+bz^2)(9+bz^2)} \tag{6.3}$$

where, $a = 2\pi n_2 I_o L_{eff} / \lambda z_o$ and n_2 is the NLR coefficient.

The NLR coefficient 'n_2' of the carbon film is found to be $(1.40 \pm 0.10) \times 10^{-4}$ cm^2/W. The separation between the peak and valley position of normalized transmission, $\Delta z_{p\text{-}v}$ for CA *Z*-scan curve in the present case is 4.40 mm satisfying the *Equation (6.4)* for the third order optical nonlinearity [**9**].

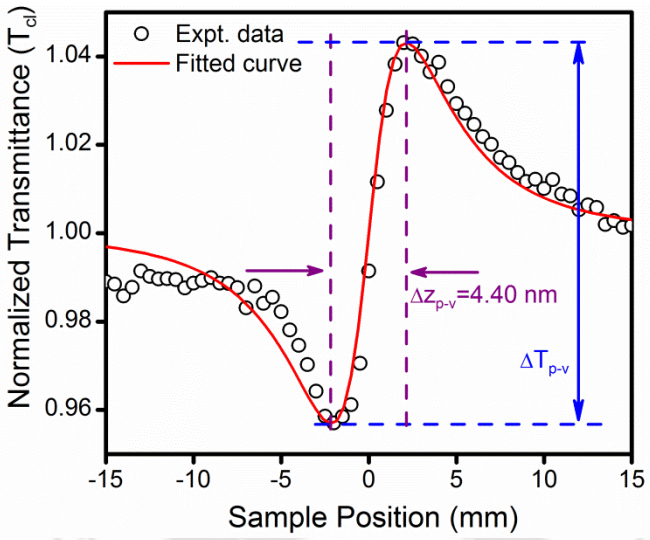

Figure 6.8: *Normalized transmittance curve for carbon film for closed aperture Z-scan, S~0.40.*

$$\Delta z_{p-v} = 1.7 z_o \tag{6.4}$$

where the Rayleigh length, z_o is 2.53 mm in the present case. In *Figure 6.8*, the peak and valley were symmetrically placed with respect to the focus, indicating the small phase distortion (i.e. $\Delta\phi_o < 1$) in the film. The phase distortion, $\Delta\phi_o$, due to the nonlinear refractive index at the focus ($z = 0$) is defined by *Equation (6.5)* [**9**].

$$\Delta\phi_o = \frac{2\pi n_2 I_o L_{eff}}{\lambda} = a z_o \tag{6.5}$$

The numerical value of $\Delta\phi_o$ was calculated from the parameter '*a*' of the fitted curve, *Figure 6.8*, and found to be ~0.22. Since the phase distortion is small, it can also be estimated using following relationship [**1, 9**]:

$$\Delta T_{p-v} \cong 0.406(1-S)^{0.25} |\Delta\phi_o| \tag{6.6}$$

where, ΔT_{p-v} is the difference in the normalized transmission of peak and valley. From *Figure 6.8*, the normalized peak transmission is 1.043 and that of valley is 0.957, thus ΔT_{p-v} = 0.086. From *Equation (6.6)*, $\Delta\phi_o$ was estimated and found to be ~0.24 for *S*~ 0.40, nearly same as that of obtained by *Equation (6.5)*. Thus, *S*~0.40 is the optimum value confirming the validity of the present *Z*-scan setup.

Conclusion

The conventional *Z*-scan setup was modified by replacing photodiode with CCD camera to measure the NLA and NLR coefficients of PLD carbon thin film in a single *Z*-scan. The implementation of the synthetic aperture in the present setup provides the option of selecting the aperture size more precisely for the optimization of closed *Z*-scan curve without physically repeating the experiment for the determination of NLR coefficient. The peak-valley separation is 1.7 times of the Rayleigh length of the focusing beam, confirming the presence of third order nonlinearity. The agreement of the theoretical and experimental value of phase distortion factor confirms the suitability of present simplified *Z*-scan setup using CCD camera via single scan only.

भारतीय प्रौद्योगिकी संस्थान गुवाहाटी
Indian Institute of Technology Guwahati

Bibliography

[**1**] M. Sheik-bahae, A.A. Said, E.W. Van Stryland, "High-sensitivity, single-beam n_2 measurements", *Optics Letters*, **14** (1989) 955-957.

[**2**] M.J. Moran, S. Chiao-Yao, R.L. Carman, "Interferometric measurements of the nonlinear refractive-index coefficient relative to CS_2 in laser-system-related materials", *IEEE Journal of Quantum Electronics*, **11** (1975) 259-263.

[**3**] S.R. Friberg, P.W. Smith, "Nonlinear optical glasses for ultrafast optical switches", *IEEE Journal of Quantum Electronics*, **23** (1987) 2089-2094.

[**4**] A. Owyoung, "Ellipse rotation studies in laser host materials", *IEEE Journal of Quantum Electronics*, **9** (1973) 1064-1069.

[**5**] A. Marcano O, H. Maillotte, D. Gindre, D. Métin, "Picosecond nonlinear refraction measurement in single-beam open Z scan by charge-coupled device image processing", *Optics Letters*, **21** (1996) 101-103.

[**6**] T. Xia, D.J. Hagan, M. Sheik-Bahae, E.W. Van Stryland, "Eclipsing Z-scan measurement of $\lambda/10^4$ wave-front distortion", *Optics Letters*, **19** (1994) 317-319.

[**7**] G. Tsigaridas, P. Persephonis, V. Giannetas, "Effects of nonlinear absorption on the Z-scan technique through beam dimension measurements", *Materials Science and Engineering: B*, **165** (2009) 182-185.

[**8**] E.W. Van Stryland, M. Sheik-Bahae, A.A. Said, D.J. Hagan, "Characterization of nonlinear optical absorption and refraction", *Progress in Crystal Growth and Characterization of Materials*, **27** (1993) 279-311.

[**9**] M. Sheik-Bahae, A.A. Said, T.H. Wei, D.J. Hagan, E.W. Van Stryland, "Sensitive measurement of optical nonlinearities using a single beam", *IEEE Journal of Quantum Electronics*, **26** (1990) 760-769.

भारतीय प्रौद्योगिकी संस्थान गुवाहाटी
Indian Institute of Technology Guwahati

Chapter 7

Optical nonlinearity in pulsed laser deposited DLC and graphitic thin films

Diamond-like carbon (DLC) thin film is a combination of sp^2 and sp^3 bonded carbon atoms in a random network whereas graphitic thin film is composed of sp^2 bonded carbon atoms only. In the sp^3 configuration, the adjacent carbon atoms are bonded strongly via σ bonds which give rise to a large band gap and hardness to the film. In the sp^2 configuration of carbon network, three of the valence electrons form trigonally σ bond and the remaining fourth electron forms a π bond. The π bond, lying normal to the plane of σ bonds and weaker in strength, is closer to the Fermi level. Thus, the presence of a π bond provides the small band gap and hence contributes towards the optical absorption and nonlinear optical (NLO) response [**1, 2**]. Carbon nanostructures in the form of carbon nanotubes, graphene, carbon black, onion-like carbon and fullerenes are sp^2 enriched and have been investigated for NLO response. The nonlinear absorption coefficient (β) and nonlinear refractive index coefficient (n_2) of single wall carbon nanotube via *Z*-scan technique using nanosecond laser at a wavelength of 532 nm are reported to be ~ 7.1×10^{-5} cm/W and ~ -1.2×10^{-9} cm^2/W, respectively [**3**]. Multiwall carbon nanotubes in ethylene glycol (0.4 mg/ml) has been reported to exhibit reverse saturation absorption effect under picosecond laser (532 nm) illumination and the corresponding value of β from *Z*-scan is observed to be 7.6×10^{-10} cm/W [**4**]. Its third order nonlinear susceptibility '$\chi^{(3)}$' via four wave mixing (nano as well pico second

laser) has also been documented by the same group [**4**]. The saturation absorption behaviour in few-layer graphene fabricated by chemical vapor deposition (CVD) under the irradiance of picosecond laser of wavelength 1550 nm is deomonstrated and the measured value of n_2 is reported to be ~10^{-7} cm^2/W [**5**]. The reverse saturation absorption is reported in linear carbon chains at a wavelength of 532 nm from nanosecond laser. Its experimentally measured value for β and n_2 are reported to be 2.1×10^{-10} cm/W and -3.0×10^{-15} cm^2/W, respectively [**6**]. The optical limiting in onion-like carbon, carbon black suspension, fullerenes and diamond nanoparticles have been reported in the literature [**2, 7-9**]. The various forms of nanostructured carbon enriched with sp^2 bond are being envisaged as a good candidate for NLO photonic device application. For the photonic applications, normally thin film geometry is preferred. The NLO properties of nanostructured carbon, particularly in the form of thin film can be assessed experimentally by various techniques. Among them, *Z*-scan technique has emerged as a very handy tool for these measurements [**10**]. In this technique, the sample is translated along the optic axis on either side of the focal plane of a lens. The transmitted beam through the sample is recorded as a function of its position '*z*' with respect to the focal plane. The nonlinear absorption (NLA) coefficient and nonlinear refractive index (NLR) coefficient can be obtained by open aperture (OA) and closed aperture (CA) *Z*-scan, respectively.

In this chapter, the measurement of the third order NLR coefficient of pulsed laser deposited (PLD) DLC and graphitic thin films using modified *Z*-scan setup is reported [**11**]. In the modified *Z*-scan setup, the photodiode of the conventional *Z*-scan is replaced by a charge-coupled device (CCD) camera, thereby improving the sensitivity of the technique [**12**]. The effect of deposition temperature, laser fluence and helium ambient on the NLR coefficient of the DLC thin films is presented. The effect of helium

gas on the NLR coefficient of graphitic thin films is also studied.

7.1 Experimental details

For NLO study, DLC films were deposited by the second harmonic of a Q-switched Nd:YAG laser and graphitic thin films were deposited using third harmonic of Q-switched Nd:YAG onto the glass substrate. The other deposition parameters for the fabrication of DLC and graphitic thin films are listed in *Table 4.1*.

The measurement of third order NLR coefficient of PLD films was performed using modified *Z*-scan setup. The schematic of experimental setup is shown in *Figure 2.4 (Chapter 2)* and discussed in detail in *Chapter 6*. Briefly, He-Ne laser was focused on the PLD thin film using a convex lens of focal length 50 mm. The thin films was scanned to 20 mm on either side of the focal point and the transmittted beam was imaged onto the CCD. The CA data was extracted, as discussed in *Chapter 6*, for the measurement of NLR coefficients.

7.2 NLR coefficient of DLC thin films deposited as a function of substrate temperature

To study the effect of substrate temperature on NLO properties, DLC films were deposited on fused silica substrate at RT, 300 °C, 500 °C and 750 °C under vacuum (~10^{-5} mbar) for 5 min at a laser fluence of ~5.0 J/cm^2, *Table 4.1, Chapter 4*. The linear absorption coefficient 'α' at a wavelength of 632.8 nm was estimated by fitting the ellipsometric data using modified Forouhi-Bloomer (mFB) model and is listed in *Table 4.2* [**13**]. The linear absorption coefficient of the carbon films was found to be increased with the increasing substrate temperature, as shown in *Figure 7.1*. The enhancement in the optical absorption in visible region is due to the increase in sp^2 content at higher substrate temperature as also observed in Raman spectra, *Figure 4.4 (b), Chapter 4*. With

increase in sp^2 content, the total number of states in the energy gap increases thereby increasing the optical absorption [**2**].

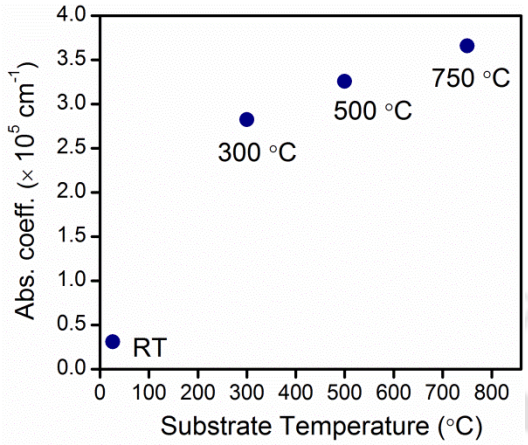

Figure 7.1: *Linear absorption coefficient of DLC thin films at 632.8 nm as a function of substrate temperature.*

The NLR coefficients of the PLD carbon films were measured using *Z*-scan technique [**14**]. The intensity of the He-Ne laser at the focus was estimated to be ~ 7.46 × 10^3 W/cm^2. Initially, the *Z*-scan was performed on the bare fused silica substrate and its normalized transmission spectra for OA as well as CA *Z*-scan is shown in *Figure 7.2*. There is hardly any signature of NLO behaviour at this laser intensity.

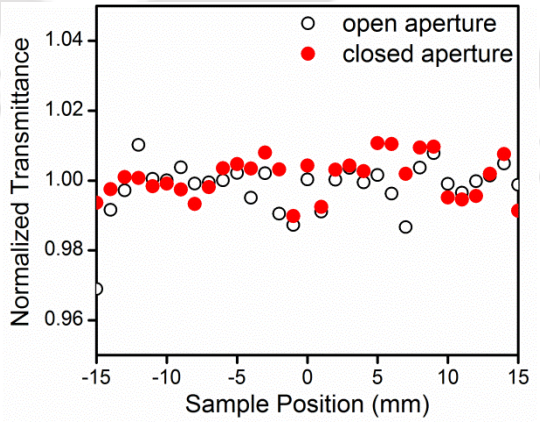

Figure 7.2: *Normalized open aperture and closed aperture Z-scan transmittance curve for fused silica substrate.*

Figure 7.3 (a-d) shows the normalized transmittance for CA *Z*-scan as a function of film position w.r.t. the focal plane for carbon films deposited at RT, 300 °C, 500 °C

and 750 °C, respectively. The experimental data points were fitted to the *Equation (6.3), Chapter 6* for CA *Z*-scan [**15**].

The CA transmittance curves for DLC thin films, *Figure 7.3*, depict minima (valley) followed by a maxima (peak), suggesting the presence of positive nonlinearity in the carbon film [**15**]. The positive nonlinearity in the film results in self-focusing. The

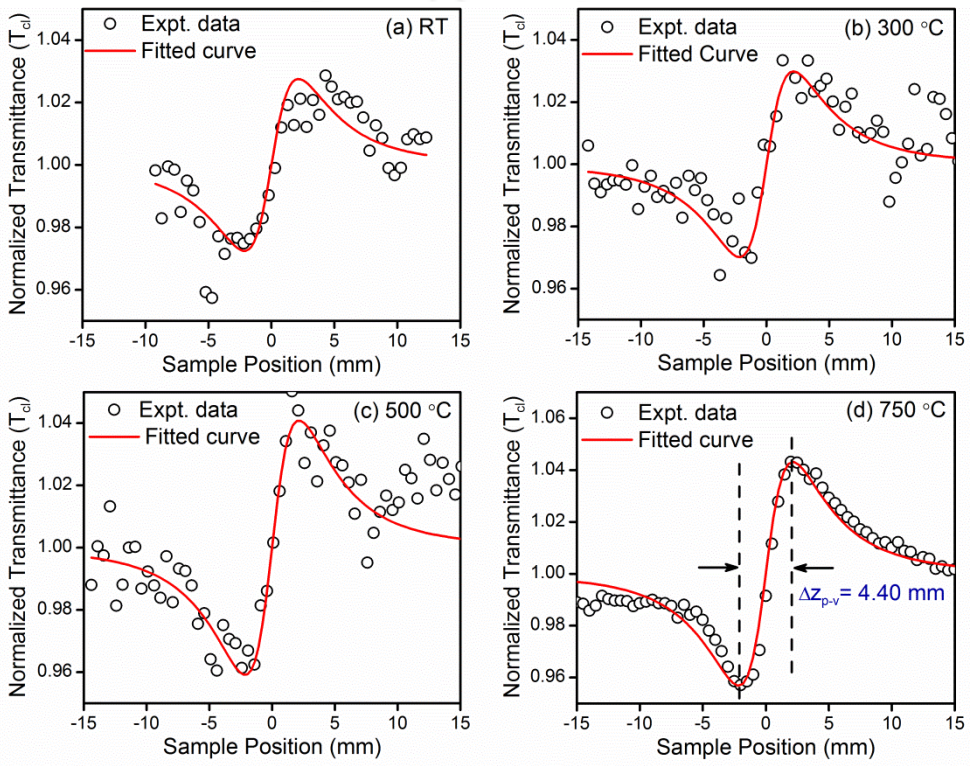

Figure 7.3: *Normalized closed aperture Z-scan transmittance curve for DLC thin films deposited at* ***(a)*** *RT,* ***(b)*** *300 °C,* ***(c)*** *500 °C and* ***(d)*** *750 °C.*

variation of NLR coefficient as a function of deposition temperature is shown in *Figure 7.4*. For the film deposited at RT, the measured NLR coefficient is $(6.08 \pm 0.75) \times 10^{-4}$ cm^2/W. The optical nonlinearity in amorphous carbon films is due to the sp^2 hybridized carbon atoms only. The sp^2 hybridized domain in amorphous carbon film provides delocalized electrons associated with carbon atoms in π bonds. The weakly bonded electrons can easily be displaced relatively to larger extent on the exposure of laser beam which leads to enhanced polarizability and hence exhibit strong nonlinearity. The NLR

coefficient was found to be increasing with the deposition temperature and for the film deposited at 750 °C, it was observed to be (1.69 ± 0.13) × 10^{-3} cm^2/W. The increase in the NLR coefficient of the film with the increase in substrate temperature is due to the increase in sp^2 bonded carbon atoms as indicated by Raman results, *Figure 4.4 (b), Chapter 4*.

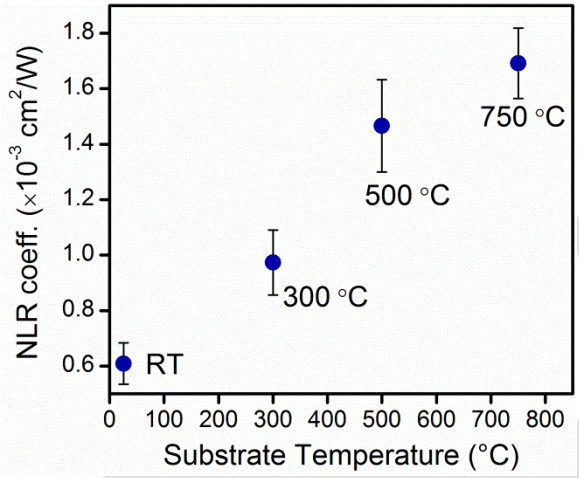

Figure 7.4: *NLR coefficient of DLC thin films as a function of substrate temperature.*

The order of nonlinearity in the film can be determined from the separation between the peak and valley position of CA transmittance curve. The peak-valley separation of normalized CA transmission, $\Delta z_{p\text{-}v}$, for the film deposited at 750 °C was found to be 4.40 mm, as marked in *Figure 7.3 (d)*, which is satisfying the condition for third order nonlinearity, given by *Equation (6.4), Chapter 6* [**15**].

The measured value of Rayleigh length (z_o) for He-Ne laser beam focused by a convex lens of focal length of 50 mm (*Z*-scan setup, *Figure 2.4*) is 2.53 mm and hence for third order nonlinearity, $\Delta z_{p\text{-}v}$ should be 4.30 mm. For all the four samples, the measured value of $\Delta z_{p\text{-}v}$ was found to be in the range of 4.30 - 4.50 mm, confirming the third order optical nonlinearity in DLC thin films. The slight variation in the value of $\Delta z_{p\text{-}v}$ could be due to the thermo-optical effect induced in films as the illumination time from sample to sample might have varied during the measurements [**16**].

7.3 NLR coefficeint of DLC thin films deposited as a function of laser fluence

The effect of laser fluence on NLR coefficeint of DLC films deposited in vacuum as well as in helium gas ambient is studied. The laser fluence was varied from 5.0 J/cm^2 to 11.7 J/cm^2 for the film deposited in the background pressure of ~10^{-5} mbar whereas in case of helium gas ambient the laser fluence was varied from 10.0 J/cm^2 to 15.0 J/cm^2, *Table 4.1, Chapter 4*.

7.3.1 NLR coefficient of DLC thin films deposited in vacuum

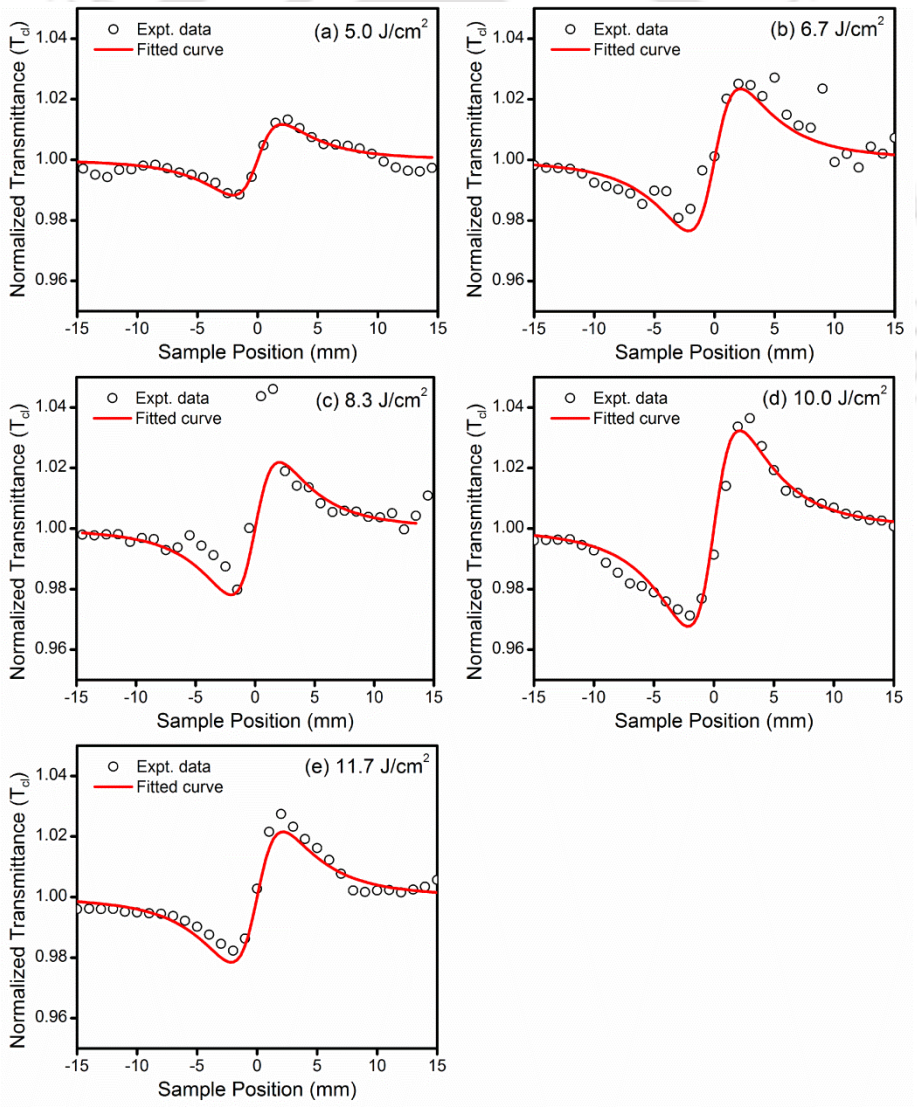

Figure 7.5: *Normalized closed aperture Z-scan transmittance curve for DLC thin films deposited at a base pressure of ~10^{-5} mbar and laser fluence of* ***(a)*** *5.0 J/cm^2,* ***(b)*** *6.7 J/cm^2,* ***(c)*** *8.3 J/cm^2,* ***(d)*** *10.0 J/cm^2 and* ***(e)*** *11.7 J/cm^2.*

Figure 7.5 (a-e) shows the normalized transmittance for CA *Z*-scan for DLC films deposited at laser fluence of 5.0 J/cm^2, 6.7 J/cm^2, 8.3 J/cm^2, 10.0 J/cm^2 and 11.7 J/cm^2, respectively under the base pressure of ~10^{-5} mbar at RT. The linear absorption coefficient was estimated using mFB model and listed in *Table 4.4 (Chapter 4)*. The normalized CA *Z*-scan data was fitted to the *Equation (6.3) of Chapter 6* and shown by the solid curve in *Figure 7.5*. The calculated NLR coefficients obtained from fitted parameter for DLC films are plotted in *Figure 7.6* as a function of laser fluence. The value of NLR coefficient for the film deposited at laser fluence of 5.0 J/cm^2 is (1.49 ± 0.12) × 10^{-4} cm^2/W which is slightly lower compared to that of the films deposited at higher laser fluence. This could be due to comparatively low film thickness, *Table 4.4 (Chapter 4).* As variation in the ratio of sp^3/sp^2 bonding in the DLC films deposited in this range of laser fluence is marginal, *Table 4.3 (chapter 4)*, and hence the variation in NLR coefficients is not large.

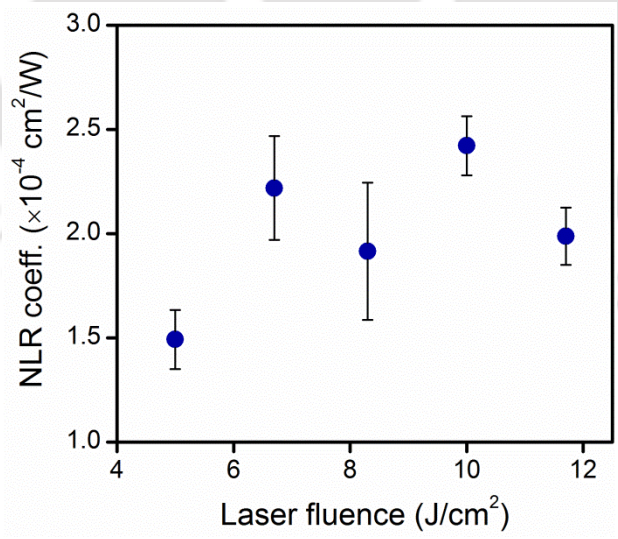

Figure 7.6: *NLR coefficient of DLC thin films as a function of laser fluence.*

7.3.2 NLR coefficient of DLC thin films deposited at helium pressure of 0.05 mbar

Figure 7.7 (a-d) shows the normalized transmittance for CA *Z*-scan for DLC thin films deposited at a helium pressure of 0.05 mbar and laser fluence of 10.0 J/cm^2, 11.7

J/cm^2, 13.3 J/cm^2 and 15.0 J/cm^2, respectively. The experimental data points were fitted to *Equation (6.3) of Chapter 6* and the calculated NLR coefficients are listed in *Table 7.1*. As the DLC films deposited at 0.05 mbar and in this range of laser fluence possess

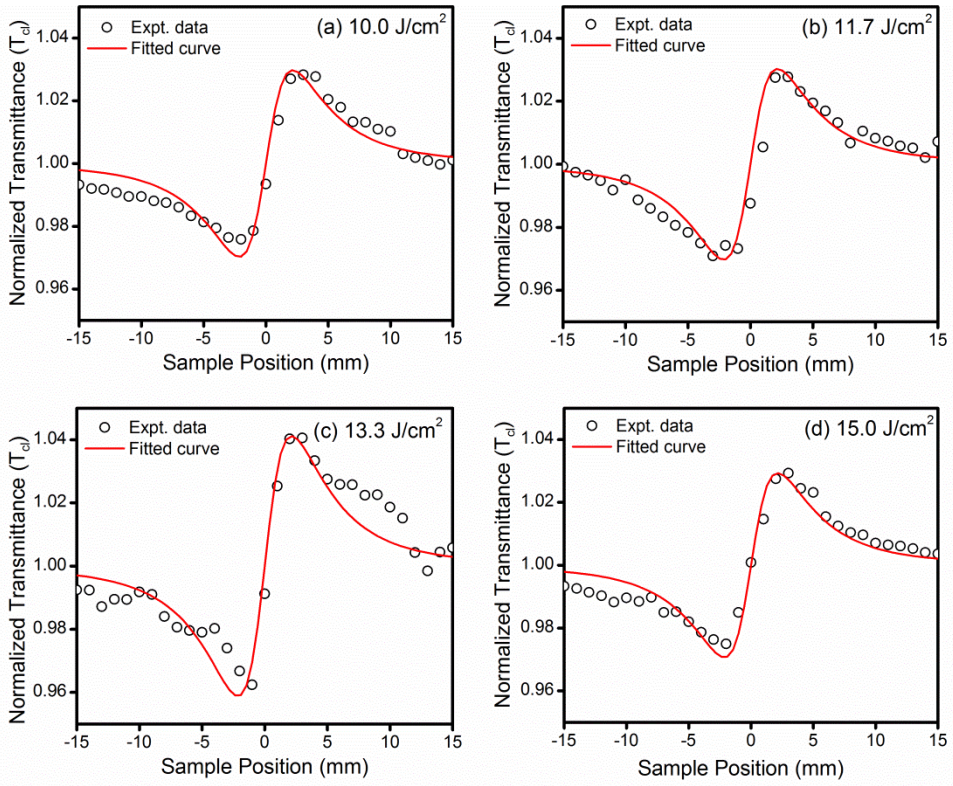

Figure 7.7: *Normalized closed aperture Z-scan transmittance curve for DLC thin films deposited at 0.05 mbar of helium pressure and laser fluence of* ***(a)*** *10.0 J/cm^2,* ***(b)*** *11.7 J/cm^2,* ***(c)*** *13.3 J/cm^2 and* ***(d)*** *15.0 J/cm^2.*

Table 7.1: *NLR coefficient of DLC thin films deposited at 0.05 mbar of helium pressure as a function of laser fluence*

Laser fluence (J/cm^2)	**Thickness (nm)**	**NLR coefficient (×10^{-4} cm^2/W)**
10.0	121	3.57 ± 0.25
11.7	140	3.79 ± 0.26
13.3	120	3.21 ± 0.25
15.0	107	2.40 ± 0.18

similar properties as observed in Raman and SE measurements (*Section 4.2.3 of Chapter 4*), thus not much variation in NLR coefficient is expected. The variation in the values of NLR coefficient of all these films are marginal. In this set of samples, optical absorption

is large for the films having large thickness (*Table 4.6 and Table 4.9 of Chapter 4*) and hence the variation in NLR coefficient is also in accordance to the variation in the film thickness.

7.4 NLR coefficient of DLC thin films deposited as a function of helium pressure

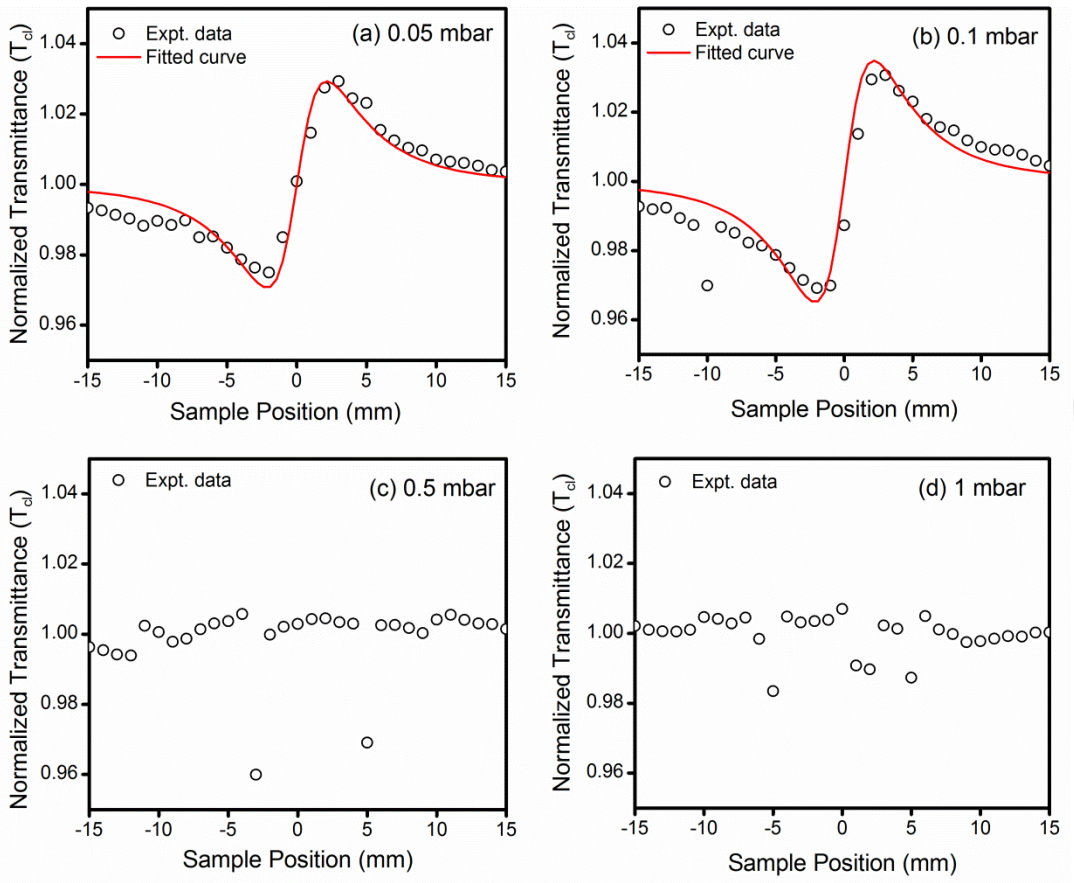

Figure 7.8: *Normalized closed aperture Z-scan transmittance curve for DLC thin films deposited at a laser fluence of 15.0 J/cm^2 and helium pressure of* ***(a)*** *0.05 mbar,* ***(b)*** *0.1 mbar,* ***(c)*** *0.5 mbar and* ***(d)*** *1 mbar.*

Figure 7.8 (a-d) shows the normalized transmittance for the CA *Z*-scan curve for DLC thin films deposited at a laser fluence of 15.0 J/cm^2 and helium pressure of 0.05 mbar, 0.1 mbar, 0.5 mbar and 1 mbar, respectively. The film deposited at a helium pressure of 0.05 mbar exhibited the NLR coefficient of (2.40 ± 0.18) × 10^{-4} cm^2/W which increased to (3.56 ± 0.26) × 10^{-4} cm^2/W for the film deposited at 0.1 mbar of

helium pressure. The small increase in the NLR value may be due to the increased thickness of the film, *Table 7.2*. The films deposited at the helium pressure of 0.5 mbar and 1 mbar didn't display any peak-valley structure, *Figure 7.8 (c-d)*. Those films consist of higher sp^3 bonding of carbon atoms as obtained from Raman and SE results (*Section 4.2.3 of Chapter 4*) and hence not expected to exhibit any signature of optical nonlinearity at this laser intensity.

Table 7.2: *NLR coefficient of DLC thin films deposited at a laser fluence of 15.0 J/cm^2 as a function of helium pressure*

Helium pressure (mbar)	Thickness (nm)	NLR coefficient (×10^{-4} cm^2/W)
0.05	107	2.40 ± 0.18
0.1	220	3.56 ± 0.26
0.5	44	--
1	34	--

7.5 NLR coefficient of graphitic thin films deposited as a function of helium pressure

Figure 7.9 (a-e) shows the normalized CA *Z*-scan curve for the graphitic thin films deposited at a base pressure of ~10^{-5} mbar and helium pressure of 0.1 mbar, 1 mbar, 5 mbar and 10 mbar, respectively, deposited at a substrate temperature of 750 °C. The film deposited at ~10^{-5} mbar is highly amorphous as observed in Raman measurement, *Section 4.3 of Chapter 4*. In case of amorphous structure of graphitic film, the displacement of the delocalized electrons is more in the presence of high intensity of laser beam due to short range ordering of sp^2 bonded carbon atoms. This leads to increase in polarizability and hence higher value of NLR coefficient was obtained. With the increase in helium pressure, films became structurally ordered leading to decrease in polarization for the same intensity of laser beam and hence decrease in NLR coefficient

was observed, *Table 7.3* [**17, 18**].

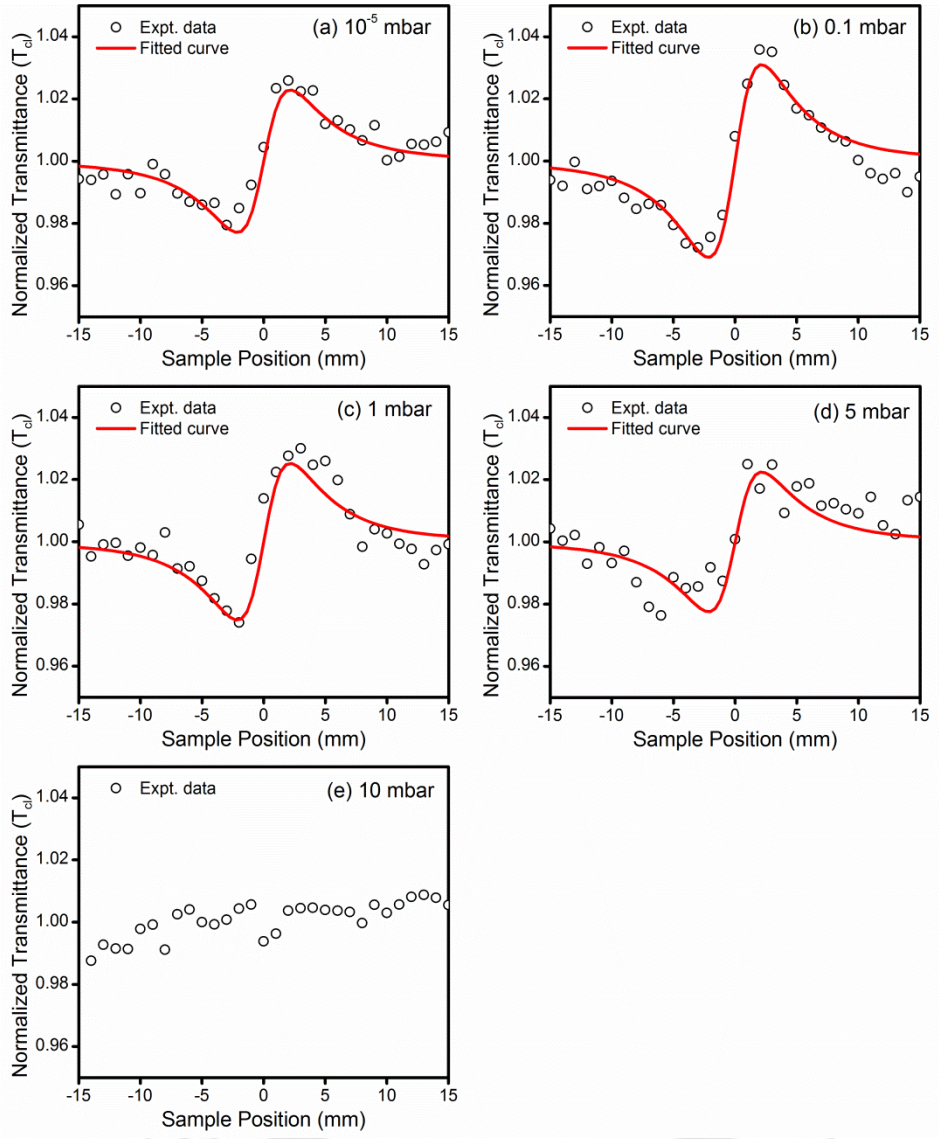

Figure 7.9: *Normalized closed aperture Z-scan transmittance curve for graphitic thin films deposited at a laser fluence of 5.0 J/cm^2 and pressure of* ***(a)*** *10^{-5} mbar,* ***(b)*** *0.1 mbar helium,* ***(c)*** *1 mbar helium,* ***(d)*** *5 mbar helium and* ***(e)*** *10 mbar helium.*

Table 7.3: *NLR coefficient of graphitic thin films as a function of deposition pressure*

Deposition pressure	**NLR coefficient ($\times 10^{-4}$ cm^2/W)**
10^{-5} mbar	17.94 ± 2.19
0.1 mbar helium	7.61 ± 0.81
1 mbar helium	4.75 ± 0.56
5 mbar helium	4.88 ± 0.74
10 mbar helium	--

Conclusion

The effect of substrate temperature, laser fluence and helium pressure on the NLO property of PLD carbon thin films is presented in this chapter. The NLR coefficients of PLD carbon thin films were measured by modified *Z*-scan setup using CCD camera. With the increase in the deposition temperature, films showed the increase in sp^2 bonding which increases the NLR coefficient. As the laser fluence has hardly any significant effect on the sp^3/sp^2 fraction of DLC film, thus the variation in NLR coefficient of DLC films as a function of laser fluence was observed to be marginal. The DLC thin films deposited at helium pressure of 0.5 mbar and 1 mbar and the laser fluence of 15.0 J/cm^2 possess higher sp^3 fraction of carbon bonded atoms, also the film is higly transparent, making it difficult to observe the nonlinear signature in these films. In case of graphitic thin films, all the samples exhibited nearly 100% sp^2 bonded carbon atoms and thus displayed relatively large optical nonlinearity compared to that of the DLC films. The increase in helium pressure increases the structural order of the film which decreases the change in polarization on the exposure of laser and hence reducing the NLR coefficeint with the increase in helium pressure. The transmittance curve for CA *Z*-scan measurement, for all DLC and graphitic thin films, showed a valley followed by a peak indicating the nonlinearity in the PLD carbon thin films is due to the self-focusing. The measured value of $\Delta z_{p\text{-}v}$ from fitted transmitted profile of CA *Z*-scan curve is 1.7 times of the Rayleigh length of the focusing beam, which confirms the presence of third order nonlinearity.

भारतीय प्रौद्योगिकी संस्थान गुवाहाटी
Indian Institute of Technology Guwahati

Bibliography

[**1**] J. Robertson, "Diamond-like amorphous carbon", *Materials Science and Engineering R*, **37** (2002) 129-281.

[**2**] E. Koudoumas, O. Kokkinaki, M. Konstantaki, S. Couris, S. Korovin, P. Detkov, V. Kuznetsov, S. Pimenov, V. Pustovoi, "Onion-like carbon and diamond nanoparticles for optical limiting", *Chemical Physics Letters*, **357** (2002) 336-340.

[**3**] J. Seo, S. Ma, Q. Yang, L. Creekmore, R. Battle, M. Tabibi, H. Brown, A. Jackson, T. Skyles, B. Tabibi, S. Jung, M. Namkung, "Third-order optical nonlinearities of singlewall carbon nanotubes for nonlinear transmission limiting application", *Journal of Physics: Conference Series*, **38** (2006) 37-40.

[**4**] K.C. Jena, P.B. Bisht, M.M. Shaijumon, S. Ramaprabhu, "Study of optical nonlinearity of functionalized multi-wall carbon nanotubes by using degenerate four wave mixing and *Z*-scan techniques", *Optics Communications*, **273** (2007) 153-158.

[**5**] H. Zhang, S. Virally, Q. Bao, L. Kian Ping, S. Massar, N. Godbout, P. Kockaert, "*Z*-scan measurement of the nonlinear refractive index of graphene", *Optics Letters*, **37** (2012) 1856-1858.

[**6**] E. Fazio, F. Neri, S. Patanè, L. D'Urso, G. Compagnini, "Optical limiting effects in linear carbon chains", *Carbon*, **49** (2011) 306-310.

[**7**] D. Vincent, S. Petit, S.L. Chin, "Optical limiting studies in a carbon-black suspension for subnanosecond and subpicosecond laser pulses", *Applied Optics*, **41** (2002) 2944-2946.

[**8**] L.W. Tutt, T.F. Boggess, "A review of optical limiting mechanisms and devices using organics, fullerenes, semiconductors and other materials", *Progress in Quantum Electronics*, **17** (1993) 299-338.

[**9**] V. Vanyukov, T. Mogileva, G. Mikheev, A. Puzir, V. Bondar, Y. Svirko, "Size effect on the optical limiting in suspensions of detonation nanodiamond clusters", *Applied Optics*, **52** (2013) 4123-4130.

[**10**] M. Sheik-bahae, A.A. Said, E.W. Van Stryland, "High-sensitivity, single-beam n_2 measurements", *Optics Letters*, **14** (1989) 955-957.

[**11**] I. Kumar, A. Khare, "Modified Z-scan set-up using CCD for measurement of optical nonlinearity in PLD carbon thin film", *Optics & Laser Technology*, **77** (2016) 51-54.

[**12**] G. Tsigaridas, M. Fakis, I. Polyzos, P. Persephonis, V. Giannetas, "*Z*-scan technique through beam radius measurements", *Applied Physics B*, **76** (2003) 83-86.

[**13**] Y. Liu, G. Xu, C. Song, W. Weng, P. Du, G. Han, "Modification on Forouhi and Bloomer model for the optical properties of amorphous silicon thin films", *Thin Solid Films*, **515** (2007) 3910-3913.

[**14**] E.W. Van Stryland, M. Sheik-Bahae, A.A. Said, D.J. Hagan, "Characterization of nonlinear optical absorption and refraction", *Progress in Crystal Growth and Characterization of Materials*, **27** (1993) 279-311.

[**15**] M. Sheik-Bahae, A.A. Said, T.H. Wei, D.J. Hagan, E.W. Van Stryland, "Sensitive measurement of optical nonlinearities using a single beam", *IEEE Journal of Quantum Electronics*, **26** (1990) 760-769.

[**16**] U. Tripathy, P.B. Bisht, "Influence of pulsed and cw pumping on optical nonlinear parameters of laser dyes probed by a closed-aperture *Z*-scan technique", *Journal of the Optical Society of America B*, **24** (2007) 2147-2156.

[**17**] B. Anand, S.R. Krishnan, R. Podila, S. Siva Sankara Sai, A.M. Rao, R. Philip, "The role of defects in the nonlinear optical absorption behavior of carbon and ZnO nanostructures", *Physical Chemistry Chemical Physics*, **16** (2014) 8168-8177.

[**18**] Z.-B. Liu, Z.-J. Zhou, Z.-R. Li, Q.-Z. Li, F.-Y. Jia, J.-B. Cheng, C.-C. Sun, "What is the role of defects in single-walled carbon nanotubes for nonlinear optical property?", *Journal of Materials Chemistry*, **21** (2011) 8905-8910.

Chapter 8

Conclusion

The fabrication of diamond-like carbon (DLC) and graphitic thin films and few- and multi- layer graphene via pulsed laser deposition (PLD) technique is reported in the present thesis. The second harmonic of a Q-switched Nd:YAG laser was focused onto a graphite target to fabricate DLC thin films and graphene layers whereas the graphitic thin films were deposited using the third harmonic of a Q-switched Nd:YAG laser. The structural information and sp^3/sp^2 content in DLC films were analysed via micro-laser Raman spectrometer. Atomic force microscope (AFM) was used to study the surface morphology. The graphene samples were subjected to field emission scanning electron microscope (FESEM) and transmission electron microscope (TEM) to study the ordering of graphene layers. The linear optical properties of DLC and graphitic thin films were measured by spectroscopic ellipsometer. Transmission spectra in UV-Visible-NIR range were also recorded for the estimation of optical band gap of DLC films. The nonlinear optical properties of pulsed laser deposited DLC and graphitic thin films were investigated via in-house assembled modified *Z*-scan setup using charge-coupled device (CCD) camera.

While recording the Raman spectrum of DLC films, excessive intensity of the excitation laser brings some temporary or permanent changes into focal region due to the laser heating. Therefore, the effect of laser power on the Raman spectrum in the intensity from 11 kW/cm^2 to 382 kW/cm^2 was undertaken. A marginal effect was observed on the Raman spectra for the excitation laser intensity upto 114 kW/cm^2 which was not

permanent. This particular film (deposited at RT and laser fluence of 5.0 J/cm^2 on corning glass) showed a broad band around 800-2000 cm^{-1} in which D and G band were merged together. Beyond the laser intensity of 114 kW/cm^2, the emergence of G and D bands distinctly was observed. This implies the modification of sp^2 clusters and conversion of sp^3 to sp^2 bonding. The structural modification in the focal region of the film surface is due to the excessive focal heating. The permanent nature of structural changes in DLC film while recording the Raman spectra at high laser intensity was confirmed further by deliberately annealing the film with laser in the intensity range of 127-382 kW/cm^2 for 5 min and then recording the Raman spectra at a laser intensity of 114 kW/cm^2.

DLC thin films were deposited over a broad range of deposition parameters; substrate temperature, laser fluence and helium gas pressure. The DLC film deposited at room temperature (RT) in vacuum (~10^{-5} mbar) at laser fluence of ~5.0 J/cm^2 was found to be rich in sp^3 bonded carbon atoms which was indicated by the appearance of a broad Raman band centred at ~1550 cm^{-1} with a broad tail extending towards lower wavenumber. The evolution of the distinct D and G bands with the increase in substrate temperature signifies the formation of graphitic domains. The sp^3 content, estimated from the dispersion of G band, in the DLC film deposited at RT was found to be ~68% which was decreased to ~25% and ~10% for the films deposited at the substrate temperature of 300 °C and 500 °C, respectively. The nearly zero dispersion of the G band for the film deposited at 750 °C indicated the presence of only sp^2 bonding. The variation in sp^3 content of the DLC films as a function of laser fluence (used to deposit the PLD films) in the range of 5.0-11.7 J/cm^2 was marginal. At higher laser fluence, films exhibited the deposition of large particulates ejected from the graphite target. To overcome this, helium gas was introduced into the chamber in the pressure range of

0.05 - 1 mbar for deposition and at each value of these helium pressure, the laser fluence was varied from 10.0 J/cm^2 to 15.0 J/cm^2. The effect of helium pressure was observed to be well pronounced compared to that of laser fluence. For the laser fluence of 15.0 J/cm^2, the sp^3 content of the film deposited at 0.05 mbar of helium pressure was ~68% which was increased to ~73% and ~83% with the increase in helium pressure of 0.1 mbar and 0.5 mbar, respectively. The optical band gap obtained by ellipsometric data, using a modified Forouhi-Bloomer model, was found to increase from 1.43 eV to 3.42 eV with the increase in helium pressure from 0.05 mbar to 1 mbar, respectively, indicating an enhancement in sp^3 bonded carbon atoms as also confirmed by Raman measurement. The DLC films were found to be hydrogen-free as indicated by the absence of clear signature of bands around 3000 cm^{-1} in Fourier transform infrared transmission spectra.

The carbon film deposited at a substrate temperature of 750 °C under vacuum (~10^{-5} mbar) was found to be rich in sp^2 bonding of carbon atoms as confirmed by the distinct appearance of G and D bands in Raman spectrum. The structural order of the film was improved in the presence of helium gas ambient which was indicated by the narrowing of G band from 90 cm^{-1} to 46 cm^{-1} and D band from 139 cm^{-1} to 39 cm^{-1} with the increase in helium pressure from 0.1 mbar to 10 mbar, respectively. The ordered graphitic structure was further confirmed by the appearance of 2D, D+D' and 2D' bands distinctly in the range of 2400-3300 cm^{-1} for the film prepared at 10 mbar of helium pressure. The graphitic films were also subjected to the ellipsometric measurement for the estimation of optical constants and the results were found in agreement with that of the Raman measurement.

Few- and multi-layer graphene on glass substrate under oxygen ambient were obtained in a single step without using any catalyst, one of the major advantages of PLD technique. The formation of graphene layer was confirmed by the line shape of second-

order Raman band (2D band). The separation between the two sub-peaks in 2D band for the film deposited at RT was observed to be 32.25 cm^{-1} indicating the presence of ~10 layers of graphene. This sub-peak separation was decreased to 28.21 cm^{-1} for graphene layers deposited at the substrate temperature of 700 °C which corresponds to 4-5 layers. The formation of few-layer graphene was further confirmed by increase in I_{2D}/I_G ratio from 0.33 to 0.47 with the increase in substrate temperature from RT to 700 °C, respectively. The corresponding decrease in I_D/I_G ratio from 0.31 to 0.13 reflects the decrease in defects and hence the formation of ordered graphene layers at higher temperature. The hexagonal phase of graphene was observed by selected area electron diffraction (SEAD) pattern with lattice *d*-spacing of ~0.33 nm measured from ultra-high resolution TEM image in confirmation with the existing literature.

To study the NLO behaviour of pulsed laser deposited DLC and graphitic thin films, the conventional *Z*-scan setup was modified by replacing the photodiode detector with CCD camera. Thus, in a single scan both, open aperture (OA) and closed aperture (CA) data can be extracted from the same set of images. A program in Matlab was developed for the appropriate selection of aperture for CA *Z*-scan and the analysis of these data.

The nonlinear refractive index (NLR) coefficient for DLC films, obtained by modified *Z*-scan setup, was found to increase from $(6.08 \pm 0.75) \times 10^{-4}$ cm^2/W to $(1.69 \pm 0.13) \times 10^{-3}$ cm^2/W with the deposition temperature from RT to 750 °C, respectively. The higher substrate temperature increased the sp^2 bonding of carbon atoms in films which provides more π-bonds and thereby increasing the NLR coefficient at elevated substrate temperature. The laser fluence has hardly any effect on the sp^3/sp^2 fraction of carbon atoms in DLC films and so was depicted in the NLR values having very low variation as a function of deposited laser fluence. The NLR coefficient of the film

deposited at laser fluence of ~15.0 J/cm^2 and helium pressure of 0.05 mbar and 0.1 mbar was found to be (2.40 ± 0.18) × 10^{-4} cm^2/W and (3.56 ± 0.26) × 10^{-4} cm^2/W, respectively. For the DLC film deposited at helium pressure of 0.5 mbar and 1 mbar, there was hardly any signature of NLO behaviour due to the presence of higher fraction of sp^3 bonding in the film as observed by Raman and ellipsometric results. Among the graphitic films, the highest NLR coefficient, (1.79 ± 2.19) × 10^{-3} cm^2/W, was observed for the film deposited at the base pressure of ~10^{-5} mbar. The NLR coefficient decreased with the increase in helium pressure for the graphitic thin films which is due to the improvement in structural order of the film, as observed by Raman measurement. The ordering of graphitic films decreases the change in polarization on laser exposure and hence NLR coefficient was found to be decreasing with the increase in helium pressure. All the carbon films exhibiting NLO behaviour displayed a valley followed by a peak in the transmittance curve for CA *Z*-scan measurement indicating that the nonlinearity in the carbon film is due to the self-focusing. The separation between the peak and valley position of CA transmitted profile is 1.7 times of the Rayleigh length of the focused beam confirming the presence of third order nonlinearity.

In conclusion, the desired quality of carbon based thin films devoid of hydrogen can be easily fabricated by pulsed laser deposition technique simply by selecting the appropriate deposition parameters.

Future scope of the work

The DLC films having higher fraction of sp^3 bonding of carbon atoms can be deposited on the metallic as well as on alloy substrate easily via PLD followed by wear resistance and hardness testing to explore its application as a protective coating. The graphitic thin film deposited at helium pressure of 10 mbar is higly ordered structure and

ultra-thin (~ 10 nm) which can be tested for its electrical conductivity for its application as a transparent electrode.

For further improving the quality of graphene layer via PLD, a parametric study is to be undertaken by depositing it at substrate temprature more than 700 °C and also in presence of helium ambient. The uniformly grown graphene layers will be studied for its electronic and mechanical properties. Graphene layers having homogeneous thickness can be studied for mode locking application as it exhibit saturable absorption behaviour.

The optical nonlinearity of DLC and graphitic thin films using cw laser is presented in this thesis. These films can also be subjected to nanosecond and femtosecond laser to study their NLO behaviour and optical limiting applications.

The quality of thin film via PLD technique depends on the dynamics of laser induced plasma. In order to understand the growth process of DLC and graphitic thin films by PLD, a systematic study on the laser induced graphite plasma can be taken as an extension of the present work.

List of Publications

Journal papers: Related to thesis work

(1) **Indrajeet Kumar** and Alika Khare, "*Optical nonlinearity in nanostructured carbon thin films fabricated by pulsed laser deposition technique*", Thin Solid Films **611** (2016) 56-61.

(2) **Indrajeet Kumar** and Alika Khare, "*Modified Z-scan set-up using CCD for measurement of optical nonlinearity in PLD carbon thin film*", Optics & Laser Technology, **77** (2016) 51–54.

(3) **Indrajeet Kumar** and Alika Khare, "*Multi- and few- layer graphene on insulating substrate via pulsed laser deposition technique*", Applied Surface Science **317** (2014) 1004-1009.

(4) **Indrajeet Kumar** and Alika Khare, "*Raman spectra of PLD deposited DLC thin films on Si substrate*", AIP Conference Proceedings, **1591** (2014) 1018-1020.

(5) **Indrajeet Kumar** and Alika Khare, "*Studies on Laser induced structural changes in pulsed laser deposited DLC film via Raman spectroscopy*", to be communicated.

(6) **Indrajeet kumar** and Alika Khare "*Effect of substrate temperature on diamond-like carbon thin films via pulsed laser deposition*", to be communicated.

(7) **Indrajeet Kumar**, Rahul Kesarwani and Alika Khare "*Effect of helium pressure on pulsed laser deposited diamond-like carbon thin films*", to be communicated.

(8) **Indrajeet Kumar** and Alika Khare "*Linear and nonlinear optical properties of pulsed laser deposited graphitic thin films*", to be communicated.

Journal papers: Not related to thesis work

(9) Mukesh Singh, **Indrajeet Kumar**, Alika Khare and Pratima Agarwal, "Third order optical nonlinear studies on highly conducting vertically aligned carbon nanoflakes" Materials Research Express, **3** (2016) 125005.

(10) Rasmi Ranjan Behera, Mamilla Ravi Sankar, J. Swaminathan, **Indrajeet Kumar**, Ashwini Kumar Sharma and Alika Khare, "Experimental investigation of underwater laser beam micromachining (UW-LBμM) on 304 stainless steel", The

International Journal of Advanced Manufacturing Technology, **85** (2016) 1969-1982.

(11) Archana Kushwaha, **Indrajeet Kumar** and Alika Khare, "Laser induced breakdown of Poly (Methyl Methacrylate (PMMA)) in air", Journal of Physical Science and Application, **4** (2014) 426-429.

Conference presentations: Related to thesis work

(1) **Indrajeet kumar**, Gyan Prakash Bharti and Alika Khare, "Laser power induced disorder in PLD deposited DLC film during Raman measurement", DAE-BRNS National Laser Symposium-23, 2014.

(2) **Indrajeet Kumar** and Alika Khare, "Nonlinear absorption and refraction measurement of PLD deposited carbon thin film", DAE-BRNS National Laser Symposium-22, 2014.

(3) **Indrajeet Kumar** and Alika Khare, "Raman spectra of PLD deposited DLC thin films on Si substrate", 58th DAE-Solid State Physics Symposium, 2013

(4) **Indrajeet Kumar** and Alika Khare, "Diamond like carbon films deposited by pulsed laser ablation of graphite target", DAE-BRNS 7th National Symposium on Pulsed Laser Deposition of Thin Films and Nanostructured Materials, 2013.

(5) **Indrajeet Kumar** and Alika Khare, "Optical nonlinearity of nanostructured carbon thin films deposited via pulsed laser ablation technique", International Conference on Nanotechnology (ICNT-2013), 2013.

(6) **Indrajeet Kumar** and Alika Khare, "Growth of few layers graphene via pulsed laser deposition technique using graphite target", Twenty-First International Symposium on Processing and Fabrication of Advanced Materials (PFAM XXI), 2012.

(7) **Indrajeet Kumar** and Alika Khare, "Raman spectrum of multilayer graphene grown by pulsed laser ablation of graphite target", 23rd International Conference on Raman Spectroscopy (ICORS-2012), 2012.

(8) **Indrajeet Kumar** and Alika Khare, "Effect of substrate temperature on pulsed laser deposited diamond like carbon thin films", Carbon Nanotechnology: Potential and Challenges, 2010.

Conference presentations: Not related to thesis work

(9) Rahul Kesarwani, G. P. Bharti, Partha P. Dey, **Indrajeet Kumar** and Alika Khare," NLO behaviour of semitransparent Cu thin film deposited by PLD", ICOL-2014.

(10) **Indrajeet Kumar**, P. K. Baruah, A. K. Sharma and Alika Khare, "Laser induced graphite plasma in liquid by CCD imaging", 28th PSSI National Symposium (Plasma-2013), 2013.

(11) **Indrajeet Kumar**, Satchi Kumari and Alika Khare, "Spatial evolution of laser induced graphite plasma by Langmuir probe", 27th PSSI National Symposium (Plasma - 2012), 2012.

(12) Archana Kushwaha, **Indrajeet Kumar** and Alika Khare, "Laser induced breakdown of Poly (Methyl Methacrylate (PMMA)) in air", 27th PSSI National Symposium (Plasma - 2012), 2012.

(13) **Indrajeet Kumar**, Archana Kushwaha and Alika Khare, "Emission spectroscopy of laser induced plasma from graphite target in vacuum", 26th National Symposium on Plasma Science and Technology (Plasma-2011), 2011.

(14) Archana Kushwaha, **Indrajeet Kumar** and Alika Khare, "Laser induced breakdown spectroscopy (LIBS) of polytetrafluroethylene (PTFE)", 26th National Symposium on Plasma Science and Technology (Plasma-2011), 2011.

(15) **Indrajeet Kumar**, Archana Kushwaha and Alika Khare, "Temporal studies of C_2 species in nanosecond laser-induced graphite plasma", DAE-BRNS 6th National Symposium on Pulsed Laser Deposition of Thin Films and Nanostructured Materials, 2011.

(16) Archana Kushwaha, **Indrajeet Kumar** and Alika Khare, "Preparation of polytetrafluroethylene (PTFE) thin films via PLD technique", CMDAYS, 2011.

(17) **Indrajeet Kumar**, Arpita Nath and Alika Khare, "Synthesis of nanodiamonds via pulsed laser ablation in Iso-propyl alcohol", 2nd International Conference on Advanced Nanomaterials and Nanotechnology (ICANN-2011), 2011.

(18) **Indrajeet Kumar**, Arpita Nath and Alika Khare, "Formation of diamond nanocrystals via pulsed laser ablation of graphite in liquids", 24th International Conference on Amorphous and Nanocrystalline Semiconductor (ICANS 24), 2011.

Workshops/Schools attended:

(1) "National Workshop on Advanced Probing Techniques in TEM (APTTEM-2016)" during 15-16 February, 2016, organized by Indian Institute of Technology Guwahati, Guwahati, India.

(2) "IEEE Matlab Workshop" during 22-23 June, 2013, organized by IEEE Student Branch, Indian Institute of Technology Guwahati, Guwahati, India.

(3) "IEEE Workshop on Compressive Sensing and Technical Writing" during 6-7 April 2013, organized by IEEE Student Branch, Indian Institute of Technology Guwahati, Guwahati, India.

(4) "Quality Improvement Programme (QIP) short term course" during 1-6 August 2011, organized by Department of Physics, Indian Institute of Technology Guwahati, Guwahati, India.

(5) "Winter School on Recent Trends in Physics of Atoms, Molecules and Lasers (WSRTPAML- 2011)" during January 9-31, 2011, organized by Department of Physics, Faculty of science, Banaras Hindu University, Varanasi, India.

(6) "DST SERC Preparatory School on Modern Optics" during 10-23 November, 2010 organized by Department of Physics, Indian Institute of Technology Guwahati, Guwahati, India.